

**PRE-EQUILIBRIUM EXCITATION OF
NUCLEI IN
(p, α) and ($p, {}^3\text{He}$) REACTIONS
INDUCED BY 120, 160 AND 200 MeV
PROTONS**

Gillian John Arendse



*This is presented in partial fulfilment of the requirements
for the degree of Master of Science at the
University of Stellenbosch
December 1994*

Supervisor: Prof A. A. Cowley

Declaration

I the undersigned hereby declare that the work contained in this thesis is my own original work and has not previously in its entirety or in part been submitted at any university for a degree.



Date: 2.12.94

PRE-EQUILIBRIUM EXCITATION OF NUCLEI IN (p, α) and $(p, {}^3\text{He})$ REACTIONS INDUCED BY 120, 160 AND 200 MeV PROTONS.

Gillian John Arendse

University of Stellenbosch

December 1994

ABSTRACT

The study of pre-equilibrium reactions induced by medium-energy light ions have become of increasing importance in recent years as they represent the bulk of the measured spectrum. On a nuclear time scale these reactions are known to take place after a one-step process of exciting discrete states in the residual nucleus but long before the process whereby the projectile distributes its kinetic energy equally over all target nucleons to form a compound nucleus which decays statistically. In this work the systematic behaviour of the continuum of complex ejectiles was investigated as a function of incident proton energy and target mass.

The continuum energy spectra for the reactions ${}^{27}\text{Al}(p, X)$, ${}^{59}\text{Co}(p, X)$, and ${}^{197}\text{Au}(p, X)$, with $X=\alpha$ and ${}^3\text{He}$, were measured using a five element detector telescope. Data were acquired at scattering angles between $10 - 160^\circ$ at incident proton energies of 120 and 200 MeV, and at scattering angles between $20 - 140^\circ$ for an incident proton energy of 160 MeV.

Experimental angle-integrated cross sections were compared with calculated angle-integrated cross sections using the geometry dependent hybrid (GDH) model. The comparison between the experimental data and the calculations were used to quantitatively estimate the contribution of the evaporation process to the pre-equilibrium spectrum.

The experimental angular distributions from the reaction (p, α) and $(p, {}^3\text{He})$ on ${}^{27}\text{Al}$, ${}^{59}\text{Co}$, and ${}^{197}\text{Au}$ were compared with calculated angular distributions using the phenomenological parametrization of Kalbach. In general good agreement between the experimental data and the calculations were obtained. Minor discrepancies were observed with regard to target mass and incident proton energy dependence. It is believed that the characteristics of these discrepancies could provide guidance to the future attempts to develop a proper quantum mechanical description of the reaction mechanism of complex-ejectile production induced by energetic protons.

VOOR-EWEWIGS OPWEKKING VAN KERNE IN (p, α) en $(p, {}^3\text{He})$ REAKSIES GEÏNDUSEER DEUR PROTONE MET INVALSENERGIEË VAN 120, 160 EN 200 MeV.

Gillian John Arendse

Universiteit van Stellenbosch

Desember 1994

SAMEVATTING

Die ondersoek van voor-ewewigs reaksies geïnduseer deur medium-energie ligte ione het oor die afgelope jare van toenemende belang geword aangesien dit 'n groot deel van die gemete spektrum uitmaak. Wat die tydskaal van die reaksies betref, vind dit plaas na 'n enkel proses waartydens diskrete toestande binne die reskern opgewek word, maar lank voor die projektiel al sy kinetiese energie oorgedra het aar die teiken-nukleone om sodoende 'n tussenkern te vorm wat statisties verval. In hierdie projek word die sistematiese gedrag van die kontinuum van komplekse deeltjies ondersoek in afhanklikheid van invalsenergie en teikenmassa.

Energie spektra vir die reaksies ${}^{27}\text{Al}(p, X)$, ${}^{59}\text{Co}(p, X)$ en ${}^{197}\text{Au}(p, X)$, met $X=\alpha$ en ${}^3\text{He}$, is gemeet met behulp van 'n vyf element detektor teleskoop. Data is versamel by verstrooiings hoeke tussen $10 - 160^\circ$ vir invalsenergieë van 120 en 200 MeV, en vir verstrooiingshoeke tussen $20 - 140^\circ$ vir 'n invalsenergie van 160 MeV.

Eksperimentele hoek-geïntegreerde kansvlakke is vergelyk met berekende hoek-geïntegreerde kansvlakke wat verkry is met behulp van die geometries-afhanklike hibried (GDH) model. Die ooreenstemming tussen die eksperimentele data en die berekening is gebruik om 'n kwantitatiewe afskating te maak van die bydrae van die verdampings-proses tot die gemete voor-ewewigs spektrum.

Die eksperimentele hoekverdelings van die reaksies (p, α) en $(p, {}^3\text{He})$ op ${}^{27}\text{Al}$, ${}^{59}\text{Co}$ en ${}^{197}\text{Au}$ was vergelyk met berekende hoekverdelings, afkomstig van die fenomenologiese parametrisering van Kalbach. Oor die algemeen is goeie ooreenstemming tussen die eksperimentele data en die berekende hoekverdelings gevind. Geringe afwykings tussen die eksperimentele data en die berekening kom nogtans voor afhangend, van invalsenergie en teiken massa. Die aard van die sistematiese afwykings mag riglyne lewer tot die daarstelling van 'n kwantum meganiese beskrywing van die reaksie meganismes betrokke by die produsering van komplekse deeltjies geïnduseer deur energieke protone.

ACKNOWLEDGEMENTS

My sincere appreciation goes to Professor A. A Cowley for his support during, and supervision of, this work. I would also like to thank the rest of the research team at the Physics Department, Dr W. A Richter, Dr J. A Stander, Prof J. W Koen and Mr W Loubser for the role they played during the experimental set-up, the data acquisition and the data analysis.

A word of special thanks goes to Dr G. F Steyn at the NAC for his guidance and support especially during the early stages of the project.

A word of thanks goes to Mr N Steenkamp for producing a figure in the thesis on the experimental hardware.

A word of special thanks goes to the staff at the Physics Department for their continued support and encouragement throughout the years. I would also like to thank my fellow-students for their support and wish them all the success with their studies.

Finally I would like to thank my parents, my brothers, my sister, my family and my friends for their continued support, encouragement and all their love throughout the years. Without their support it would have been even harder for me to reach this milestone in my life.

Philippians 4: 13

" I can do all things through Christ which strengtheneth me. "

CONTENTS

CHAPTER 1: INTRODUCTION

1. Overview of Reaction Theory	9
2. Scientific Justification for Experiment	14

CHAPTER 2: THE EXPERIMENT

1. General Aspects	17
2. The Facility	17
3. Scattering Chamber	19
4. Detector Telescopes	20
5. Targets	21
6. Electronics	22
(a) Linear	23
(b) Logical	23
7. Data Acquisition	26
(a) Computer Hardware	26
(b) Computer Software	27
8. Experimental Procedure	28

CHAPTER 3: DATA ANALYSIS

1. Particle Identification	31
2. Beam Direction	33
3. Energy Calibration	33
4. Corrections built into Analysis	35
(a) Computer and Electronic Dead Time Corrections	35
(b) Dead Layer Corrections	36

5. Absolute Cross Section	45
6. Error Analysis	45
7. Energy Spectra and Angular Distributions	46

CHAPTER 4: THEORETICAL CALCULATIONS

Kalbach's Phenomenological Parametrization

1. Basis for Angular Systematics	49
2. Kalbach's Parametrization	54
(a) Overview	54
(b) Improved Parametrization	54
(c) Parameters	55
(d) Calculations	56

CHAPTER 5: RESULTS

1. Energy Spectra	59
(a) α particle emission	59
(b) ^3He particle emission	59
(c) Comparison of α and ^3He particle emission energy spectra	60
2. Angular Distributions	71
(a) Comparison for (p, α) reactions	71
(b) Comparison for $(p, ^3\text{He})$ reactions	71
3. Comparison of experimental angle-integrated cross sections with Geometry Dependent Hybrid (GDH) model calculations	72

CHAPTER 6: SUMMARY AND CONCLUSIONS

91

REFERENCES

93

CHAPTER ONE

INTRODUCTION

INTRODUCTION TO NUCLEAR REACTION THEORY

1. Overview

The theory of nuclear reactions has a very long history, stretching back to the 1930s when Bethe calculated the scattering from a central potential, Bohr proposed the compound nucleus theory, and Oppenheimer and Philips initiated the theory of direct reactions. In the following years these theories have been extensively developed and used to calculate a wide range of nuclear cross sections.

Many different processes can take place when a projectile interacts with a target nucleus. A proton of low incident energy interacts mainly with the Coulomb field and is elastically scattered according to Rutherford's Law. As the incident energy of the proton is increased it encounters the nuclear field and the scattering cross-section departs from Rutherford's Law. This may be described by the optical model, which describes the interaction by a complex potential. The potential has to be complex to allow for the various non-elastic processes which become energetically possible.

With the developments that have taken place, it has become clear that reaction processes can be divided into two stages:

a DIRECT STAGE that takes place in a time comparable with the transit time of the projectile across the target nucleus, and

a COMPOUND NUCLEUS STAGE, in which the residual nucleus, after the direct stage, emits further particles after attaining statistical equilibrium. It was found that the cross sections of many nuclear reactions could be described by the direct reaction or by compound nucleus theories, or sometimes by a combination of the two.

During the last two decades it has become increasingly clear that there are many reactions that cannot be adequately described in terms of the direct and compound nucleus reaction theories. There is evidence that emission can take place after the direct stage, but long before the attainment of full statistical equilibrium.

At present we are considering the nuclear reaction as taking place in a number of stages by a series of nucleon-nucleon interactions which lead to the fully statistical excitation of the nucleus.

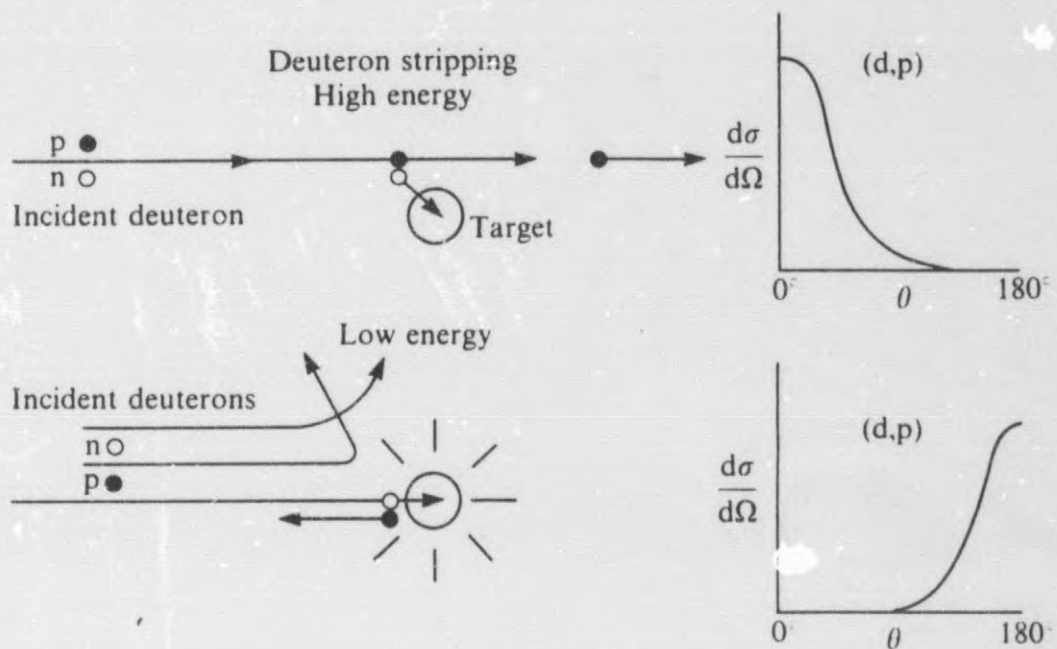


Figure 1.1 Angular Distributions according to Hodgson 1971 [2]

(a) Direct Reactions

In 1935 Oppenheimer and Philips [1, 8] considered the (d,p) reaction. They observed that the process occurred by a direct transfer of a neutron to the target without the creation and subsequent decay of a compound nucleus. The reaction lead to angular distributions being peaked in the forward or backward direction depending on the incident energy. This situation is depicted in figure 1.1.

The term direct reaction, in general, include all processes that directly connect the initial and final states during the reaction, without the formation of a intermediate compound system.

Direct Reactions take place in the time it takes the incident particle to traverse the target nucleus. At low energies it is found that the interaction is with the nucleus as a whole, and as the energy is increased with the individual target nucleons. The cross-sections for direct reactions are usually peaked in the forward direction. Examples of direct reactions are:

- i. Inelastic scattering where the incident particle gives some of it's energy to the target nucleus, raising it to an excited state.
- ii. Nucleon transfer reactions where one or more nucleons are transferred from:
 - A. the projectile to the target (stripping reaction)
 - B. the target to the projectile (pickup reaction)
- iii. Charge exchange where the emitted particle has the same mass as the projectile

The direct reaction is the dominant process at high incident energies.

(b) Compound Nucleus Reactions

The foundations of compound nucleus reactions were laid by Bohr (1936) [3, 8] and Bohr and Kalckar (1937) [4, 8]. They proposed that a nuclear reaction begins with the capture of the projectile by the target nucleus, followed by the sharing of its energy amongst all the composite nucleons. Statistical equilibrium is established after which emission of particles take place from the compound system. This statistical process continues for as long as it is energetically possible, after which the residual nucleus reaches its ground state via gamma emission.

These processes of formation and decay were regarded as separate, where the second stage had no connection to the first stage of the encounter.

At low energies the incident particle may be captured by the target to form an excited compound nucleus. This can only happen if there is a state accessible to the compound nucleus at the appropriate energy. The character of the reaction therefore depends on the structure of the compound nucleus.

For example, when dealing with light nuclei, the energy levels are well spaced. The cross section displays a resonance structure whenever the incident energy corresponds with the individual states.

When dealing with heavier nuclei on the other hand, the energy levels are closely spaced. The result is that the resonance structure is averaged out making the cross section vary smoothly with energy.

The energy carried by the incoming particle is distributed amongst the constituent nucleons until statistical equilibrium is established. Eventually a nucleon or group of nucleons receive enough energy to escape, and this process continues as long as it is energetically possible, i.e. it continues as long as the excitation energy is above the emission threshold. After this emission process the remaining nucleus goes to the ground state via gamma emission. At higher incident energies a direct process may occur first. The direct process is then followed by the statistical decay of the residual system.

A characteristic feature of compound nucleus reactions is the independence of the processes of formation and decay. During the energy-sharing process all memory of the initial state are lost, except the conservation laws which have to hold, i.e. energy, parity and angular momentum. As a result we find that the Angular Distribution, a plot of the cross-section as function of angle, is symmetrical about 90° . The compound nucleus reaction is the dominant process at low incident energies.

(c) Pre-equilibrium Reactions.

In 1947 Serber [5, 8] made the hypothesis that the interaction of a high-energy nucleon with the nucleus could be described in terms of two-body interactions of the projectile with nucleons of the target. These interactions then initiate a cascade of nucleon-nucleon interactions by which the energy of the projectile is spread amongst an ever increasing number of nucleons.

Two stages were distinguished:

- i. A fast stage corresponding to a cascade of nucleon-nucleon interactions, during which the incident particle emerges from the nucleus, with a reduced energy, together with particles struck near the surface of the nucleus.
- ii. A slow stage corresponding to the end of the intranuclear cascade where the fully equilibrated nucleus de-excites by means of the usual evaporation process.

The accumulation of experimental results indicated the presence of phenomena that could not be characterized by direct or compound reaction mechanisms.

Nuclear reactions were obtained which have cross section distributions that is symmetrical about 90° , indicating a compound nucleus process, but an energy distribution with more energetic particles than predicted by compound nucleus theories. At higher energies, when the direct process is expected to dominate, reactions were found that could not be understood by direct reaction theory.

This suggests that the nuclear excitation takes place in a number of stages, and that emission can take place at an earlier stage before full statistical equilibrium is established. This type of process by which nuclear reactions occur is called the pre-equilibrium or intermediate process.

Over the years many different theories were developed to understand the observed systematics. These theories all have in common the idea that the process of nuclear excitation takes place in a number of stages, corresponding to the excitation of more and more particle-hole pairs.

In 1966 Griffin proposed the exciton model [6, 7, 8] to describe the formation and decay of the compound nuclear state. The hypothesis was made that the incoming particle, by interacting with the target nucleus, gives rise to a simple configuration characterized by a small number of excitons (excited particles and holes). Successive two-body residual interactions give rise to an intranuclear cascade through a sequence of states, characterized by increasing exciton number, eventually leading to a fully equilibrated nucleus.

The first attempt to develop a formal theory to describe the pre-equilibrium reaction process was made by Feshbach, Kerman, and Koonin in 1980 [9]. In the FKK theory two different statistical states are postulated to occur during the course of the de-excitation of the nucleus before evaporation.

i. Multistep Compound Process MSC

In a MSC reaction all particles remain bound during the equilibration cascade. Quantum mechanical theories assume that the nucleus is excited through a series of nucleon-nucleon collisions between the projectile and the target nucleus. The interaction is characterized by a process in which particle-hole pairs are continuously created, until the incident energy is spread through the nucleus. At each stage there are three possibilities:

- A. excitation of an additional particle-hole pair
- B. de-excitation of a particle-hole pair
- C. emission into the continuum

Transitions at each stage of the MSC process is much slower than that for the MSD process, as a quasi-equilibrium has to be established at each stage, which also causes the angular distribution to be symmetric about 90° .

Incident protons of 10–15 MeV are most likely to excite bound or quasi-bound particle-hole ($p - h$) and therefore initiate the MSC process. [8]

ii. Multistep Direct Process MSD

At low incident energies it is found that all the particles in the intranuclear cascade remain bound, so that it is possible to describe the reaction with the MSC theory. As the incident energy increases it becomes more likely that at least one particle remains in the continuum, so that the "memory" of the original direction of the projectile is retained. Interactions, occurring in a time comparable to the transit time of the nucleon, take place in a sequence of stages, yielding a cross section that is peaked in the forward direction. The MSD process predominates for incident protons with energies ≥ 25 –30 MeV.

2. Scientific Justification

In the proton induced experimental proton energy spectra three distinct energy regions can be identified as shown in figure 1.2.

- (a) Evaporation Region
 - dominated by particles evaporated from the compound nucleus
- (b) Region of Discrete States
 - peaks for direct transitions to discrete low energy levels
- (c) Continuum
 - mainly excited by multistep, pre-equilibrium processes

To understand medium-energy nuclear reactions it is necessary to have an in-depth knowledge of the reaction mechanism for the excitation of the continuum.

Two-body reactions $A(a,b)B$ leading to highly excited states, as well as decay products of the residual nucleus contribute to the excitation of the continuum.

As we know, pre-equilibrium mechanisms leading to proton emission have been studied extensively at NAC [11–14]. It now becomes important to explore the continuum with regard to the emission of complex ejectiles, as the existing experiments do not allow a determination of the systematics.

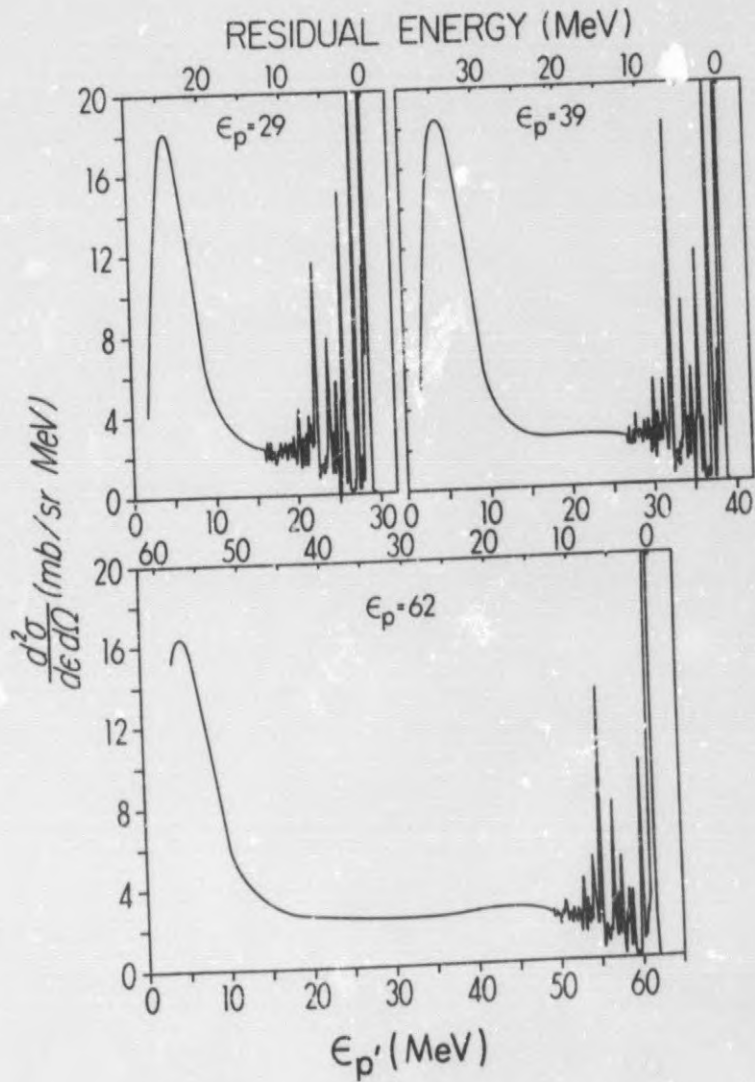


Figure 1.2 *Energy Regions on Proton Energy Spectra (Blann 1975) [10]*

Current ideas regarding the reaction mechanism favour a clustering mechanism, which was introduced at lower energy to explain the observed systematics.

It is expected that a proper quantum mechanical prescription will be developed soon at Oxford so that the theoretical tools to interpret the experimental data will be available.

CHAPTER TWO

THE EXPERIMENT

EXPERIMENTAL DESCRIPTION

1. General Aspects

The basic experimental objective of the study was to bombard ^{27}Al , ^{59}Co , and ^{197}Au nuclei with protons of 120, 160, and 200 MeV. The detectors were chosen to stop 200 MeV alphas within the detector telescope. Measurements were carried out during May–June 1993, at the NAC (National Accelerator Centre). Fast timing signals were used to specify the logic for the coincidence measurements. The conventional $\Delta E - E$ technique was used for particle identification. By setting gates on the two dimensional spectra we were able to select the various ejectiles of interest, in this case α and ^3He particles. Experimental data was stored on magnetic tapes for data reduction after the experiment had been carried out.

2. The Facility

The NAC provides in the needs of three user communities on a regular basis ever since November 1986. It provides particle beams for use in basic research, mainly nuclear physics, radioisotope production, and proton and neutron therapy.

The experiment was performed at the cyclotron facility of the National Acceleration Centre (NAC) [15]. A layout of the facility is shown in Figure 2.1. A solid pole injector cyclotron (SPC1) with an internal ion source, capable of producing unpolarized light ions, accelerates the protons to a maximum energy of 8 MeV for injection into the first orbit of the Separated Sector Cyclotron (SSC) where the protons are accelerated to a maximum energy of up to 200 MeV. A second injector cyclotron (SPC2) is able to produce polarized and heavy ion beams.

Charged particles are extracted from the SSC and transported via high-energy beamlines through two 90° analyzing magnets before being directed by a switching magnet into one of the lines which enter the three shielded vaults for experimental use. From the switching magnet a pair of doublet quadrupoles on beamline A (figure 2.1) focuses the beam at the centre of a scattering chamber. The beam is stopped 6 meters from the exit of the scattering chamber. A concrete shielded beamstop is used as a Faraday Cup, which measures the total deposited charge. For this experiment beam energies of 120 MeV, 160 MeV and 200 MeV were used with the beam current varying between 60 and 600 nA, depending on the scattering angle.

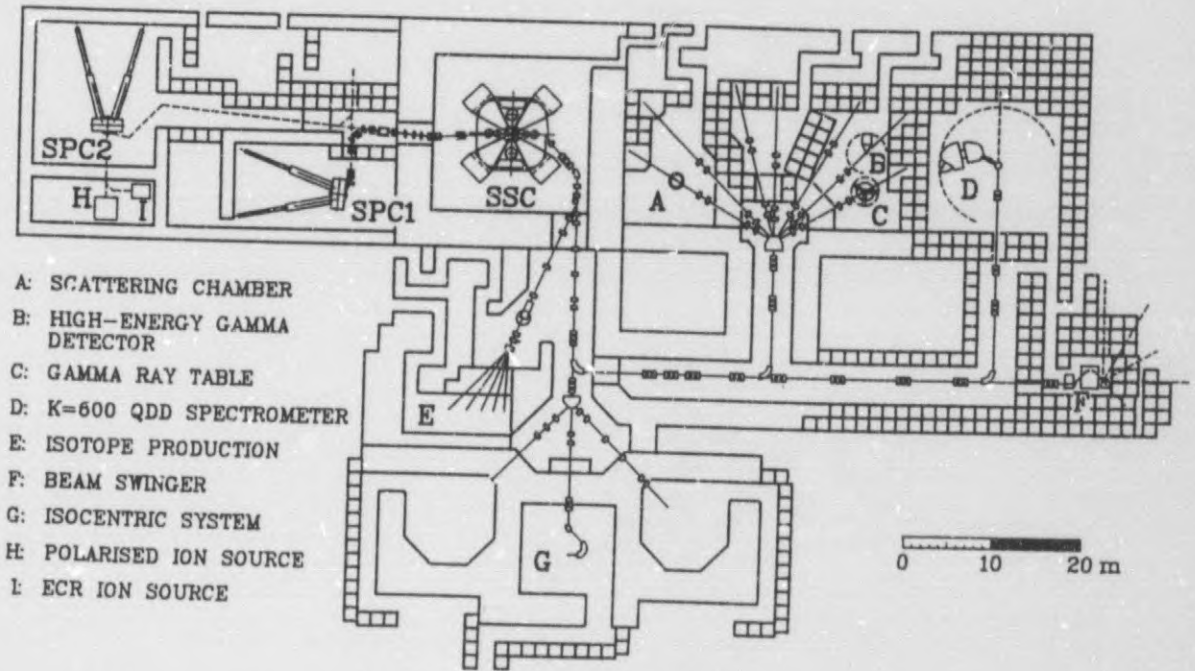


Figure 2.1 A layout of the facilities at the National Accelerator Center (NAC)

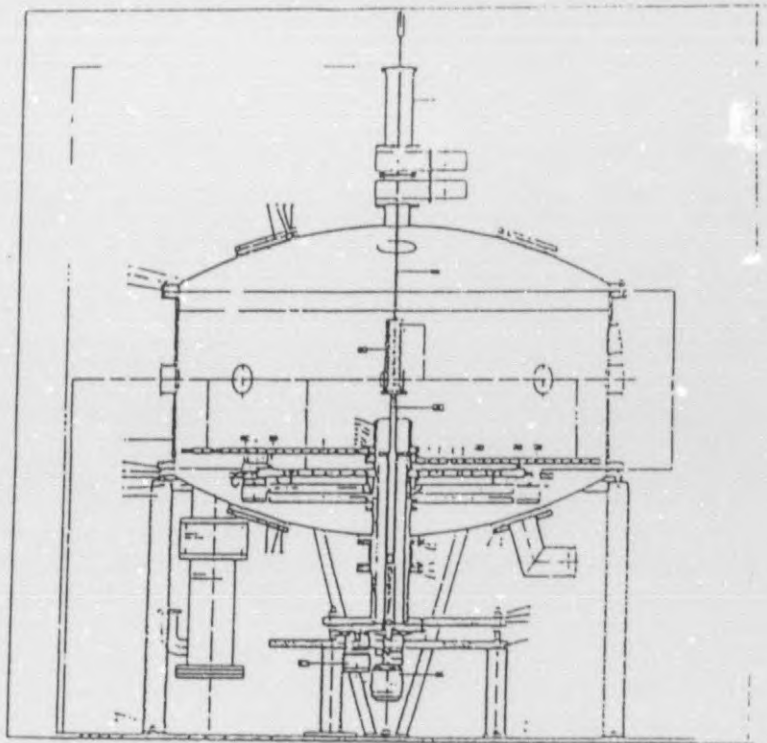


Figure 2.2 The Scattering Chamber

3. The Scattering Chamber

One of the experimental facilities used in light-ion experiments at NAC is the precision 1.5 m diameter scattering chamber, originally acquired from the University of Maryland. (figure 2.2) The scattering chamber is situated in the vault which is served by beamline A.

The target mechanism, situated at the centre of the chamber, makes provision for a target ladder, in which five targets can fit. By changing its position vertically, with respect to the beam, any one of the five targets can be selected. The target ladder can further be rotated around a vertical axis which provides a mechanism for changing the target angle with an accuracy of $\sim 0.1^\circ$.

Two independently movable arms can be positioned at any angle with respect to the beam direction. (figure 2.3)

Various slot positions on the arms is used to bolt down the detector telescopes and pre-amplifiers. The walls of the chamber are equipped with ports which provide feedthroughs for $50\ \Omega$ and $93\ \Omega$ cables as well as the high voltage and power supply cables. One of the ports is used to view the target for the purpose of focussing the beam spot. All the movable components inside the chamber can be remote controlled from either inside the vault or from a control unit in the data room.

During the experiment the scattering chamber and the beamlines were kept at a vacuum of 10^{-5} mbar. To obtain this vacuum in a reasonable time the evacuation process was carried out in three stages. A fore-vacuum of 0.1 mbar was obtained with the use of a rotary pump. A turbo molecular pump was then used to lower the vacuum to 10^{-3} mbar. Finally a cryogenic pump was used to get the vacuum down to 10^{-5} mbar.

All signals emerging from the detectors are subjected to the noise of an electrical environment. To eliminate noise due to ground-loops, the scattering chamber is earthed in the following way:

While setting up, the chamber is earthed to "mother earth", which is simply a connection to a copper rod in the soil. During an experiment however, the chamber is earthed to "common earth", which implies a connection to a copper grid underneath the floor of the data room, to which the computer and all the electronic racks are also connected.

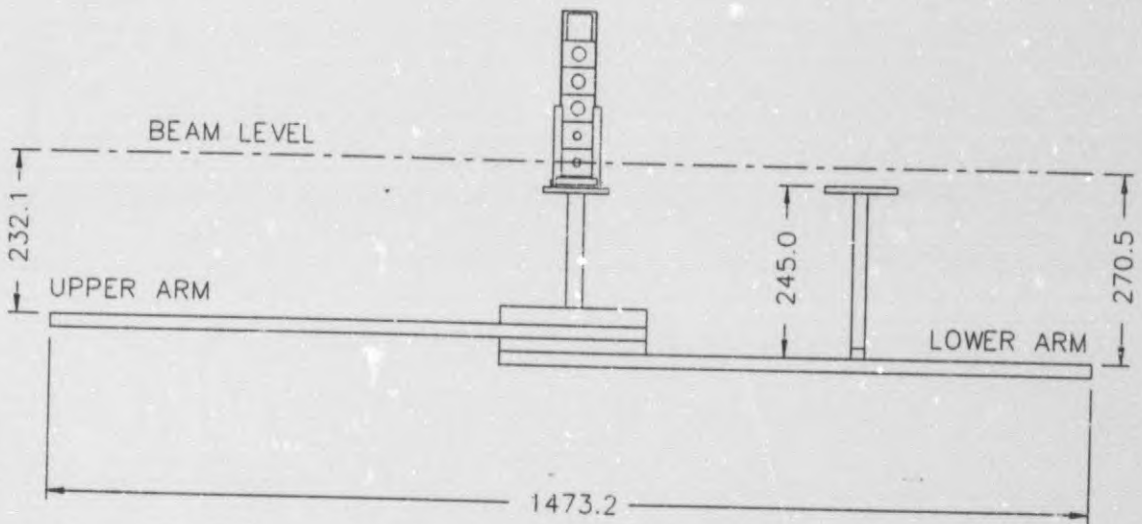


Figure 2.3 Side elevation of the movable components inside the scattering chamber

4. Detector Telescopes

During data acquisition a single five element detector telescope, with the detectors labelled A, B, C, etc. was used. (figure 2.4) Our experimental setup consisted of:

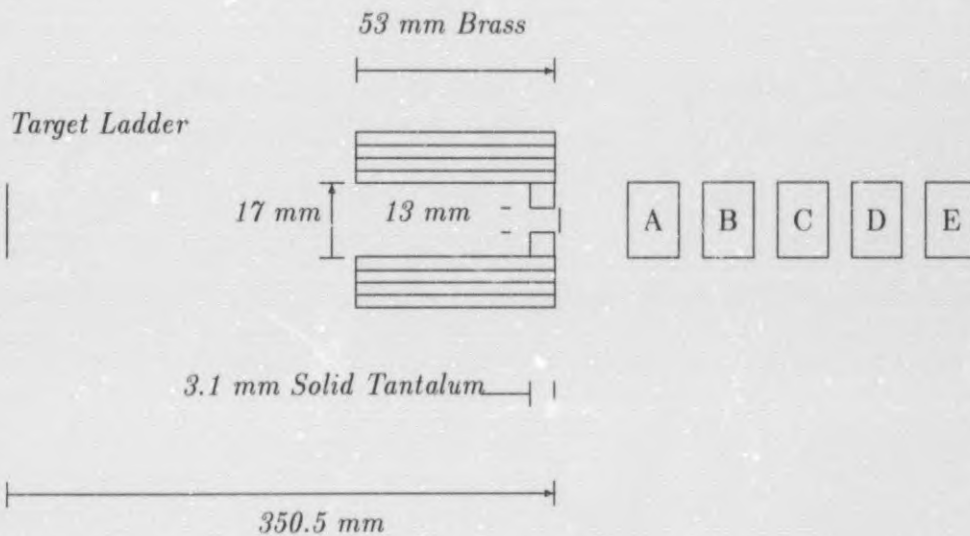
- (a) A 150 μm Si
- (b) B 5000 μm SiLi
- (c) C 5000 μm SiLi
- (d) D 5000 μm SiLi
- (e) E 1000 μm Si

The thickness of the detectors have been chosen in such a way that 200 MeV α particles can be stopped within the telescope.

For collimation a solid tantalum collimator, 3.1 mm thick with a hole diameter of 13 mm, was used. In order for us to position the collimator in front of the detectors a brass holder was used. This brass holder had an insert to which the tantalum collimator was fixed.

Mylar foil, 13 μm thick, was placed over the front hole of the collimator to reduce the flux of low energy electrons onto the detector telescope.

The collimating system was placed 350.5 mm from the centre of the target and subtended a solid angle of 1.08 msr. The detector telescope could be moved over an angular range of 10-160°.



- A: 150 μm Si detector
 B: 5000 μm SiLi detector
 C: 5000 μm SiLi detector
 D: 5000 μm SiLi detector
 E: 1000 μm Si detector

Figure 2.4 Cross section of the detector telescope used with 13 μm Mylar foil over collimator.

During the calibration of our detector telescope it was necessary to make use of a second detector telescope. By observing the elastically scattered protons in coincidence with the recoiling ^1H or ^2H from the $^1\text{H}(p,p)^1\text{H}$ and $^2\text{H}(p,p)^2\text{H}$ reactions we were able to calibrate our detector system.

(Chapter 3)

The second telescope contained a ΔE detector as well as a detector used as a stopping detector. The detectors were:

- (a) 1000 μm Si
- (b) NaI

Again it was necessary to use a collimating system, much the same as the one used during the data acquisition. It was however necessary to use a smaller diameter to reduce the kinematic spread and thereby ensuring good energy resolution.

5. Targets

The target ladder used during the experiment can only contain five targets. It was therefore necessary to use two target configurations. The first configuration consisted of our three targets ^{27}Al , ^{59}Co , and ^{197}Au , an empty frame and a rubv target with a 3 mm hole.

The ruby target displays scintillation properties when struck by a particle

Target	Target thickness $\frac{mg}{cm^2}$
^{197}Au	4.0 ± 0.1
^{59}Co	1.00 ± 0.02
^{27}Al	2.9 ± 0.2

Table 2.1 List of targets used during experiment

beam, and can therefore be used for the purpose of focussing the beam at the target centre.

Beam halo comprises mainly secondary particles originating from the scattering of the beam off beamline components. In order for us to be able to monitor the effect of this halo, an empty frame was used. By comparing the count rate due to "halo interactions" (empty frame in position) with the count rate due to "true interactions" (target in position) we were able to determine whether or not the effect of halo could be ignored. Excessive halo was reduced by the operators with the use of various slits to an acceptable level, less than 5%.

A list of the targets used during the experiment is given in Table 2.1.

The thickness of the targets were obtained by carefully weighing the targets and calculating their areas.

The second configuration was used during the energy calibration of the various detectors. In this configuration a CD_2 and a CH_2 target, both polythene targets, were used together with the ruby and the empty frame.

6. Electronics

This section deals with the electronic setups which were used during the experiment, to convert the detected events to electrical signals for processing by the computer software.

Output signals from all the detectors were fed into charge sensitive pre-amplifiers. The pre-amplifiers were mounted in the scattering chamber in order to minimize the cable capacitance and hence improve the quality of the timing signals.

The function of the pre-amplifier is to amplify the weak signals coming from the detectors and to shape the subsequent output pulse (tailpulse). The pre-amplifier generates two types of output pulses, namely fast timing and slow linear pulses. These pulses carry different information and have to be treated differently.

(a) Linear Electronics

The amplitude of the linear signals contain information on the amount of energy deposited in the detector. A block diagram of the electronics used during data acquisition is shown in Figure 2.5.

From the patch panel inside the data room the linear signals were fed into linear amplifiers followed by delay amplifiers and linear gate stretchers (LGS) which opened the channels to analog to digital converters (ADC). Only the signal of an event of interest was selected by logical requirements which were provided by the timing signals. These logic pulses were used to generate the necessary gate for the linear gate stretcher module of a specific detector. Signals from the LGS modules were fed into fast ADC. After digitation, the energy signals are fed into the VAX/VMS computer via CAMAC and a Microprogrammable Branch Driver (MBD).

(b) Logical Electronics

The fast linear timing signals are converted to logical signals which have a fixed shape, and magnitude which represents the two logical states 0 or 1. A block diagram of the logical electronics used during the experiment is shown in figure 2.6.

The fast output signals from the pre-amplifiers were sent through separate Timing Filter Amplifiers (TFA), Delays, and Constant Fraction Discriminators (CFD) to process the fast logic signals.

The logical signals, derived from the timing signals, were used to identify valid events. An event was considered valid when a particle was detected in detectors A and B or B and C with NO veto signal, that is a signal from the fifth detector.

Our condition for a valid event was therefore:

$$(A \cup C) \cap B \cap \bar{E}$$

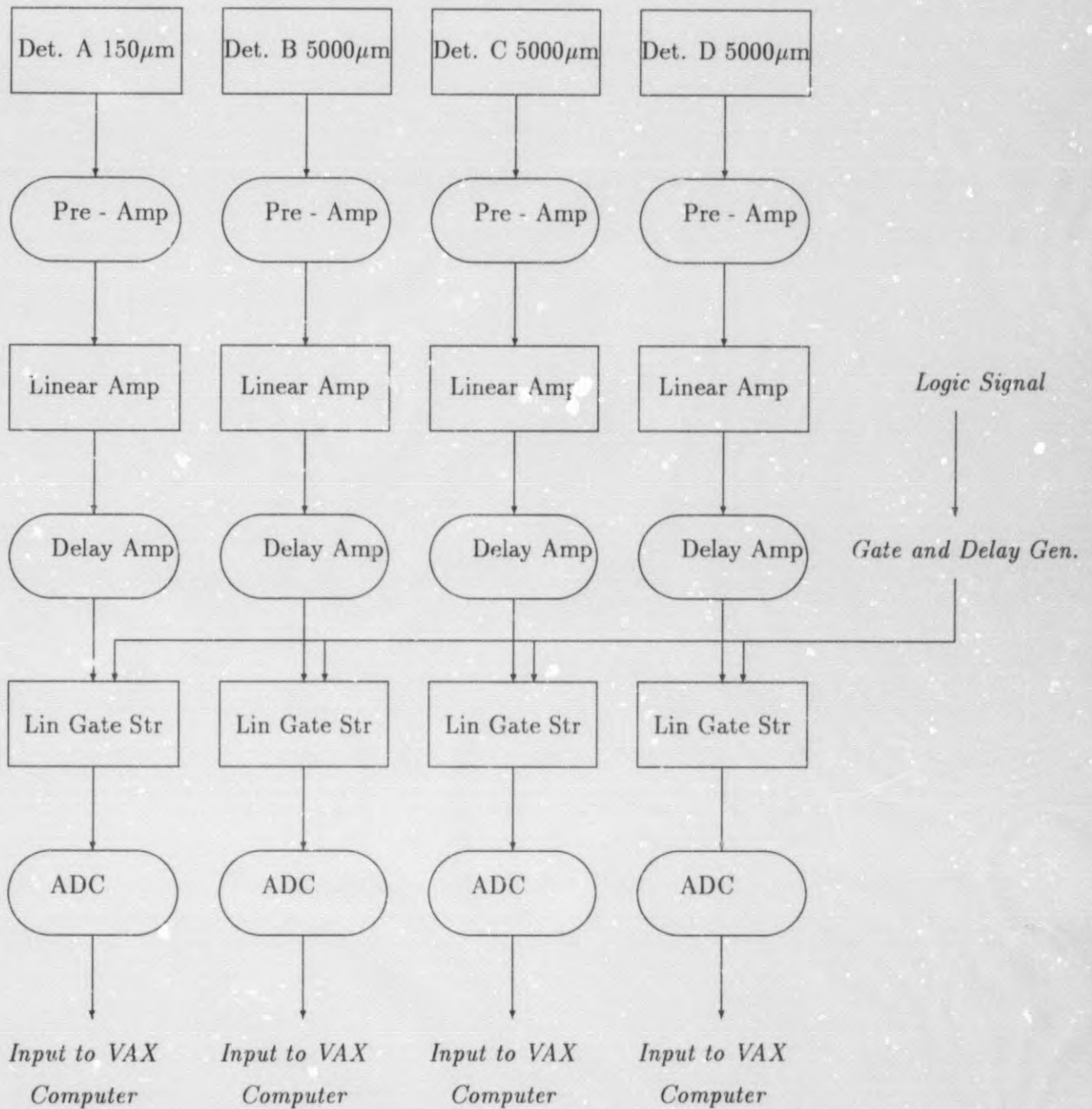


Figure 2.5 Diagram of the Linear Electronics used during the experiment

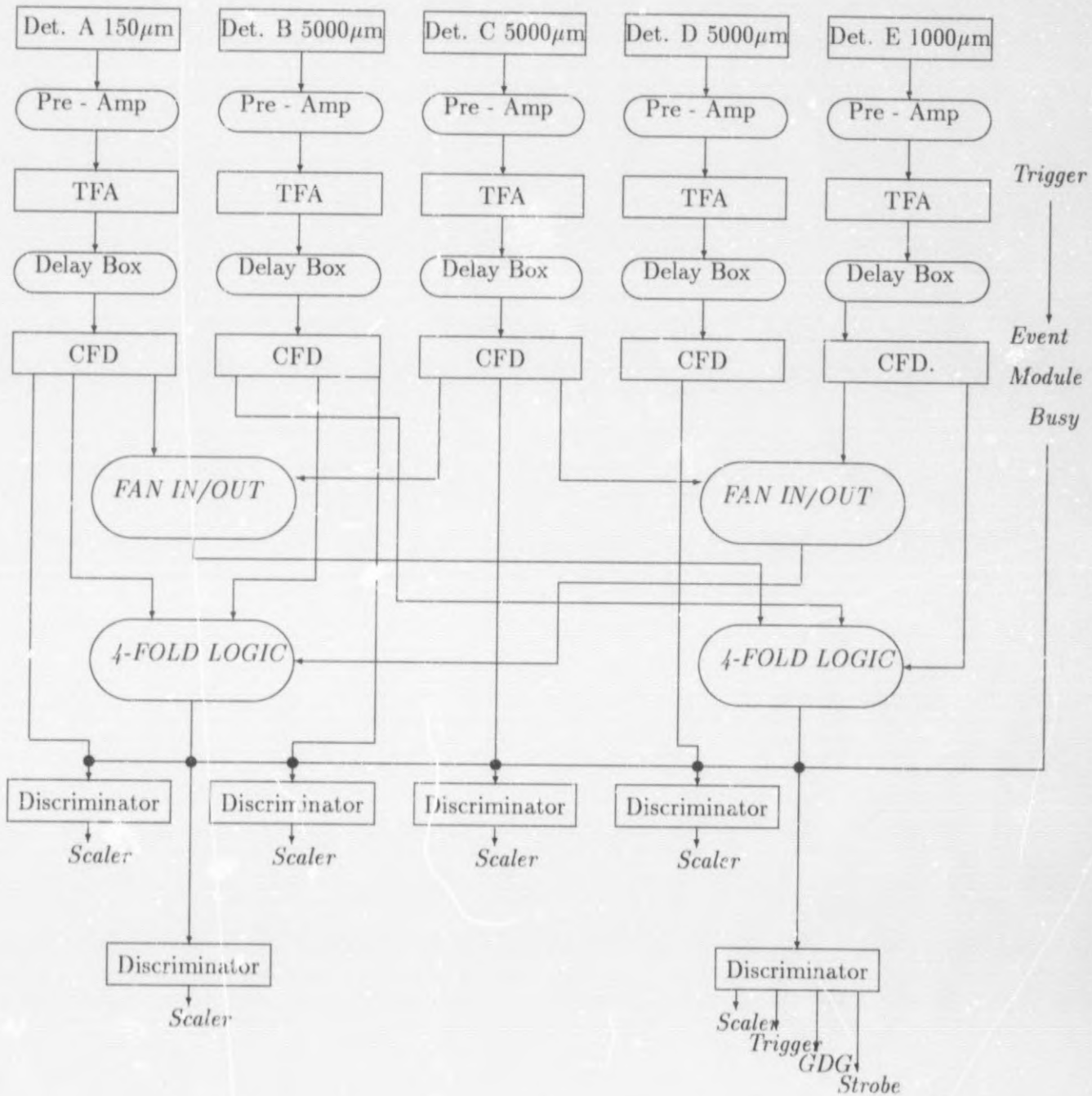


Figure 2.6 Diagram of the Logical Electronics used during the experiment

The .OR. operation was carried out by a FAN IN-OUT module, while the .AND. operation, together with the VETO, was carried out by a FOUR FOLD LOGIC UNIT. The output of this module was fed into a discriminator, which was inhibited by a computer busy signal. The output of the discriminator was used as the event trigger, and also as the input of a coincidence register. The logical signals were generated by feeding one of the discriminator outputs into a Gate and Delay Generator (GDG). The GDG is then used to open the necessary gates on the linear pulses.

The coincidence register is used to separate events produced by particles that stop in detector B from all the valid events. This is done by setting a register if a coincidence is observed between A and B with NO signal from C or the Veto.

The condition for coincidence is given by:

$$(A \cap B) \cap (\bar{C} \cup \bar{E})$$

From each detector element a signal was fed into an uninhibited scaler, while the coincidence signals were fed into inhibited scalers.

The digital output signals from the Current Integrator (CI) were recorded in an uninhibited scaler, as well as a scaler inhibited by a computer busy signal. The two scaler values were used to monitor the computer dead time. In order to monitor the electronic dead time of our electronic setup, pulser signals were fed into the linear electronic circuit. (Chapter 3)

7. Data Acquisition

(a) Computer Hardware

CAMAC is a modular system which forms the interface between the output of the NIM modules and the Computer, which controls and activates the data acquisition process. The interface between the VAX-11/730 and the CAMAC interface modules is a Bi-Ra Microprogrammable Branch Driver (MBD-11). During data acquisition event by event data were written to magnetic tapes which were later copied to DAT-tapes for off-line analysis. An on-line graphics computer terminal provided color screen monitoring of the recorded spectra.

(b) Computer Software

The data acquisition system XSYS on the VAX-11/730 provides the necessary computer software for all the experimental data handling at the National Accelerator Centre (NAC). Before acquiring data the computer software was set up in the following way. After initializing XSYS the required data areas for gates, histograms and scalers were allocated. A Data Acquisition Program (DAP) was implemented and an EVAL program was loaded for event analysis.

i. Memory Allocation

Eleven one-dimensional histograms, which consisted of 1024 channels were allocated to hold prescaled singles events, and pulser events for the four detectors, as well as energy spectra for the ejected particles, in this case α and ^3He particles. The data areas which were defined for data acquisition purposes are presented in Table 2.2.

For particle identification two two-dimensional histograms were allocated (64×64). One corresponded to the low energy events (A vs B), while the other corresponded to the high energy events (B vs C). A third two-dimensional histogram was allocated (128×128) to hold the Mass versus Energy spectrum which provided better particle separation for the low energy events. (Chapter 4)

Various data areas had to be allocated for the one, as well as two-dimensional gates needed during the data analysis.

ii. Data Acquisition Program DAP

The actual data acquisition is controlled by a sorting subprocess called XSORT. This subprocess reads both the DAP and the Event Analysis Language (EVAL) files. The DAP file provides the necessary CAMAC commands which are used by the MBD to initialize, start, and stop runs.

iii. Event Analysis Language EVAL

The EVAL program provides the language for sorting the data either on-line or off-line with the VAX computer. The contents of the EVAL and DAP files are determined by the experimental configuration used.

Name	Type	Size	Description
A	1D	1024	Single A events
B	1D	1024	Single B events
C	1D	1024	Single C events
D	1D	1024	Single D events
Pattern	1D	256	Pattern Register
APulser	1D	1024	Pulser events
BPulser	1D	1024	Pulser events
CPulser	1D	1024	Pulser events
DPulser	1D	1024	Pulser events
Helions	1D	1024	Energy spectrum
Alphas	1D	1024	Energy spectrum
AB	2D	64x64	PID - spectrum
BC	2D	64x64	PID - spectrum
BCD	2D	64x64	PID - spectrum
AME	2D	128x128	PID - spectrum
GTABH	2D	GATE	Helion gate
GTABA	2D	GATE	Alpha gate
GTBCH	2D	GATE	Helion gate
GTBCA	2D	GATE	Alpha gate
GTAMEH	2D	GATE	Helion gate
GTAMEA	2D	GATE	Alpha gate

Table 2.2 List of data areas generated for data analysis

8. Experimental Procedure

The detector telescopes were mounted inside the scattering chamber as shown in figure 2.7. In the data room the necessary Nuclear Instrumental Modules (NIM) were set up, as prescribed by the linear and logic circuits, which were linked to the corresponding CAMAC interfaces.

The initial duty of the beamline operators, who delivered a 200 MeV proton beam, was to centre the beam on the target by making use of a ruby target. A television camera was used to monitor the process of focussing and centring the beam.

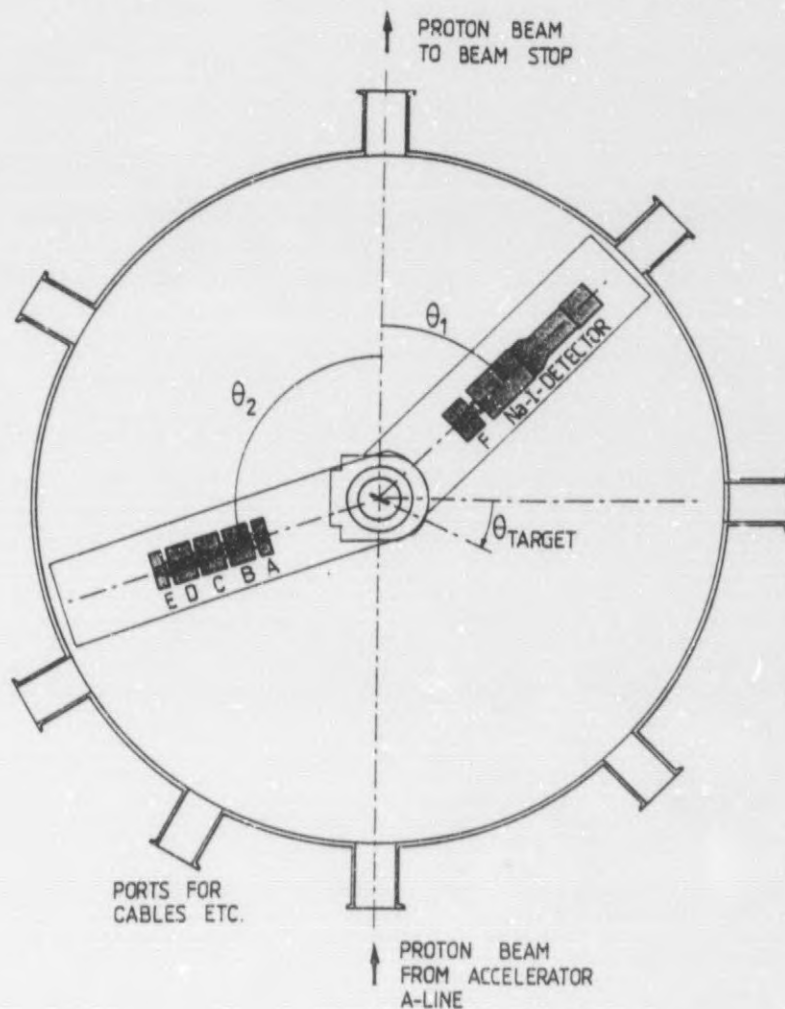


Figure 2.7 Aerial view of detector and target geometry

The elastic scattering of protons and deuterons off a target was used to finetune the electronic components, to determine the beam offset, and to calibrate our detector telescope (see Chapter 3). It was therefore necessary to make two-body kinematic calculations for both protons and deuterons for use during the energy calibration measurements. For this purpose a computer program called KINMAT was used.

The ΔE detector was also calibrated at the end of the experiment with a ^{228}Th source, which emits α particles of known energies.

CHAPTER THREE

DATA ANALYSIS

DATA ANALYSIS

1. Particle Identification

The main objective during the replay of the experimental data was to extract the measured α and ${}^3\text{He}$ energy spectra. All events were sorted according to the EVAL sorting routine, in which a distinction is made between α and ${}^3\text{He}$ particles. The distinction is based on the setting of two dimensional gates on the appropriate two dimensional histograms.

From the Bethe-Bloch formula [16] we know that the stopping power is proportional to the charge, z , of the detected particle, and inversely proportional to the velocity, v , of the detected particle, and the mass, m , of an electron i.e

$$-\frac{dE}{dx} \propto \frac{z^2}{mv^2}$$

By using the $\Delta E - E$ technique, which considers the energy loss in two adjacent detectors, we were able to identify the detected particles as each particle gives rise to a distinct locus on the two dimensional $\Delta E - E$ spectrum. By setting gates on these spectra we were able to extract data corresponding to the particle of interest. (figure 3.1).

For analysis we made use of two $\Delta E - E$ histograms. One was generated for detectors A and B, and another for detectors B and (C .AND. D). The first histogram attributed to the low energy part of the energy spectrum, whilst the latter attributed to the high energy part of the energy spectrum. The first histogram was incremented by the detection of low energy events, which did not give a good separation between the particles for absolute gate settings. In order to improve the separation, and hence the gate setting, a second histogram was generated. A Mass versus Energy Spectrum (*MvsES*) was generated in which the mass was calculated by using the following expression:

$$\text{Mass} = (A + B)^{1.7} - B^{1.7}$$

where

A and B refer to the energy deposited in detectors A and B.

Two dimensional gates could then again be set around the particles of interest. (figure 3.2)

The gates on the *MvsES* and the $\Delta E - E$ spectrum were then used to increment the energy spectra for the α and ${}^3\text{He}$ particles. The *MvsES* provided the low energy part where as the $\Delta E - E$ provided the high energy part of the spectrum.

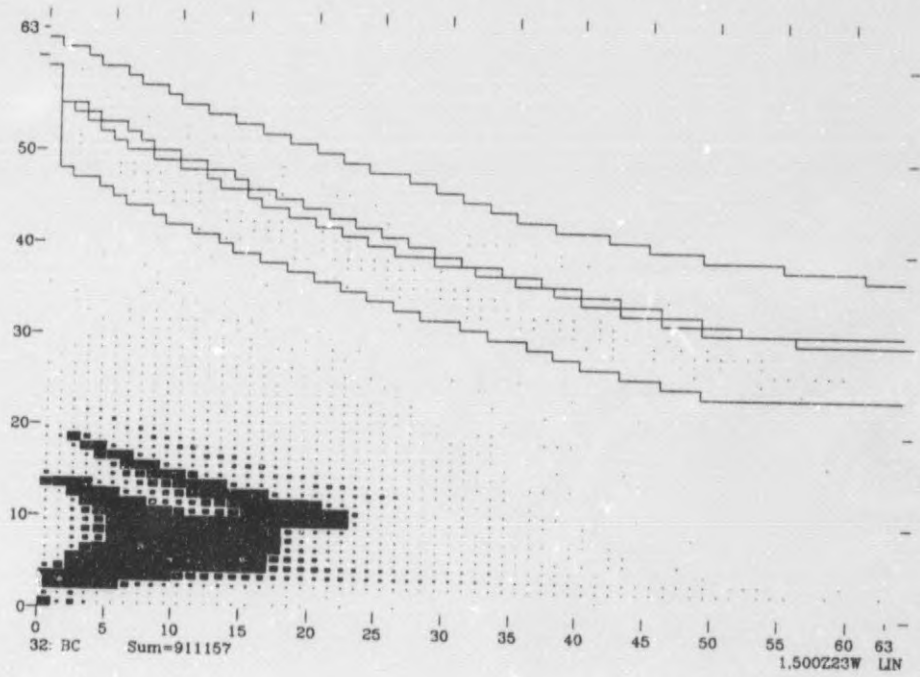


Figure 3.1 *PID spectrum used for identification of high energy α and ^3He particles*

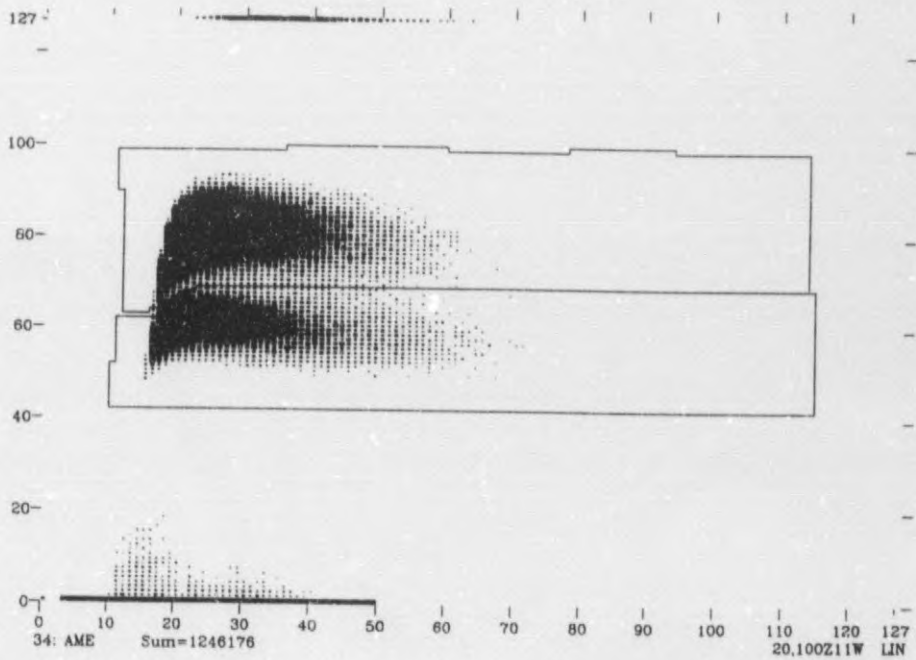


Figure 3.2 *PID spectrum (MvES) used for identification of low energy α and ^3He particles*

2. Beam Direction

To determine the difference between the direction of the beam and the zero alignment of the detector arms in the scattering chamber, the fact that elastic scattering of unpolarized protons is symmetric about the beam direction, was used. Data were acquired at -20° . The detector telescope was then moved to the opposite side of the beam. The ratio of the number of counts in the elastic peak to the inhibited integrator counts were calculated and compared for the two situations. The ratio at -20° was found to be in agreement with the ratio at $+19.4^\circ$. This meant that our beam offset was 0.3° . This offset was taken into account when the detector telescope was positioned.

$$\theta(\text{reading}) + 0.3 = \theta(\text{true})$$

3. Energy Calibration

For the calibration of the $150\ \mu\text{m}$ Si-detector a ^{228}Th -source, which emits α particles with discrete energies, was used. The channel numbers, corresponding to each peak, were determined and a linear fit could be made on the energy versus channel number data. The calibration curve is shown in figure 3.3.

The following relation was obtained:

$$E = 0.026 \times \text{Channel} - 0.04$$

The calibration of the other detectors was done by considering the elastic scattering of protons and deuterons in the following two reactions:

(a) $p(p,p)p$

(b) $d(p,d)p$

In both cases the scattered particles were detected in coincidence in order to eliminate background from the spectrum. For the coincidence measurement a second detector telescope was used which consisted of a $1000\ \mu\text{m}$ Si detector and a NaI detector. A second collimation system was used which consisted of the same components as that used during the first experiment, except that the diameter of the tantalum collimator was reduced to 3 mm. (figure 3.4)

The reduced diameter subtended a smaller solid angle, which ensured better energy resolution. The timing signal of the silicon detector was used in the logical electronics while the NaI detector served as a stopping detector.

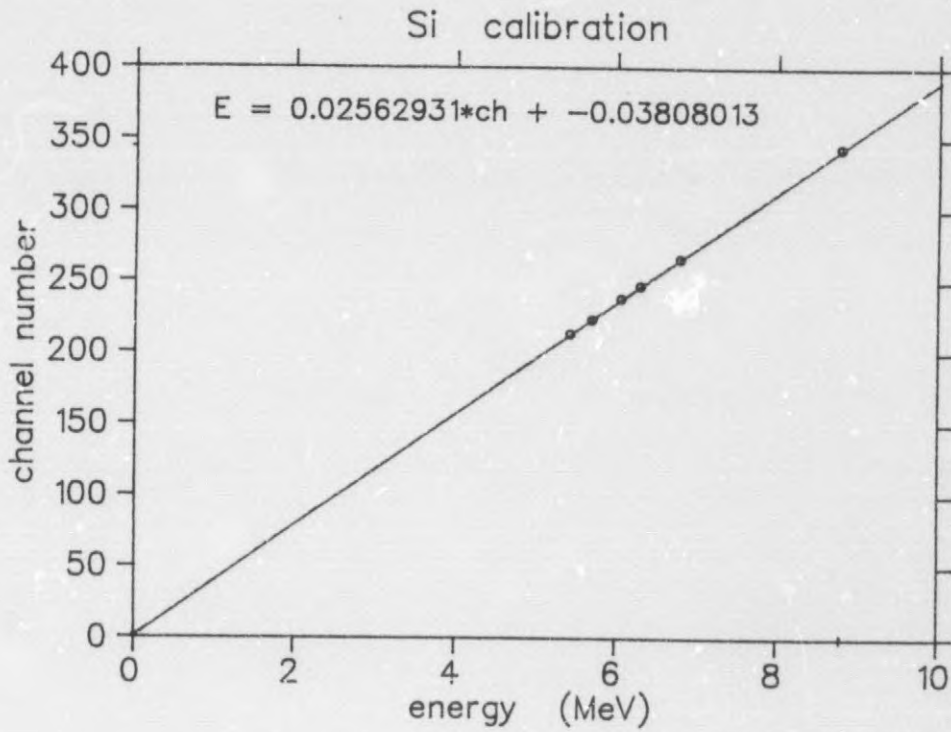
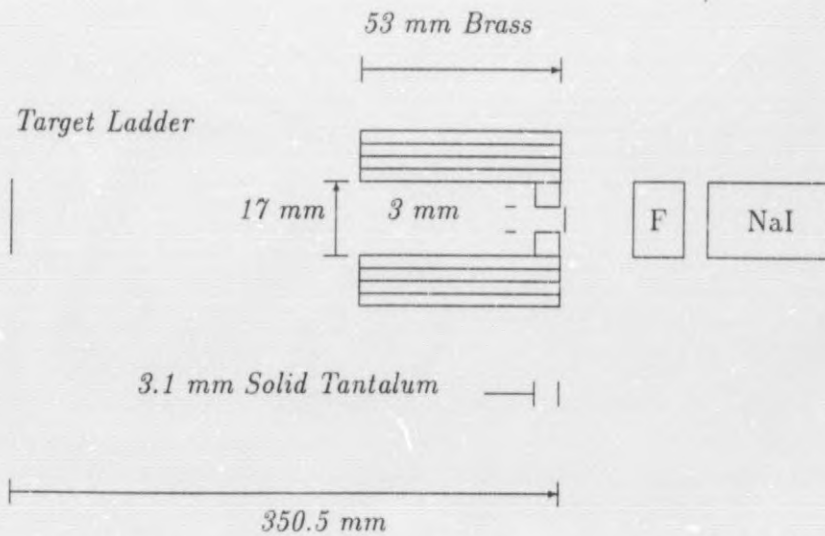


Figure 3.3 Energy calibration for the 150 μm detector



F: 1000 μm Si detector

Figure 3.4 Cross section of the experimental set-up for the second detector telescope. 13 μm Mylar foil over exit hole of collimator.

A diagram of the electronics used for the second telescope is given in figure 3.5.

A computer program, KINMAT, was used to calculate the two-body kinematics which provided a relation between the observed energy and the detection angle. An event was considered valid if it corresponded to the following situation:

$$F \cap (B \cap (A \cup C)),$$

where F indicates the Si detector in the second telescope.

A linear fit was done on the energy versus channel number data. The following dependences were obtained for the three detectors:

- (a) B: $E = 0.063 \times \text{channel} + 0.146$
- (b) C: $E = 0.065 \times \text{channel} + -0.115$
- (c) D: $E = 0.057 \times \text{channel} + -0.025$

Our energy calibration gave us a method of quantitatively calculating the dead layers of the various detectors. Figures 3.6 to 3.11 show the energy calibration curves before and after the dead layer corrections based on elastic $p - p$ scattering. The results obtained from the use of elastic deuteron scattering gave us the same calibration parameters.

With the aid of these dependences we were able to calculate the energy deposited in the various detectors.

4. Corrections built into the Analysis

It was necessary to take two types of correction factors into account during our analysis namely: Computer and electronic dead time and dead layer correction factors.

(a) Computer and Electronic Dead Time Corrections

The largest contribution to dead time comes from the ADC conversion time plus the time required by the computer to read the event data. The computer automatically corrects for the dead time losses by providing a busy signal which inhibits the acquisition of data, as this busy signal acts as a veto signal. The computer dead time is properly accounted for by using the effective accumulated charge in calculating the absolute cross section.

The electronic dead time was determined by comparing the number of processed pulser events which appear in two dimensional pulser histograms and the inhibited pulser scaler. For this analysis pulser histograms were generated for A versus B and B versus C, where the alphabetic characters refer to the detectors in the detector telescope. Two dimensional gates were set around the blobs on the two dimensional histograms. (figures 3.12 and 3.13)

By using the two histograms the total average dead time was calculated by using the following formula:

$$\text{Dead time} = D = 0.5 \times [AB + BC]$$

where

AB is the dead time for the first histogram and BC the dead time for the second histogram.

The experimental data were then corrected for dead time effects by dividing the number of counts with $(1 - D)$.

(b) Dead Layer Corrections

Due to the presence of dead layers on the detectors, the energy loss measured is not the true energy of the detected particle. It was therefore necessary to incorporate corrections into our analysis.

From the energy calibration we obtained approximate values of the dead layers for the detector telescope. Our aim with the detector calibration was to obtain a calibration with an offset of zero. This would mean that channel zero corresponded to zero energy.

The method of energy calibration followed was to view the detectors in front of the detector being calibrated as contributing to the inactive medium of the detector. The inactive layer was adjusted until a zero offset was obtained. The inactive layer was calculated with a computer program called ELOSS. This program calculates the energy loss due to a given thickness of matter. By adjusting the thickness of the matter, in this case silicon, the energy loss could be obtained. By subtracting this value from the energy deposited in the detector, we were able to get calibrations with offset parameters of approximately zero.

For the calibration of detector B we had to provide an inactive layer of $235 \mu\text{m}$. Similarly we obtained inactive layers of 5.12 mm for detector C and 9.84 mm for detector D. The values of the inactive layers should not be seen as the dead layers of the various detectors, but rather as the inactive medium in front of the specific detector as illustrated in figure 3.14.

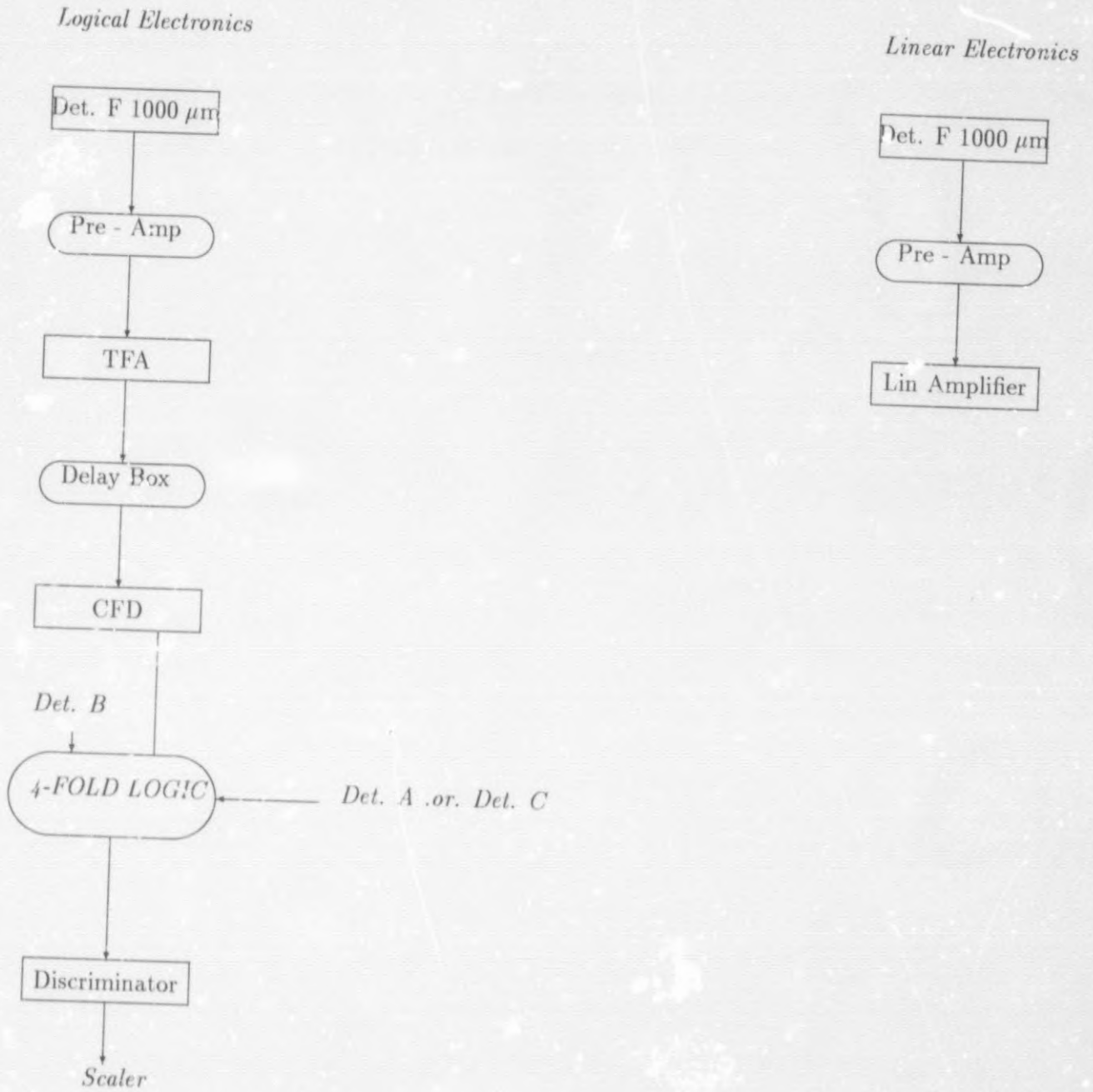


Figure 3.5 *Linear and Logical Electronics for second detector telescope. This telescope was used during the calibration of our detectors.*

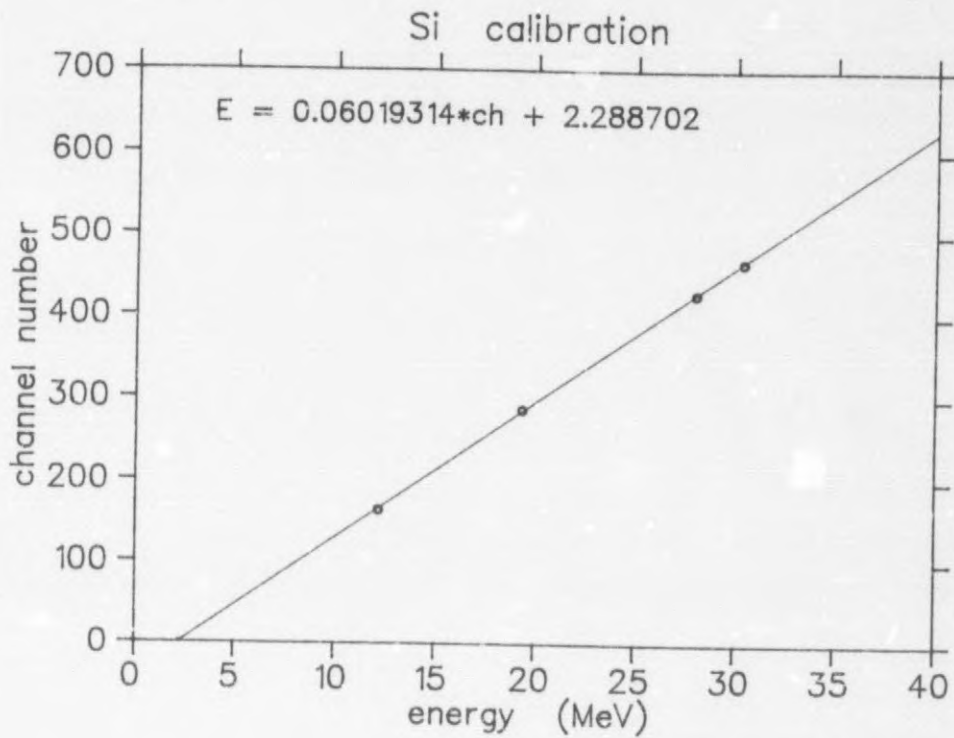


Figure 3.6 Energy calibration for B detector without Dead layer corrections

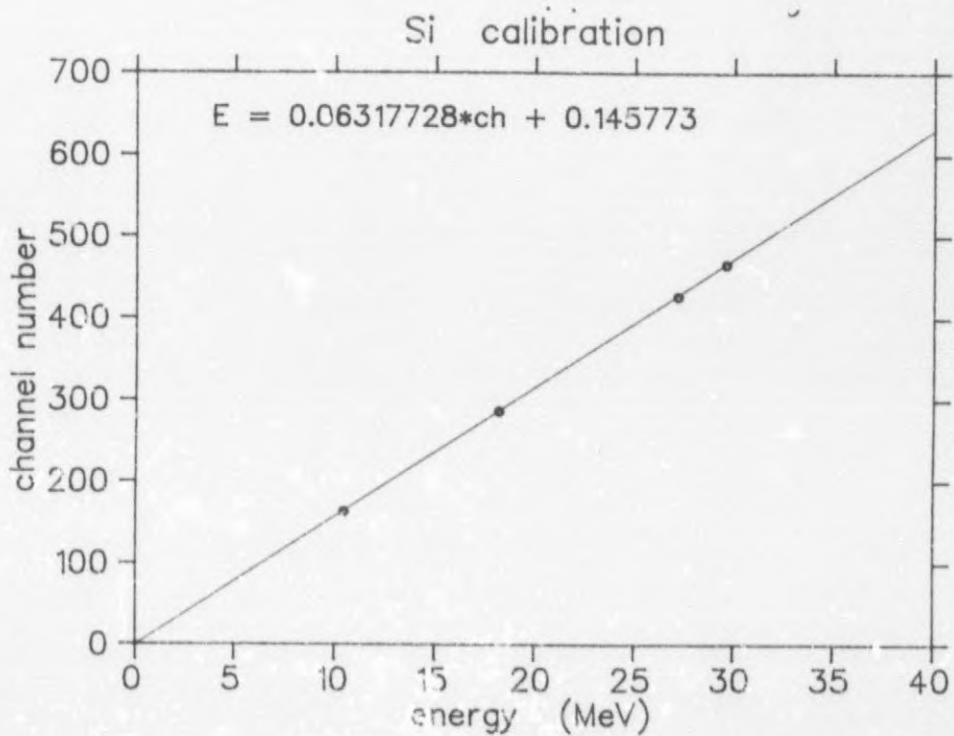


Figure 3.7 Energy calibration for B detector with dead layer corrections

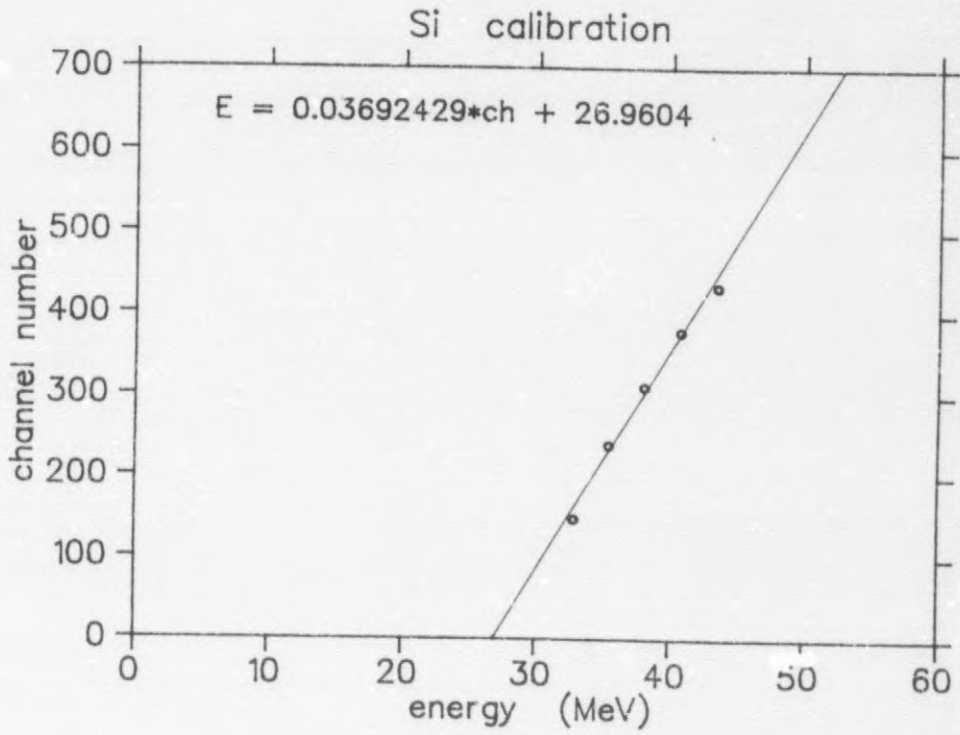


Figure 3.8 Energy calibration for C detector without dead layer corrections

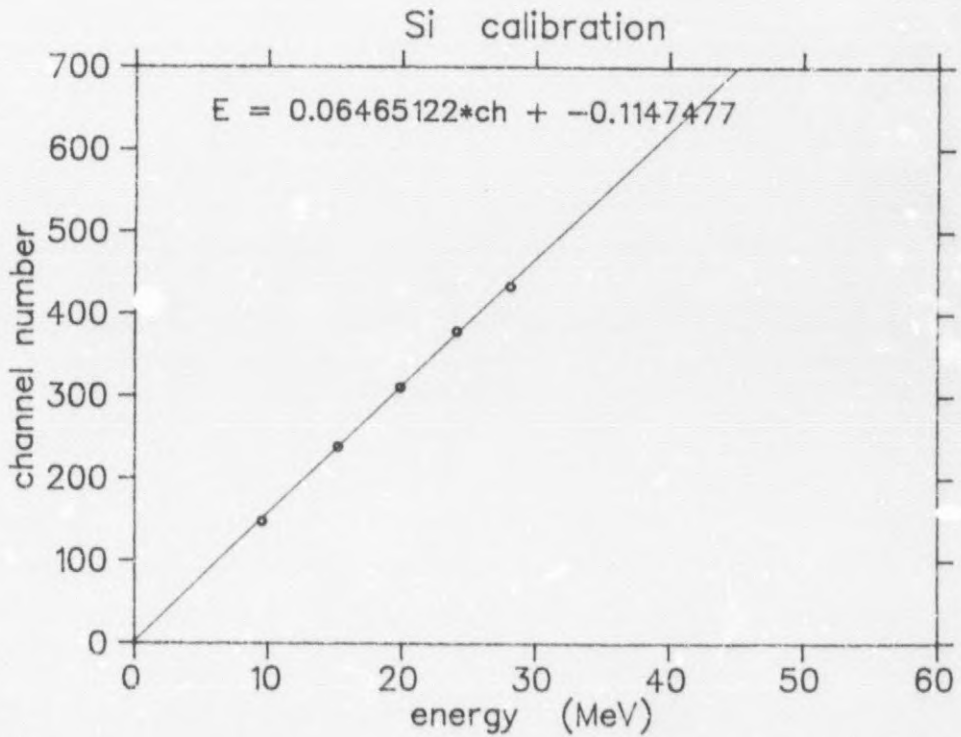


Figure 3.9 Energy calibration for C detector with dead layer corrections

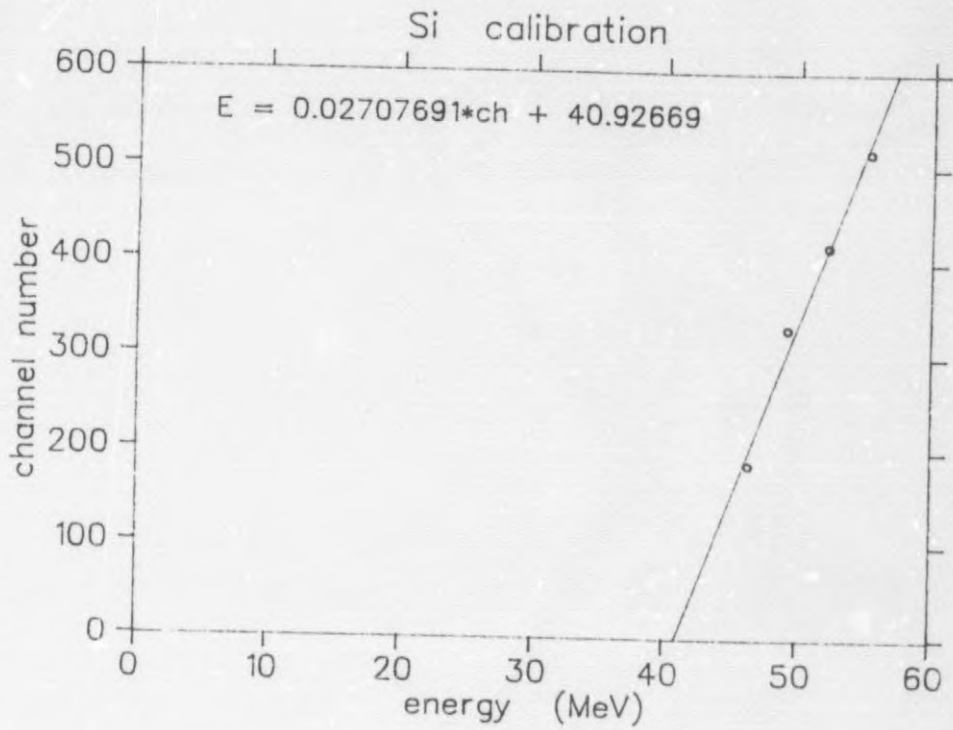


Figure 3.10 Energy calibration for D detector without dead layer corrections

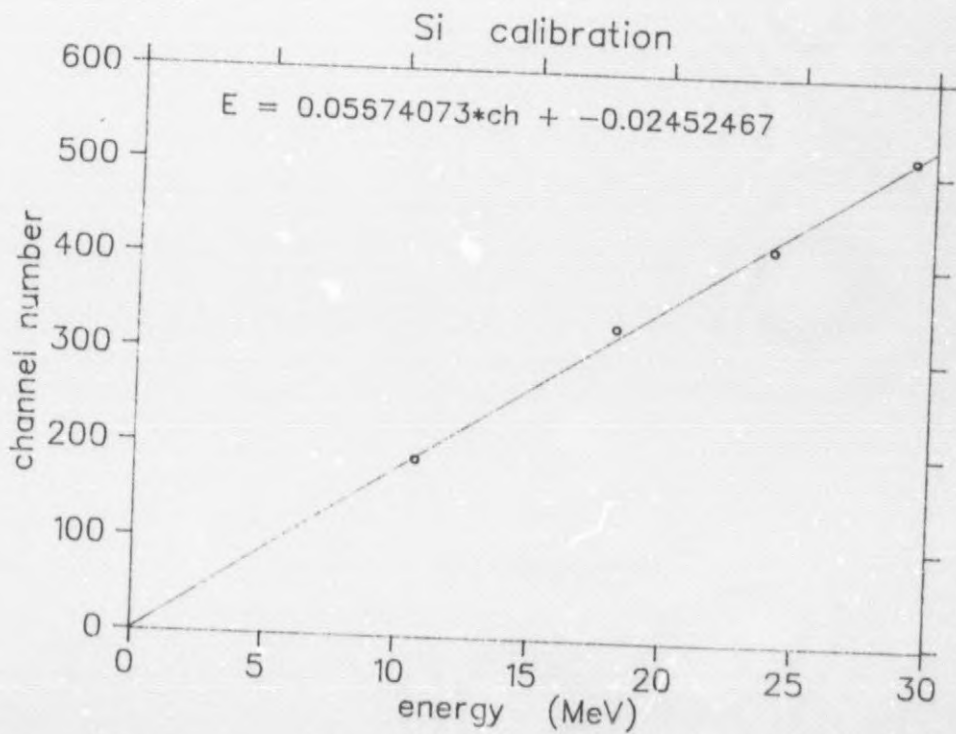


Figure 3.11 Energy calibration for D detector with dead layer corrections

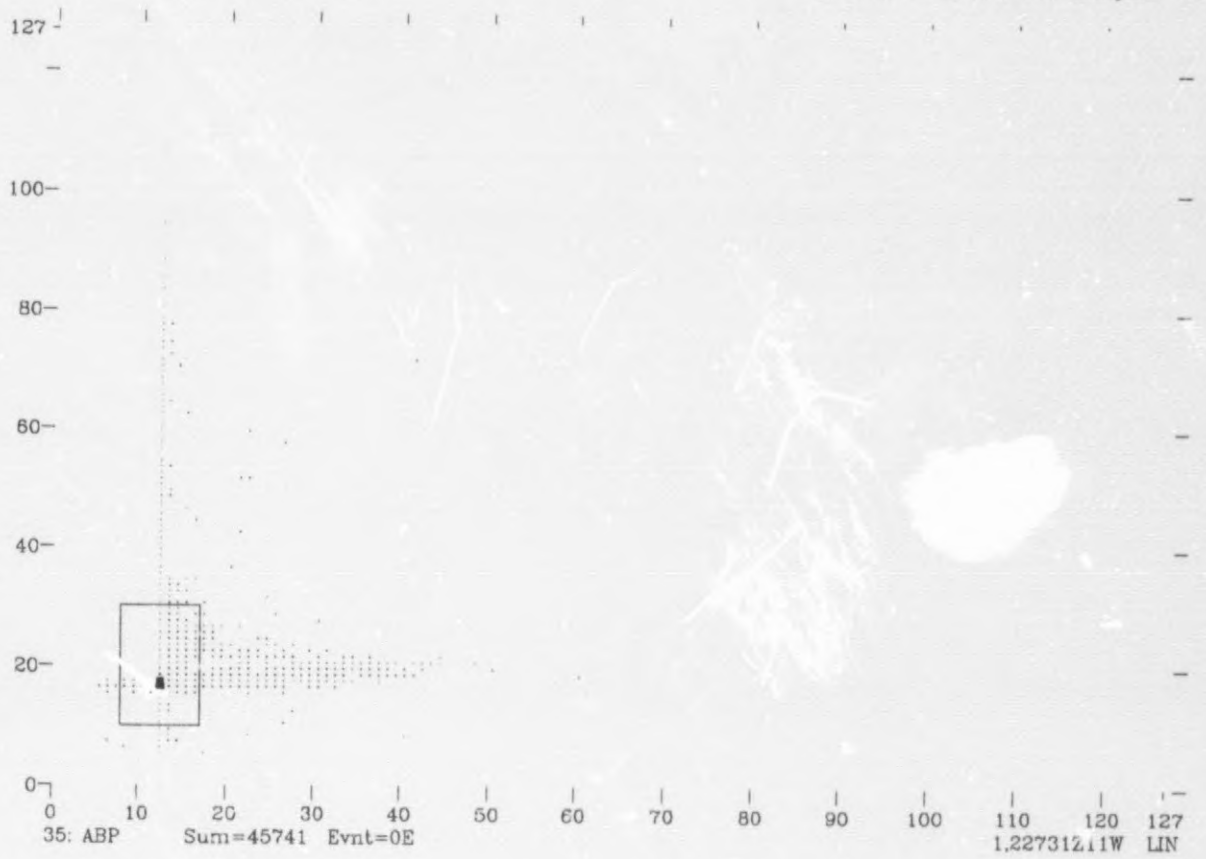


Figure 3.12 Two dimensional pulser histogram for A vs B

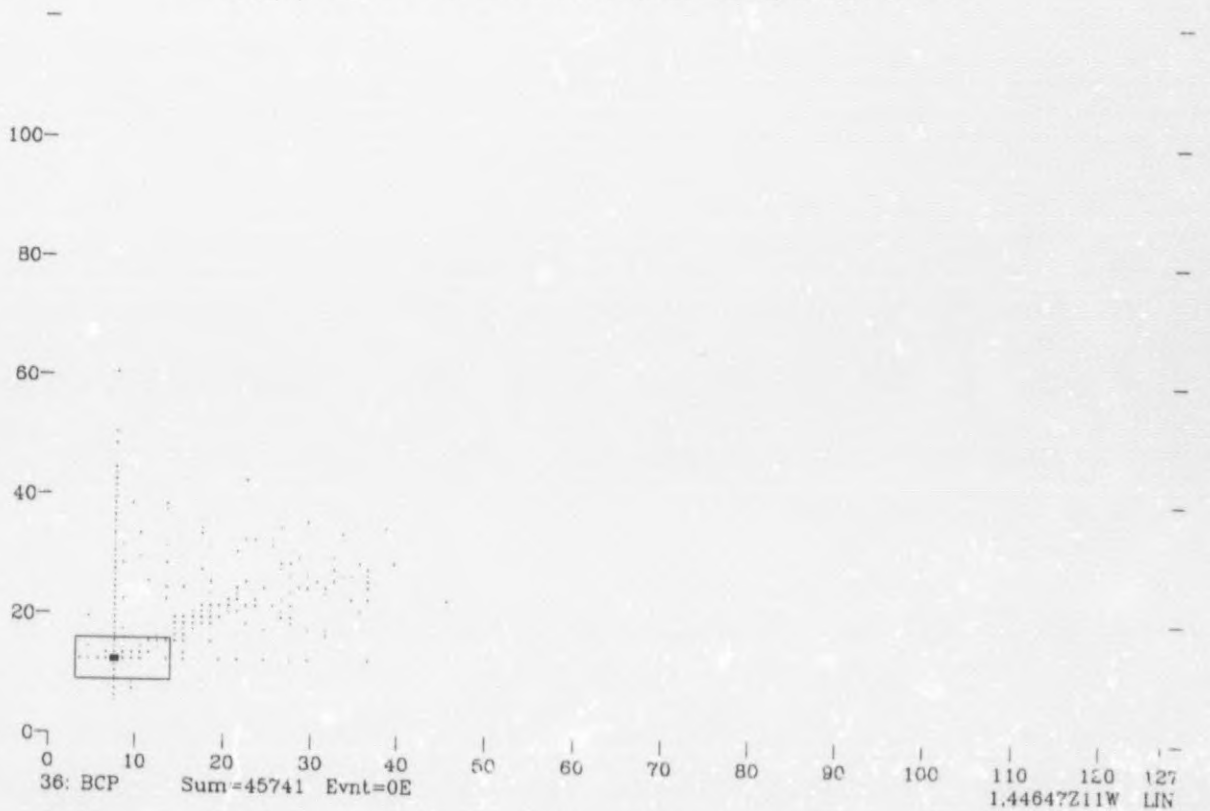


Figure 3.13 Two dimensional pulser histogram for B vs C

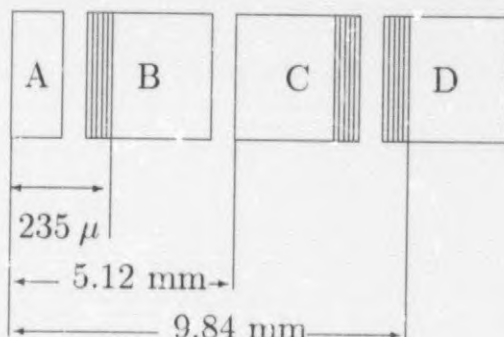


Figure 3.14 *Calculated dead layers for various detectors. The first detector corresponds to the 13 μm Mylar foil.*

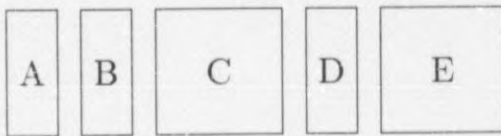
In our detector configuration detector B and detector C were placed with their significant dead layers facing forward and backward respectively as shown in figure 3.14. The dead layers on the other two surfaces of detectors B and C, typically $\simeq 0.1 \mu\text{m}$, were ignored for all practical purposes. Similarly detector D was placed with its significant dead layer also facing forward as indicated in figure 3.14.

From figure 3.14 the following deductions can be made:

- i. detector B has an approximate dead layer of $85 \mu\text{m}$ with an active medium of approximately 4.885 mm
- ii. the active medium of detector C together with the dead layers of C and D is 4.72 mm, which implies that detector C has a physical thickness of less than 5 mm

For the purpose of calculating the dead layer correction factors we viewed detectors B and C as forming a single detector with an active medium of 9.26 mm. We introduced a dead layer of 0.13 mm for detector D with an active medium of 10 mm as illustrated by figure 3.15. The approximations made for the dead layers contribute to the systematic error of our final results, via the energy calibration.

Using a computer program called KINMAT we were able to calculate the energy loss in the dead layers as opposed to that lost in the active medium of the detectors for both α and ${}^3\text{He}$ particles.



- A 150 μm detector
- B 85 μm dead layer
- C 9.26 mm detector
- D 130 μm dead layer
- E 10 mm detector

Figure 3.15 *Detector set up for dead layer corrections*

Functional fits were then generated for the data obtained by the KINMAT calculation. It was necessary to fit two functions, one to the upper part and one to the lower part, of the data, as displayed in Figures 3.16 and 3.17.

The following fits were obtained:

$$\Delta E(\text{Upper}) = \frac{a + cx + ex^2}{1 + bx + dx^2}$$

and

$$\Delta E(\text{Lower}) = \frac{a + bx + c}{\sqrt{x}} + \frac{d}{x^2}$$

A Fortran program could then be written with which we corrected the data for dead layer effects, where:

$$[\text{Corrected value} = \text{Old Value} + \Delta E].$$

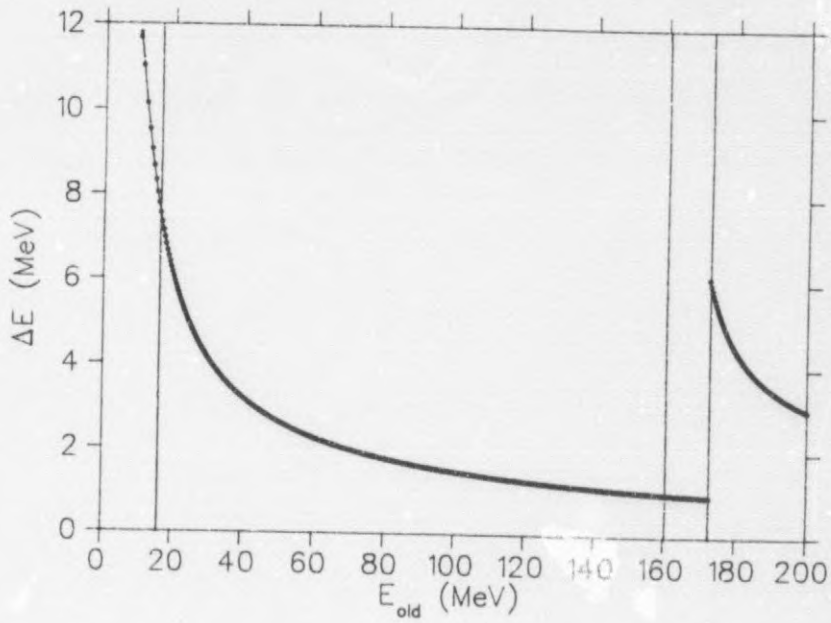


Figure 3.16 Dead layer correction function for the (p, α) reaction.

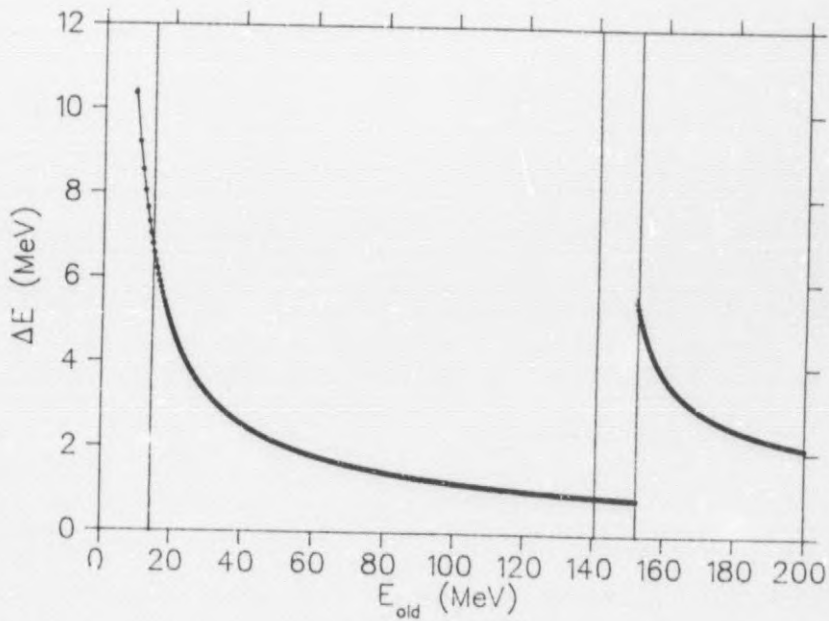


Figure 3.17 Dead layer correction function for the (p, ^3He) reaction

5. Absolute Cross Section

The number of counts in the analyzed spectra had to be converted to an absolute cross section in the laboratory frame of reference. This was done by multiplying the number of counts with a conversion factor. The scattering cross sections for the α and ^3He particles were determined by using the following formula:

$$\frac{d^2\sigma}{d\Omega dE} = \frac{N \times 10^{27}}{N_{cii} \times N_0 \times \Delta\Omega \times \Delta E}$$

N - Corrected number of counts

$\Delta\Omega$ - Solid angle

ΔE - Width of Energy bin (MeV)

N_0 - Number of target nuclei/cm²

N_{cii} - Number of incident projectiles on target

$$N_0 = \frac{t \times 10^{-3} \times 6.023 \times 10^{23}}{4 \times \cos\theta_{tgt}}$$

where

A is the molar mass

t the target thickness in mg/cm²

and θ_{tgt} the target angle.

$$N_{cii} = (\text{charge})/e = \frac{Q \times 10^{-9}}{1.602189 \times 10^{-19}}$$

with Q in nC

After making all the necessary substitutions the equation becomes the following:

$$\frac{d^2\sigma}{d\Omega dE} = \frac{0.2462069 \times N \times A \times \cos\theta_{tgt}}{t \times Q \times \Delta\Omega \times \Delta E}$$

6. Error Analysis

(a) Statistical Errors

In the spectra presented in the next chapter error bars are indicated for cases in which the error bar is greater than the symbol size used. The error bar corresponds to the statistical error, which was calculated as being the \sqrt{N} , where N is the number of counts in each bin. By using the formula for error propagation [16], the error was propagated in all the operations that were performed on the data.

(b) Systematic Errors

In this subsection we attempt to summarize the uncertainties which we feel contribute to the systematic error.

i. Target Thickness

A substantial contribution to the total systematic error comes from the uncertainties in the thickness of the three targets used during our experiment. The uncertainties varied between 2% for ^{59}Co to 7% for ^{27}Al .

ii. Solid Angle

The uncertainty in the solid angle consisted of an uncertainty in the radius of the collimator opening, and the distance between the centre of the target and the centre of the collimator opening. The combined error was estimated from the uncertainties in the measured parameters. From an uncertainty of ~ 0.1 mm in the measured distance, and ~ 0.03 mm in the collimator's radius, the maximum uncertainty is about 1%.

iii. Energy Calibration

Our final energy calibration was obtained after the effect of dead layer energy losses had been taken into account. The program used to calculate the energy loss, ELOSS, has a 2% accuracy. The uncertainty in energy calibration eventually resulted in a combined error in the energy scale of a particular spectrum.

iv. Particle Identification

An accurate calculation of the cross section is based on the setting of accurate gates on the PID spectra. Upon setting the gates, there is an uncertainty connected to whether or not we are including particles that we should not include, and excluding particles that we should not exclude. This uncertainty due to the setting of the gates constitute an error of $\sim 5\%$ [17]

v. Electronic Dead Time

The uncertainty which is related to the correction of the cross sections for electronic dead time is estimated to be less than 2% [17].

A realistic estimate for the total systematic error is obtained if we apply the formula for error propagation for addition [16] to the errors of the various factors which contribute to the systematic error. Table 3.1 reflects the various contributors to the systematic error.

7. Energy Spectra and Angular Distributions

After setting the gates around the α and ^3He particles in the particle identification (PID) spectra, the contents of the gates were used to increment

Contributors	Error in %
Target Thickness	
^{27}Al	7
^{59}Co	2
^{197}Au	3
Solid Angle	1
Energy Calibrations	4
Particle Identification	5
Electronic Dead Time	2
Total Systematic Error	10

Table 3.1 Summary of systematic errors

one dimensional energy spectra, which is a graphical representation of the number of counts in the different channels.

The absolute cross section was then obtained by multiplying the corrected number of counts per channel with a normalization factor as described in section 3.5.

Angular distributions were obtained by making a 5 MeV cut at the desired ejectile energies, for the reactions (p, α) and $(p, {}^3\text{He})$ on ^{27}Al , ^{59}Co , and ^{197}Au .

In the next chapter we calculate the angular distributions by making use of the phenomenological parametrization of Kalbach.

CHAPTER FOUR
THEORETICAL CALCULATIONS

THEORETICAL CALCULATIONS

Kalbach's Phenomenological Parametrization.

1. Basis for Angular Systematics

It has been established that pre-equilibrium processes play an important role in nuclear reactions induced by light projectiles. A characteristic feature of the particle emission from the composite nucleus, before the attainment of equilibrium, is the emission of high energy particles with angular distributions peaked in the forward direction.

The overabundance of high energy particles is due to the fact that the nuclear excitation energy is shared amongst only a few degrees of freedom during the early stages of the reaction when pre-equilibrium emission occurs. The partial preservation of the incident projectile's direction causes the angular distribution to be peaked in the forward direction.

Both quantum mechanical and semi-classical theories have been developed to account for the observed systematics of pre-equilibrium emission.

The quantum mechanical approaches of Feshbach, Kerman, and Koonin (FKK) [9, 18], Tamura et al (TUL) [19], and Nishioka et al (NWY) [20] are able to describe the spectral shape and angular distribution of the emitted particles. Koning and Akkermans [21] have shown that the computational results of the various models, although physically very different, are roughly of the same quality.

The semi-classical exciton [6, 7, 8] and hybrid [22, 23, 24] pre-equilibrium models are able to describe the angle-integrated spectral shapes successfully, although it is found that in their usual formulation they cannot yield angular distributions directly.

Another approach which is often followed to reproduce the angular distributions is the phenomenological systematics of Kalbach [25]. It is found that these systematics are useful in predicting and describing the differential cross sections, although its basis in physics remains obscure.

The fact that the observed continuum pre-equilibrium cross sections vary smoothly with angle and energy, and lend themselves to simple parametrizations, suggests that we should be able to describe the cross sections using a simple model of the reaction process.

By using an exciton model, that explicitly conserves momentum and does not assume a leading particle, Chadwick and Obložinský [26] were able to derive theoretically Kalbach's parametrization of the forward peaking.

The derivation relies on the use of state densities with linear momentum in an exciton model. These densities describe the linear momentum structure of the phase space of excited particles and holes (excitons).

It is assumed that the incident nucleon interacts with the target nucleus to form a two-particle-one-hole (2p-1h) state, and in subsequent two-body nucleon-nucleon interactions the excited system may pass through more complex particle-hole configurations towards equilibrium. Particle emission can occur from the early pre-equilibrium stages and these particles typically contribute to the high energy part of the emission spectra. The model assumes that particle-hole states can be populated provided that both energy and momentum is conserved. Furthermore the "memory" of the initial projectile's direction is not maintained solely by a fast leading-particle, but rather carried by excited particles and holes during pre-equilibrium cascade. By explicitly conserving linear momentum they obtained a rate of emission with energy ϵ and direction Ω given by:

$$\frac{d^2\Lambda_n}{d\epsilon d\Omega} = \frac{2m\epsilon\sigma_{inv}R(p)}{\pi^2\hbar^3} \frac{\rho(p-1, h, E - \epsilon_\Omega, \mathbf{K} - \mathbf{k}_\Omega)}{4\pi\rho(p, h, E, \mathbf{K})} \quad (0.1)$$

where

m - ejectile mass

σ_{inv} - reaction cross section for inverse process

E - composite system's total Energy before emission

\mathbf{K} - composite system's total momentum before emission

$E - \epsilon_\Omega$ - residual nucleus energy relative to the bottom of the nuclear well

$\mathbf{K} - \mathbf{k}_\Omega$ - residual nucleus momentum relative to the bottom of the nuclear well

$\epsilon_\Omega = \epsilon + B_{em} + \epsilon_F$

ϵ_F - Fermi energy

B_{em} - emission particle's separation energy

$k_\Omega = \sqrt{2m\epsilon_\Omega}$

$R(p)$ - correction factor accounting for neutron-proton distinguishability

It is possible to write the state densities with linear momentum as the product of an energy-dependent state density and a linear momentum distribution, [27]

$$\rho(p, h, E, \mathbf{K}) = \rho(p, h, E)M(p, h, E, \mathbf{K}) \quad (0.2)$$

An advantage of using this construction is that they were able to use a form of the energy-dependent state density $\rho(p, h, E)$ which includes Pauli blocking effects fully.

In a semi-classical model of the nucleus the individual particles and holes have definite values of linear momentum. This state density is composed of an ensemble of $p-h$ states in which the single-particle momenta are oriented in random directions. The summed momenta for each state yields a specific total momentum \mathbf{K} , whilst the ensemble of states result in a distribution of the momentum \mathbf{K} . By applying the central limit theorem from statistics they were able to obtain an expression for the momentum distribution,

$$M(p, h, E, \mathbf{K}) = \frac{1}{(2\pi)^{3/2}\sigma^3} \exp\left(\frac{-K^2}{2\sigma^2}\right) \quad (0.3)$$

where σ^2 represents the width of the distribution.

In semi-classical pre-equilibrium theories the emission cross sections are calculated by applying detailed balance, and making use of $p-h$ state densities. The principle of detailed balance states that two systems a and b , with state densities ρ_a and ρ_b , are in statistical equilibrium when the depletion of the states of system a by transitions to system b , equals their increase by the time-reversed process $b \rightarrow a$ [8].

If state densities with linear momentum are used we obtain angle dependent emission rates, and can therefore obtain angular distributions directly.

Since the cross section for pre-equilibrium emission is proportional to the emission rate, this enables us to write the double differential cross section as:

$$\frac{d^2\sigma}{d\epsilon d\Omega} = \frac{d\sigma}{d\epsilon} G(n, \theta) \quad (0.4)$$

where

$G(n, \theta)$ - Angular distribution kernel

$\frac{d\sigma}{d\epsilon}$ - Angle integrated cross section

The following expression for the angular distribution kernel was obtained by Chadwick et al [26]:

$$G(n, \theta) = \frac{1}{4\pi} \frac{2a}{e^a - e^{-a}} \exp(a \cos \theta) \quad (0.5)$$

$$a = \frac{3Kk_{\Omega}}{2nm\epsilon_{av}} \quad (0.6)$$

where the parameters have the following meaning:

K : Projectile's momentum measured from bottom of the nuclear well
 k_{Ω} : Ejectile's momentum measured from the bottom of the nuclear well

n : Number of excitons = $p + h$

m : Mass of the ejectile

ϵ_{av} : Average excitation energy relative to the bottom of the nuclear well

θ : Scattering angle

a : Slope parameter

Writing, a , in terms of channel energies we obtain:

$$a = \frac{3\sqrt{(\epsilon_{in} + B_{in} + \epsilon_F)(\epsilon + B_{em} + \epsilon_F)}}{\zeta n \epsilon_{av}} \quad (0.7)$$

where the parameters have the following meaning:

ϵ_{in} : Incident energy

B_{in} : Separation energy of projectile

ϵ : Ejectile energy

B_{em} : Separation energy of ejectile

ζ : Energy dependent factor to account for other quantum effects such as refraction and diffraction from the nuclear potential.

Features of the Angular Distributions:

- (a) Angular distribution applies to each pre-equilibrium stage component.
- (b) Conservation of linear momentum is maintained for all orders of scattering.
- (c) Forward peaking increases with incident and emission energy, and decrease with increasing number of excitons. As the number of excitons increase, we find that the incident momentum is shared amongst more particles and holes.

The work done by Chadwick et al [26] provides a framework for beginning to understand some of the unexplained features of the Kalbach Parametrization, such as:

- (a) Independence of slope parameter on incident energy less than 130 MeV.
 - would arise by the approximate cancelling of the incident energy dependence with the increasing number of stages, each with a flatter angular distribution.
- (b) Independence of slope parameter on projectile mass for energies less than 130 MeV.
 - a increases as the mass increases, but is partially compensated by the increasing number of excitons.

2. Kalbach's Parametrization [25]

(a) Overview

In 1981 the Kalbach Mann (K-M) [28, 29] systematics was published which described the shapes of the angular distributions for inclusive reactions at incident energies up to 80 MeV and emission energies up to 60 MeV. It was found that the angular dependence was primarily determined by the energy of the emitted particle, to first order, and the fraction of the time that it was emitted in a multistep direct (MSD) process as opposed to a multistep compound (MSC) process.

The observed systematics were parametrized in terms of Legendre polynomials using a small number of parameters.

The K-M systematics however had problems in reproducing angular distributions at both high and low-emission energies. At high emission energies the MSD angular distribution becomes strongly forward-peaked and it becomes difficult to reproduce the smooth behavior using Legendre polynomials. At the other extreme the systematics do not predict isotropy of the angular distributions as the energy approach zero.

An additional disadvantage of the K-M systematics is that second order dependencies on other reaction parameters could not be studied.

An improvement of the K-M systematics was made possible by the availability of a broader data base, a mathematical form to replace the Legendre polynomials and reasonable behavior at low emission energies.

(b) Improved Parametrization

The Legendre polynomials were replaced by an expression which incorporates exponential decay as a function of angle. An exponential in $\cos\theta$ was introduced as it yields a smooth turnover of the cross section of 0° and 180° and since the solid angle element is written as

$$d\Omega = d \cos \theta d\phi \quad (0.8)$$

The mathematical form of the MSD part is given by:

$$\frac{d^2\sigma}{d\Omega dE} = \frac{1}{4\pi} \frac{d\sigma}{dE} \frac{2a}{e^a - e^{-a}} \exp(a \cos \theta) \quad (0.9)$$

where

θ is the scattering angle in the centre of mass frame.

According to the K-M systematics the slope parameter, a , should to first order be a function only of the energy parameter $e_b = E_b + B_b$, where e_b is the kinetic energy of the particle in the exit channel and B_b the binding energy of the emitted particle in the composite nucleus.

Retaining the same parameters, but requiring that the MSC part be symmetric about 90° we obtain:

$$\frac{d^2\sigma}{d\Omega dE} = \frac{1}{4\pi} \frac{d\sigma}{dE} \frac{a}{e^a - e^{-a}} [\exp(a \cos \theta) + \exp(-a \cos \theta)] \quad (0.10)$$

As a test of both the MSD and the MSC parts of the angular distributions we demand that angle-integration gives the correct energy differential cross sections.

A general expression for the cross section as a function of scattering angle can be obtained by the addition of the above two equations. After addition we obtain:

$$\frac{d^2\sigma}{d\Omega dE} = \frac{1}{4\pi} \frac{d\sigma}{dE} \frac{a}{\sinh(a)} [\cosh(a \cos \theta) + f \sinh(a \cos \theta)] \quad (0.11)$$

The angle-integrated cross section $\frac{d\sigma}{dE}$ and the fraction, f , of the cross section which is multistep direct, is assumed to be known either from pre-equilibrium model calculations or from experiment.

(c) Parameters

The quantity e_b should represent the energy of the exit channel relative to the Fermi level of the emitting nucleus. As emission occurs from excited nuclei, in which the influence of pairing and shell structure on the position of the Fermi level have washed out, it was thought more appropriate to use a separation energy relative to the excited state Fermi level. To accomplish this change e_b was replaced by $e_b = E_b + S_b$, where S_b , the separation energy, is obtained from the liquid drop model with pairing and shell terms neglected. The expression used in calculating the separation energy can be found in [25].

The slope parameter, $a(e_b)$, have been described with a polynomial in e_b . The leading term was assumed to be linear to guarantee that calculated angular distributions at $e_b = 0$ be isotropic.

The second order dependencies with incident protons and the change in the primary parameter at incident energies above 100 MeV lead to the following relation:

$$a(e_b) = 0.040e_b + 1.8 \times 10^{-6}(e_b)^3 \quad (0.12)$$

It was however still necessary to improve the above expression in order to account for the observed second order dependencies on bombarding energy and emitted particle for nucleon induced reactions. This condition was met by introducing a third term which varies as $(\frac{e_b}{e_a})^4$

$$a(e_b) = 0.040e_b + 1.8 \times 10^{-6}(e_b)^3 + 1.9M_a m_b (\frac{e_b}{e_a})^4 \quad (0.13)$$

where

$$M_p = 1, m_\alpha = 2, m_{^3\text{He}} = 1$$

These equations are valid in the energy regime of 35–100 MeV. To avoid a whole new parametrization for nucleon induced reactions in the regime above 150 MeV, the parameter e_b in the first two terms were replaced by the ratio $X_1 = E_1 \frac{e_b}{e_a}$, where $E_1 = \min(e_a, E_{t1})$ and E_{t1} the transition energy. The third term was then recast to give it the same form as the first two, but with a lower transition energy, E_{t3}

Finally we obtain:

$$a(e_b, e_a) = 0.040X_1 + 1.8 \times 10^{-6}(X_1)^3 + 6.7 \times 10^{-7}M_a m_b (X_3)^4 \quad (0.14)$$

with :

$$X_1 = \frac{E_1 e_b}{e_a}, \quad X_3 = \frac{E_3 e_b}{e_a}$$

$$E_1 = \min(e_a, E_{t1})$$

$$E_3 = \min(e_a, E_{t3})$$

$$e_a = E_a + S_b$$

$$e_b = E_b + S_b$$

$$E_{t1} = 130 \pm 10 \text{ MeV}$$

$$E_{t3} = 41 \pm 5 \text{ MeV}$$

(d) Calculations

As we are dealing with high incident and ejectile energies it was reasonable to consider only the MSD process. [11, 25]

We therefore made use of the expression in equation (0.10) to calculate the differential cross section. The slope parameter was calculated by using equation (0.14).

As we considered both α and ${}^3\text{He}$ particles as ejectiles we had to make use of two different expressions to calculate the slope parameter. Two Fortran programs were written to calculate the differential cross sections for the α and ${}^3\text{He}$ particles. The results obtained from the calculations are compared with the experimental data in the next chapter.

CHAPTER FIVE

RESULTS

RESULTS

1. Energy Spectra

The continuum energy spectra in the laboratory frame of reference were obtained for the reactions $^{27}\text{Al}(p, \alpha)$, $^{27}\text{Al}(p, {}^3\text{He})$, $^{59}\text{Co}(p, \alpha)$, $^{59}\text{Co}(p, {}^3\text{He})$, $^{197}\text{Au}(p, \alpha)$, and $^{197}\text{Au}(p, {}^3\text{He})$ at incident energies of 120, 160, and 200 MeV.

(a) α particle emission

The energy spectra for α particle emission are shown in figures 5.1–5.3. Statistical error bars are indicated for cases in which the error exceeds the symbol size.

The spectra vary rapidly with angle in the forward direction and remain constant in shape and magnitude in the backward direction, i.e. for detection angles greater than 80° for all three targets. High energy particles are produced mainly at forward angles for all target nuclei. On the other hand, the low energy particles differ only by a factor two from isotropy in the case of the ^{197}Au target, and are peaked much more strongly in the forward direction for the two lighter nuclei.

In figure 5.4 the energy spectra are displayed for a detection angle of 20° . We observe that the α particle yield increases as the target mass increases for all three incident energies.

(b) ${}^3\text{He}$ particle emission

The energy spectra for ${}^3\text{He}$ particle emission are shown in figures 5.5–5.7. Statistical error bars are shown for cases in which the error is greater than the symbol size used.

The spectra vary rapidly with angle in the forward direction, and remain more constant in both shape and magnitude in the backward direction, for detection angles greater than 80° for all three targets at the various incident energies. High energy particles are produced mainly at forward angles for all target nuclei. As with α particles, the low energy particles are closer to isotropic in the case of the ^{197}Au target, and more peaked in the forward direction for the two lighter target nuclei.

(c) **Comparison of α and ${}^3\text{He}$ particle emission energy spectra**

In figures 5.8–5.10 the energy spectra are displayed at a forward detection angle of 20° for the three targets at the various incident energies. The decrease in the α particle emission spectra is much more rapid than for the ${}^3\text{He}$ particle emission spectra. This suggests that the emission of α and ${}^3\text{He}$ particles could result from two dissimilar processes [30]. From the figures we also observe that the process of α particle emission is the dominant process for emission energies ≤ 60 MeV. For higher emission energies, or equivalently lower excitation energies, we find that the emission of ${}^3\text{He}$ particles become the dominant process. This feature seems to be independent of the incident energy or the target mass.

In nucleon induced nuclear reactions at excitation energies of several tens of MeV, light composite particle emission will occur. Zhang Jing-shang et al [31] characterizes the emission of composite particles in terms of a formation probability. Their main idea is that some nucleons which form the complex particle may come from levels below the Fermi sea. They have found that the pick-up configurations, involving particles and holes, play an important role for emission energies less than 60 MeV. It is in this region that we have a greater probability for the formation of α particles than for ${}^3\text{He}$ particles. For higher energies it is found that the configurations $4p - 0h$, in the case of α particles, and $3p - 0h$, in the case of ${}^3\text{He}$ particles, become dominant.

As the emission energy decreases we find that the excitation energy increases. This would correspond to the formation of a "hot spot" in which the energy gets distributed amongst the nucleons through nucleon-nucleon interactions. If a particular nucleon, or group of nucleons, get enough energy it can be emitted from this "hot spot". Kozłowski et al [32, 33] have shown that the energy spectra and angular distributions of the α and ${}^3\text{He}$ particles emitted in proton induced reactions can be successfully described in terms of a moving hot source model.

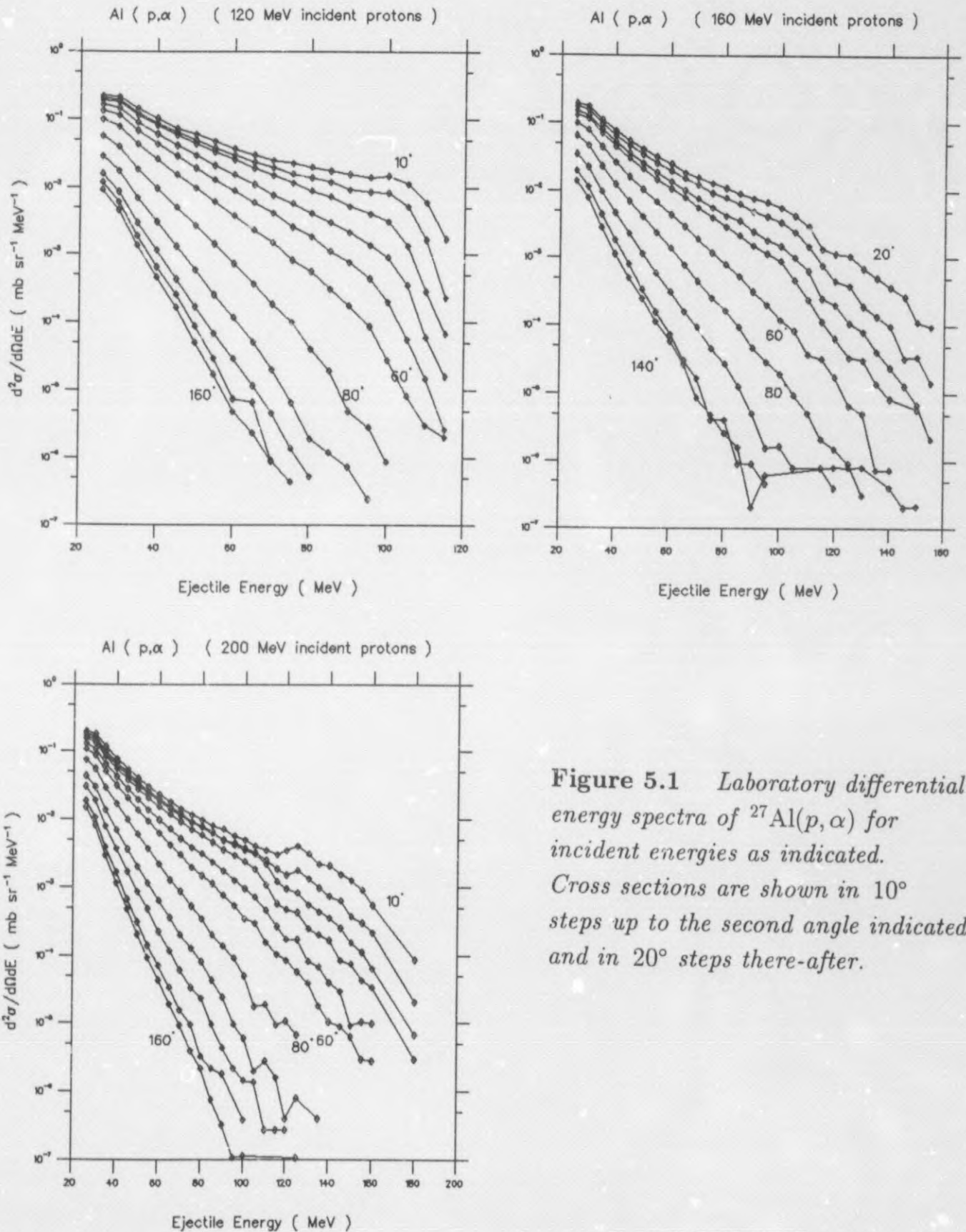


Figure 5.1 *Laboratory differential energy spectra of $^{27}\text{Al}(p, \alpha)$ for incident energies as indicated. Cross sections are shown in 10° steps up to the second angle indicated and in 20° steps there-after.*

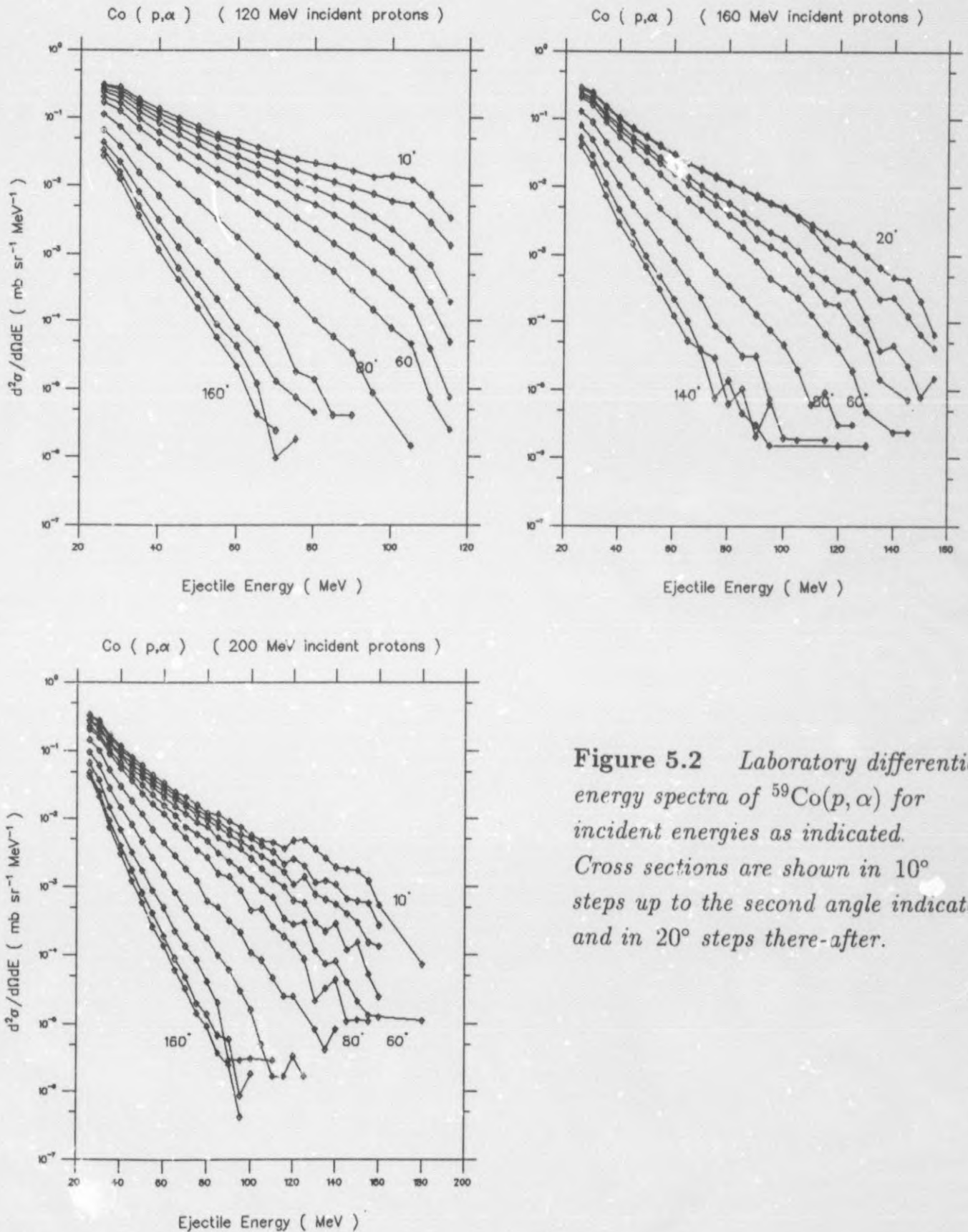


Figure 5.2 Laboratory differential energy spectra of $^{59}\text{Co}(p, \alpha)$ for incident energies as indicated. Cross sections are shown in 10° steps up to the second angle indicated and in 20° steps there-after.

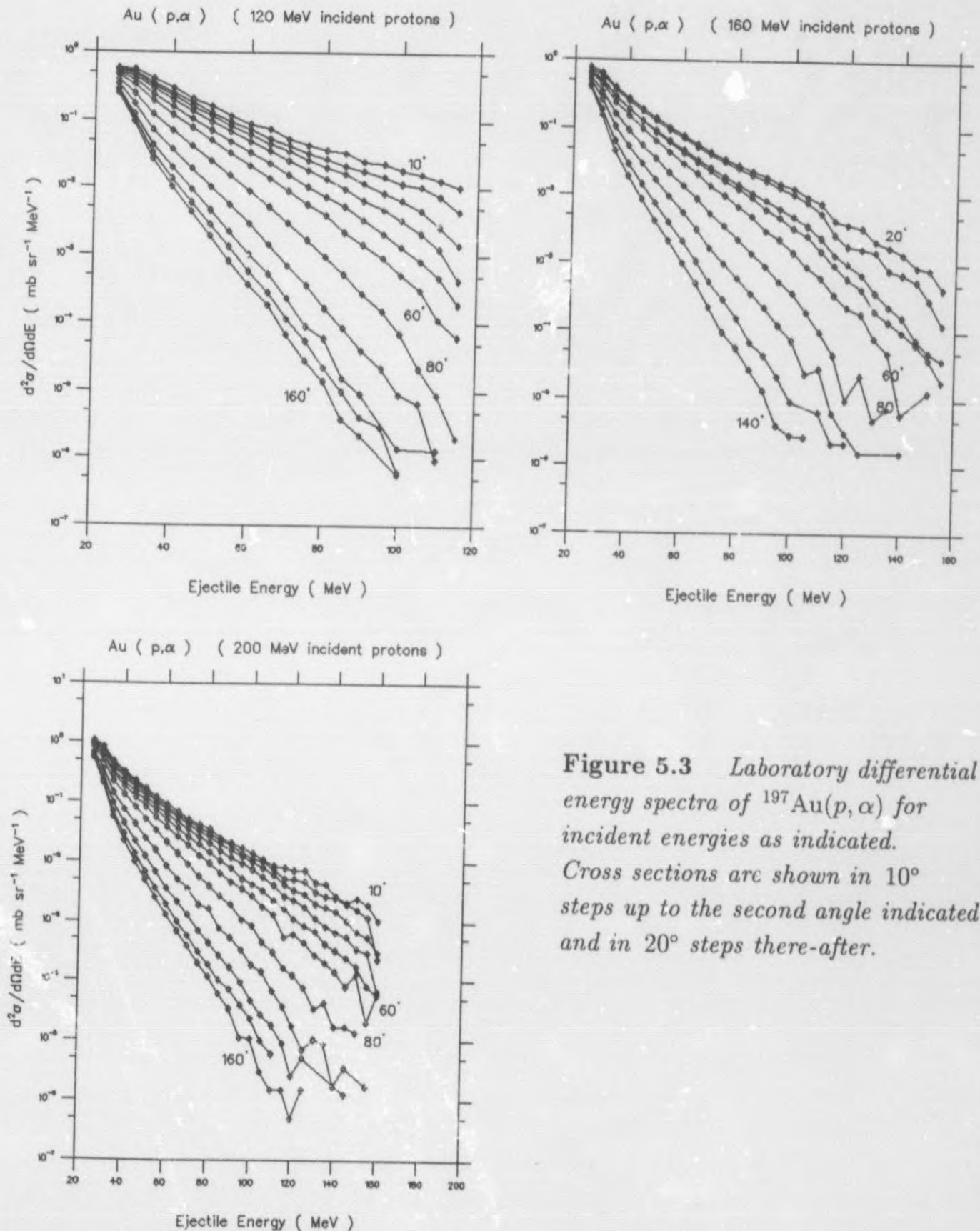


Figure 5.3 Laboratory differential energy spectra of ¹⁹⁷Au(p, α) for incident energies as indicated. Cross sections are shown in 10° steps up to the second angle indicated and in 20° steps there-after.

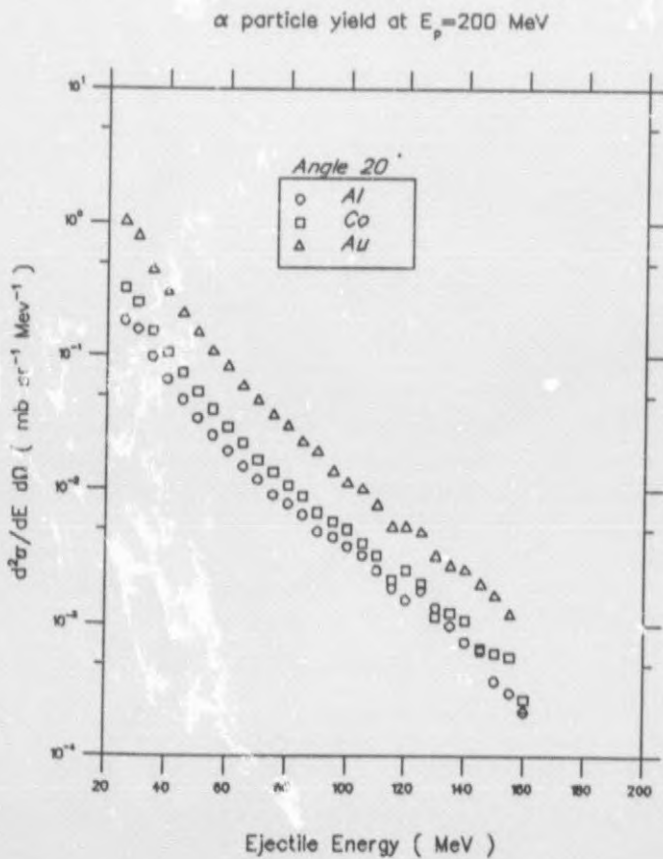
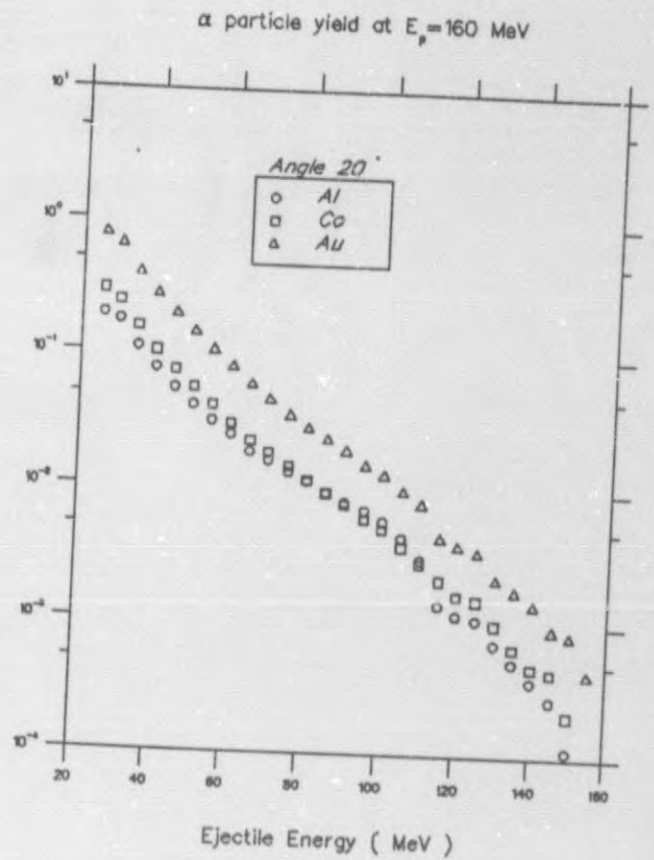
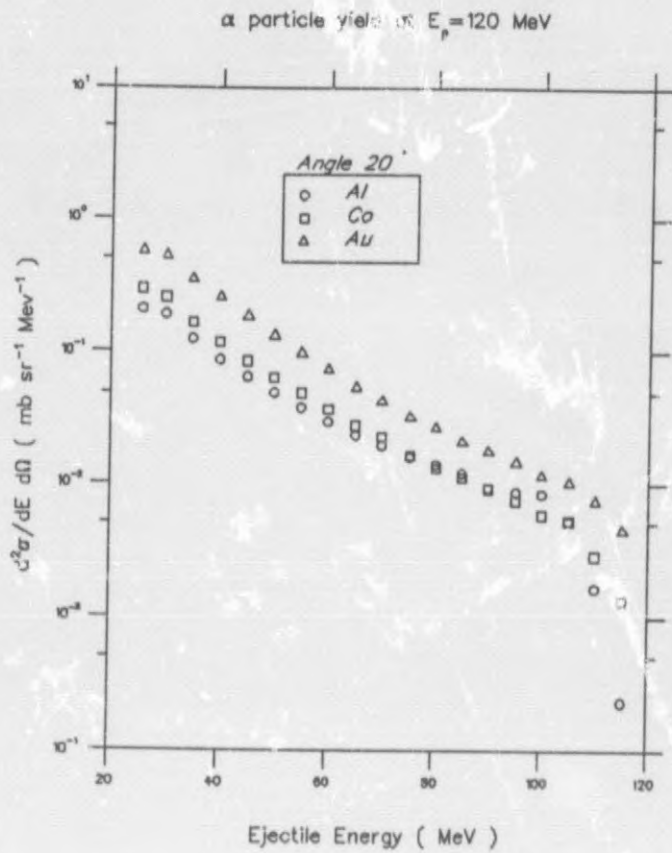


Figure 5.4 Laboratory differential energy spectra displaying the α yield for incident energies as indicated. The spectra are displayed for a detection angle of 20° .

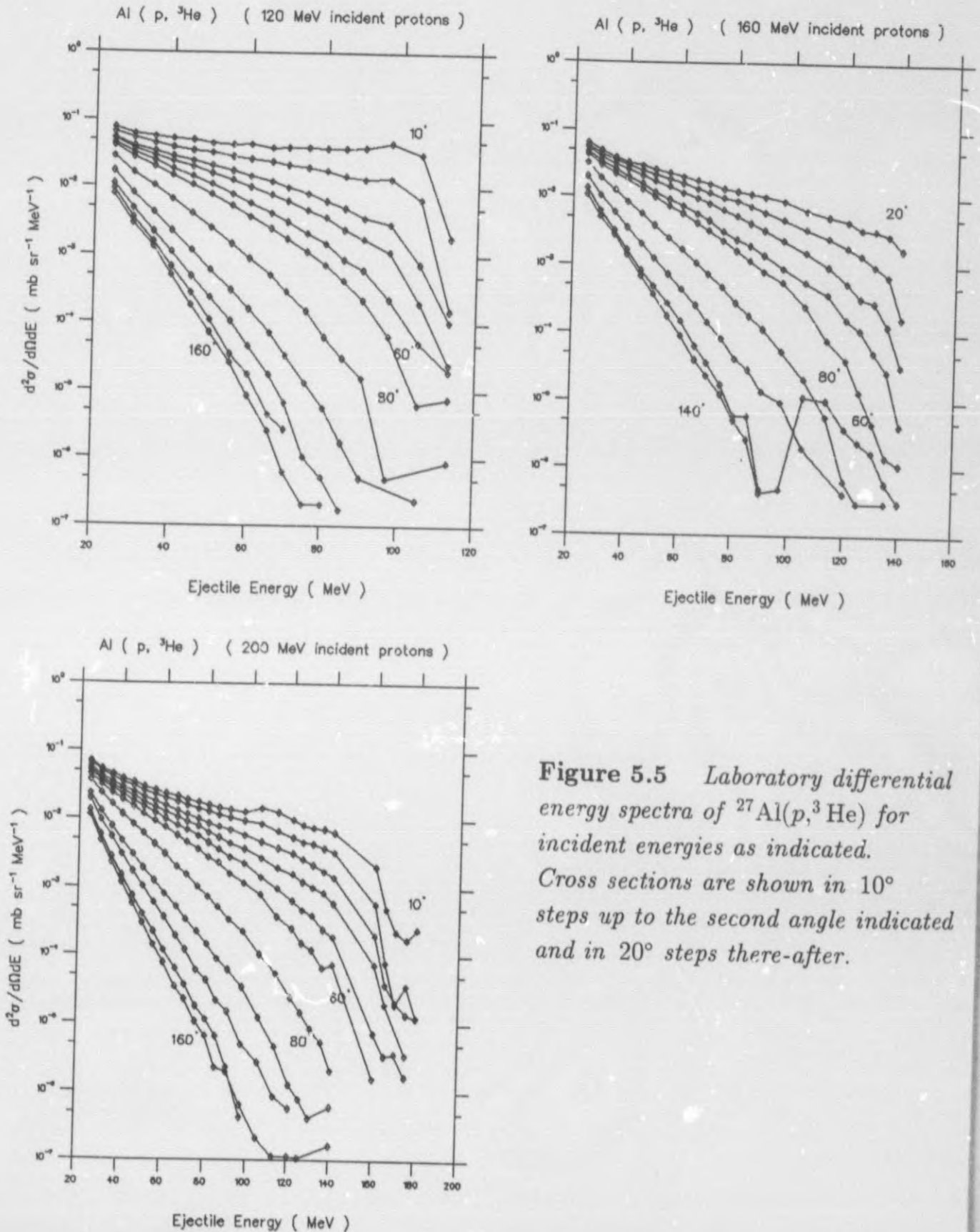


Figure 5.5 Laboratory differential energy spectra of $^{27}\text{Al}(p, {}^3\text{He})$ for incident energies as indicated. Cross sections are shown in 10° steps up to the second angle indicated and in 20° steps there-after.

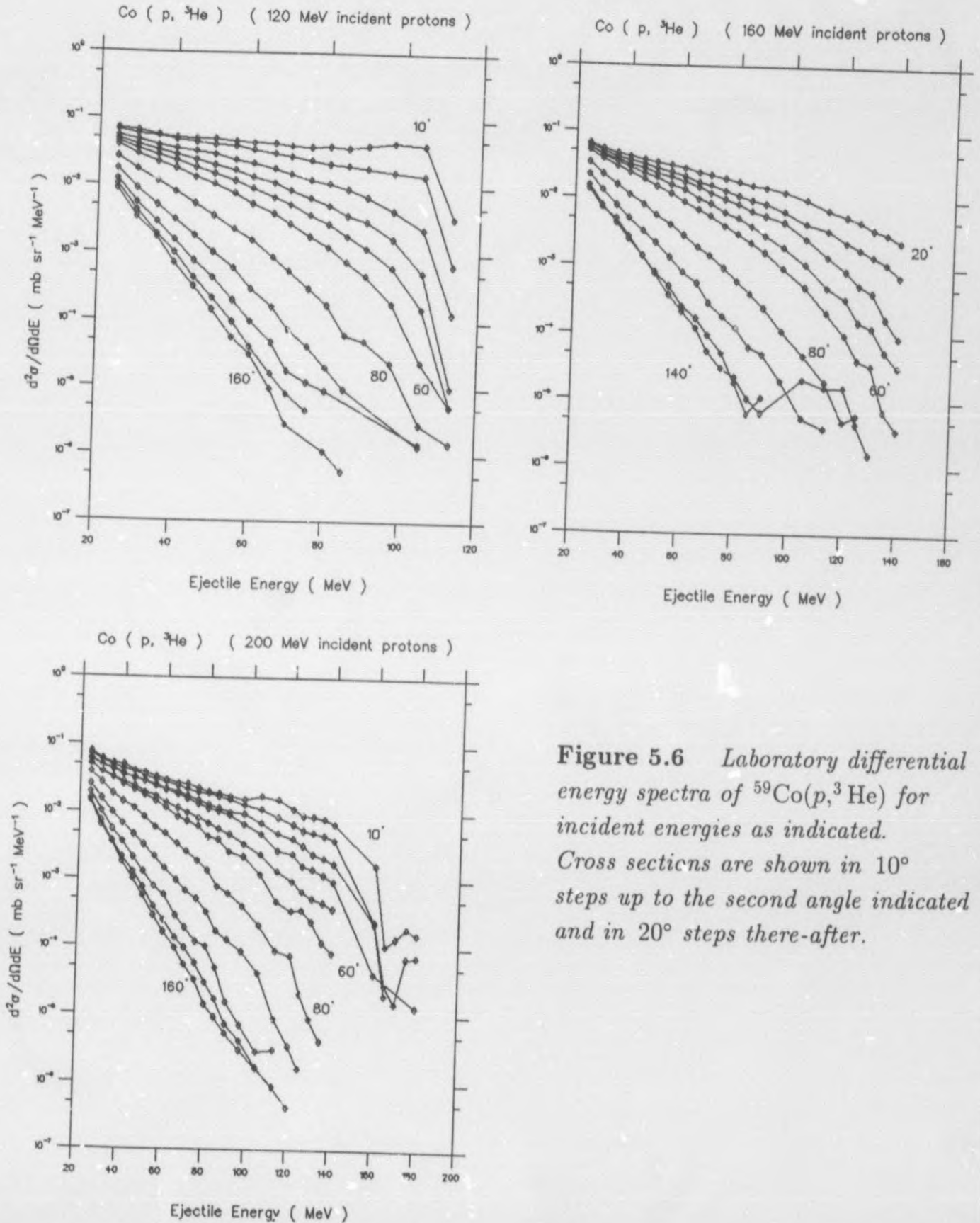


Figure 5.6 Laboratory differential energy spectra of $^{59}\text{Co}(p, ^3\text{He})$ for incident energies as indicated. Cross sections are shown in 10° steps up to the second angle indicated and in 20° steps there-after.

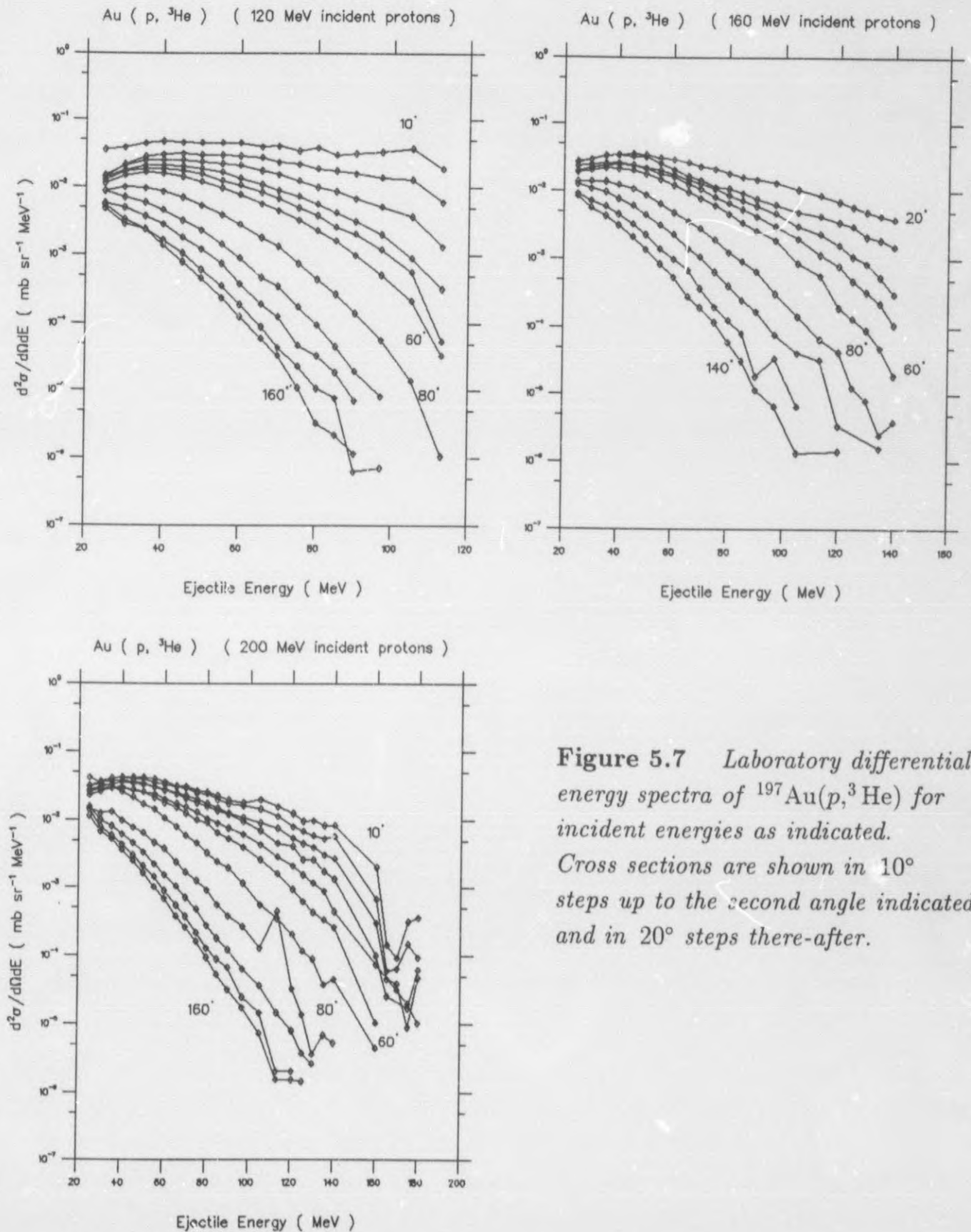


Figure 5.7 Laboratory differential energy spectra of $^{197}\text{Au}(p, {}^3\text{He})$ for incident energies as indicated. Cross sections are shown in 10° steps up to the second angle indicated and in 20° steps there-after.

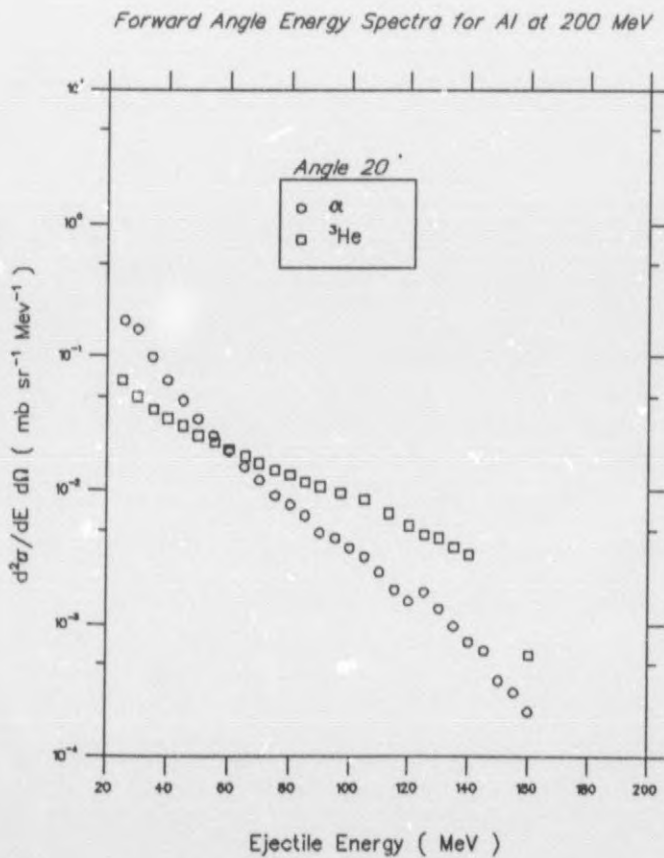
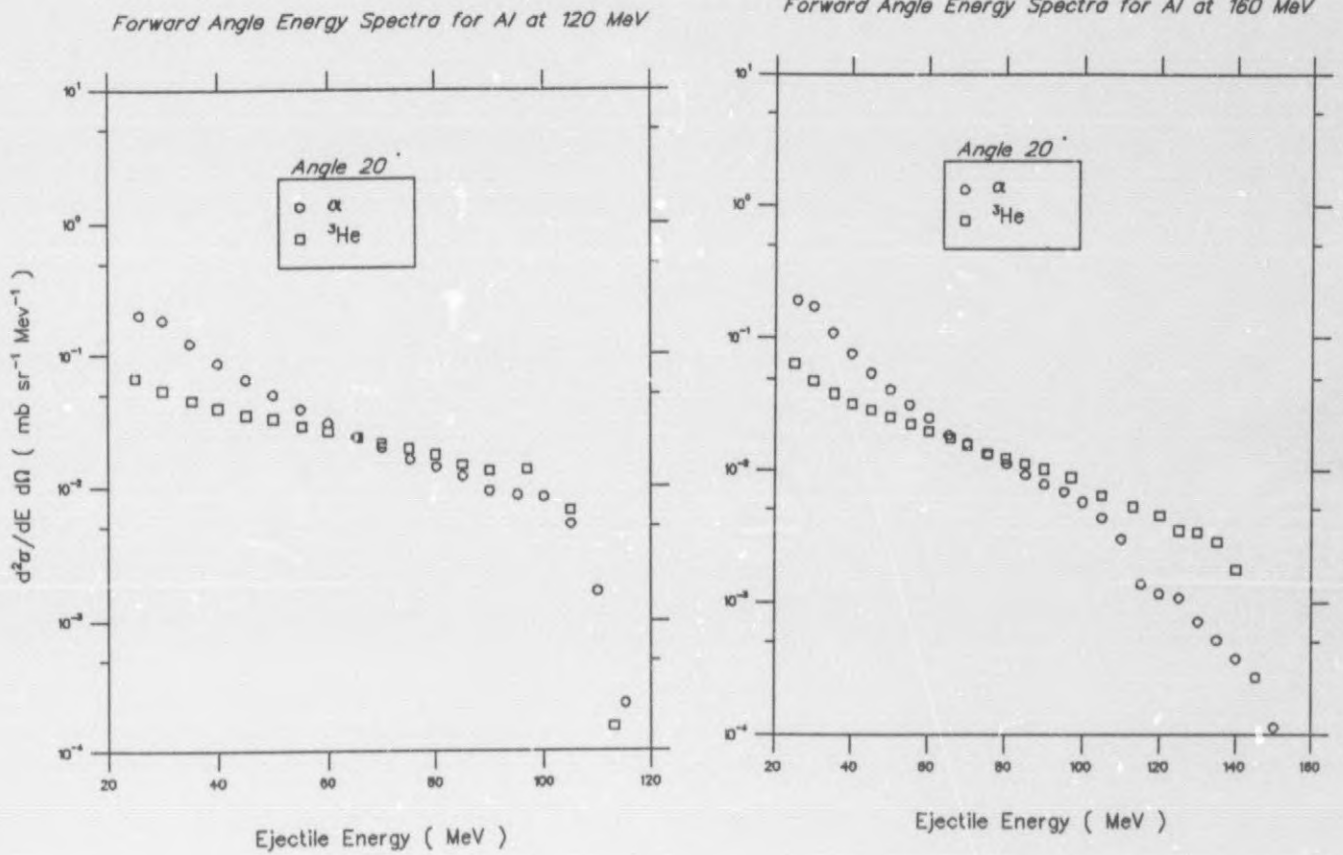
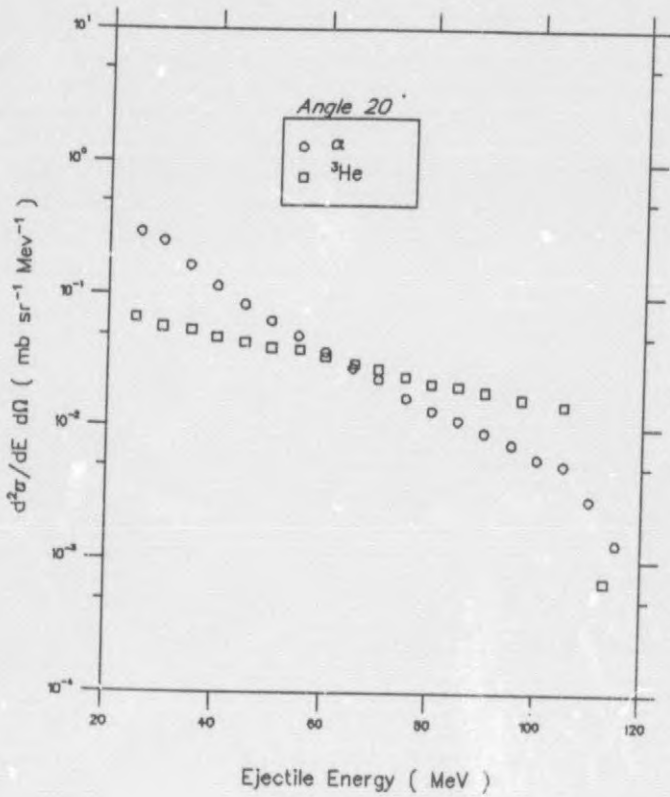
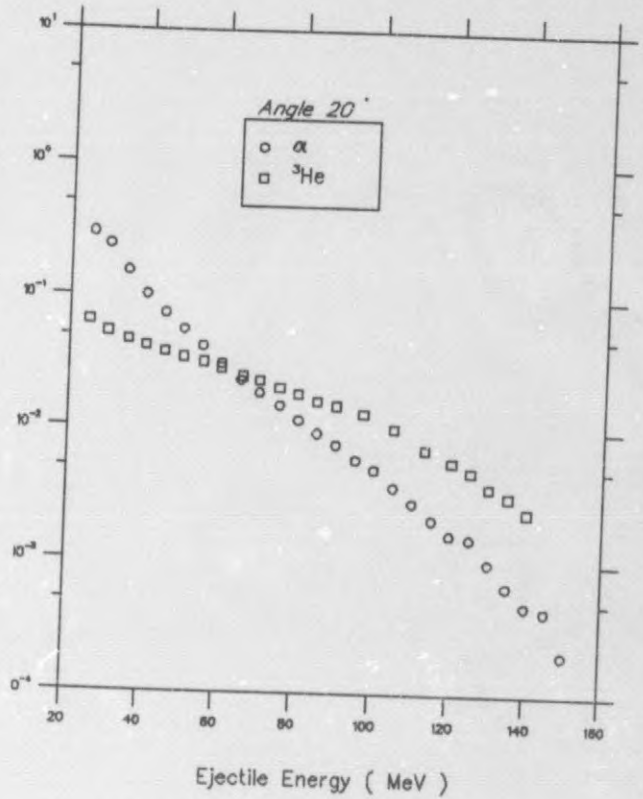


Figure 5.8 Laboratory differential energy spectra of $^{27}\text{Al}(p, X)$, $X=\alpha, ^3\text{He}$ for incident energies as indicated. Spectra are displayed for a detection angle of 20° .

Forward Angle Energy Spectra for Co at 120 MeV



Forward Angle Energy Spectra for Co at 160 MeV



Forward Angle Energy Spectra for Co at 200 MeV

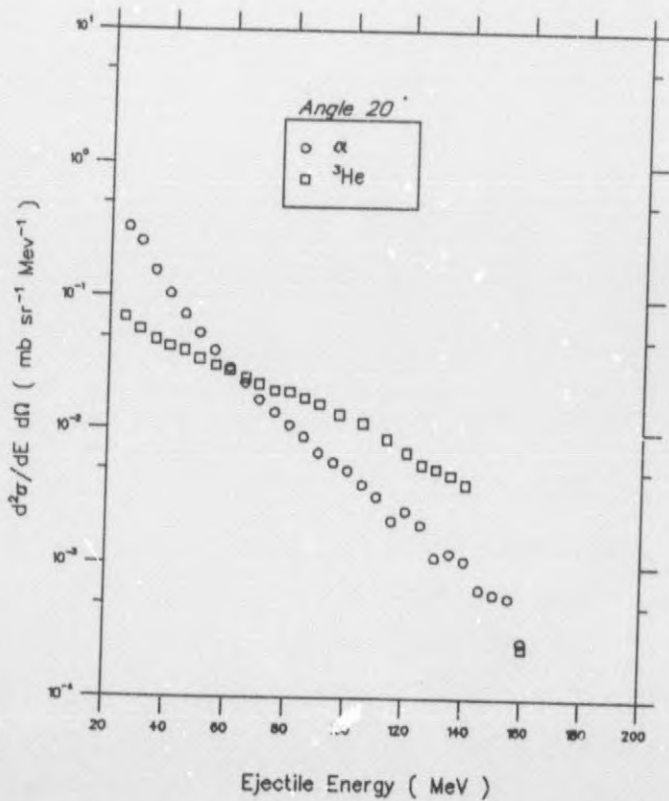


Figure 5.9 Laboratory differential energy spectra of ⁵⁹Co(p, X), X=α, ³He for incident energies as indicated. Spectra are displayed for a detection angle of 20°.

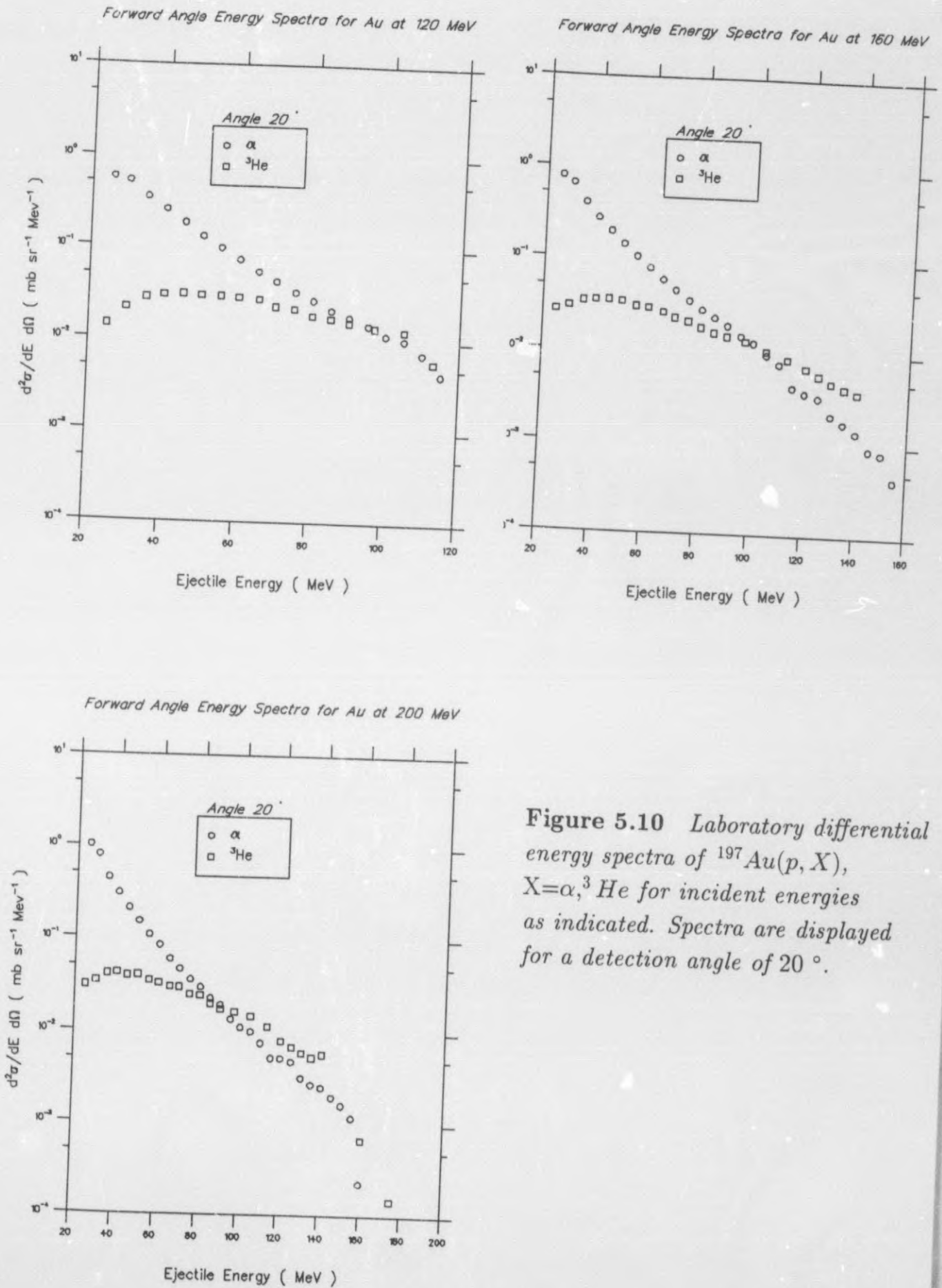


Figure 5.10 Laboratory differential energy spectra of $^{197}\text{Au}(p, X)$, $X=\alpha, {}^3\text{He}$ for incident energies as indicated. Spectra are displayed for a detection angle of 20° .

2. Angular Distributions

The Kalbach phenomenological parametrization was used to calculate the angular distributions for the various reactions in the laboratory frame of reference.

In order for us to be able to compare the calculated angular distributions with the experimental distributions, it was necessary to normalize the theoretical results. The normalization factor corresponds to $\frac{1}{4\pi} \times \frac{d\sigma}{dE}$, as stated in equation (0.10). In order to perform the normalization in a consistent way we decided to normalize the theoretical distributions to the experimental distributions at a detection angle of 80° . To demonstrate that the resultant normalizations appear to be reasonable, the value of $\frac{1}{4\pi} \times \frac{d\sigma}{dE}$ for the complete data set, i.e for both α and ${}^3\text{He}$ particles, is displayed in figures 5.11–5.12 as function of ejectile energy. It is noticeable that the magnitude of the normalization factor is independent of the incident energy and varies smoothly with emission energy. The systematic behavior of the normalization factor is reassuring as it suggests a reliable normalization.

(a) Comparison for (p, α) reactions

The angular distributions for the (p, α) reactions are compared with the Kalbach parametrization in figures 5.13–5.15. In general we find good agreement between the parametrization and the experimental data.

For a fixed ejectile energy we find that the comparison between the parametrization and the experimental data gets better as the target mass increases. This trend is manifested by the quantity in figure 5.16 for the targets and energies shown.

For a fixed target mass we find that the comparison between the parametrization and the experimental data degrades as the incident energy is increased. This behavior is displayed in figure 5.17.

(b) Comparison for $(p, {}^3\text{He})$ reactions

The angular distributions for the $(p, {}^3\text{He})$ reactions are compared with the Kalbach parametrization in figures 5.18–5.20. Overall we again find good agreement between the parametrization and the experimental data.

As in the case of the α particle emission distributions, the $(p, {}^3\text{He})$ reactions display the same target mass and incident energy dependence, as portrayed in figures 5.21–5.22.

3. Comparison of experimental angle-integrated cross sections with Geometry Dependent Hybrid (GDH) model calculations

Angle-integrated cross sections were calculated for the reactions $^{27}\text{Al}(p, \alpha)$, $^{59}\text{Co}(p, \alpha)$, and $^{197}\text{Au}(p, \alpha)$ at incident energies of 120, 160, and 200 MeV. The experimental cross sections were compared with calculations based on the geometry dependent hybrid (GDH) model [22, 23, 24]. These calculations were performed with the computer code ALICE [34].

The GDH model is a semi-classical approach to describe pre-compound decay processes in terms of particle-particle and particle-hole interactions. The cascade of two-body interactions is characterized by an increasing exciton number. The model has been successful in reproducing spectra for the emission of protons and neutrons [24]. However, this model does not contain a mechanism which describes the pre-equilibrium emission of composite particles and hence only predicts the evaporation component of the (p, α) reaction. The comparison between the experimental angle-integrated cross section and the theoretically calculated cross section provides a quantitative estimate of the evaporation component contained in the spectrum.

Figure 5.23 displays the comparison between theoretical calculations and experimental cross sections for the reaction $^{59}\text{Co}(p, \alpha)$ at the incident energies indicated. From the figure it can be seen that the evaporation process contributes only $\simeq 10\%$ to the pre-equilibrium spectrum at an emission energy of $\simeq 40$ MeV. For emission energies greater than 40 MeV we find that the contribution of the evaporation process becomes negligible compared to the pre-equilibrium process. The angle-integrated cross section for the ^{27}Al and ^{197}Au targets, which are not shown, exhibit a similar trend.

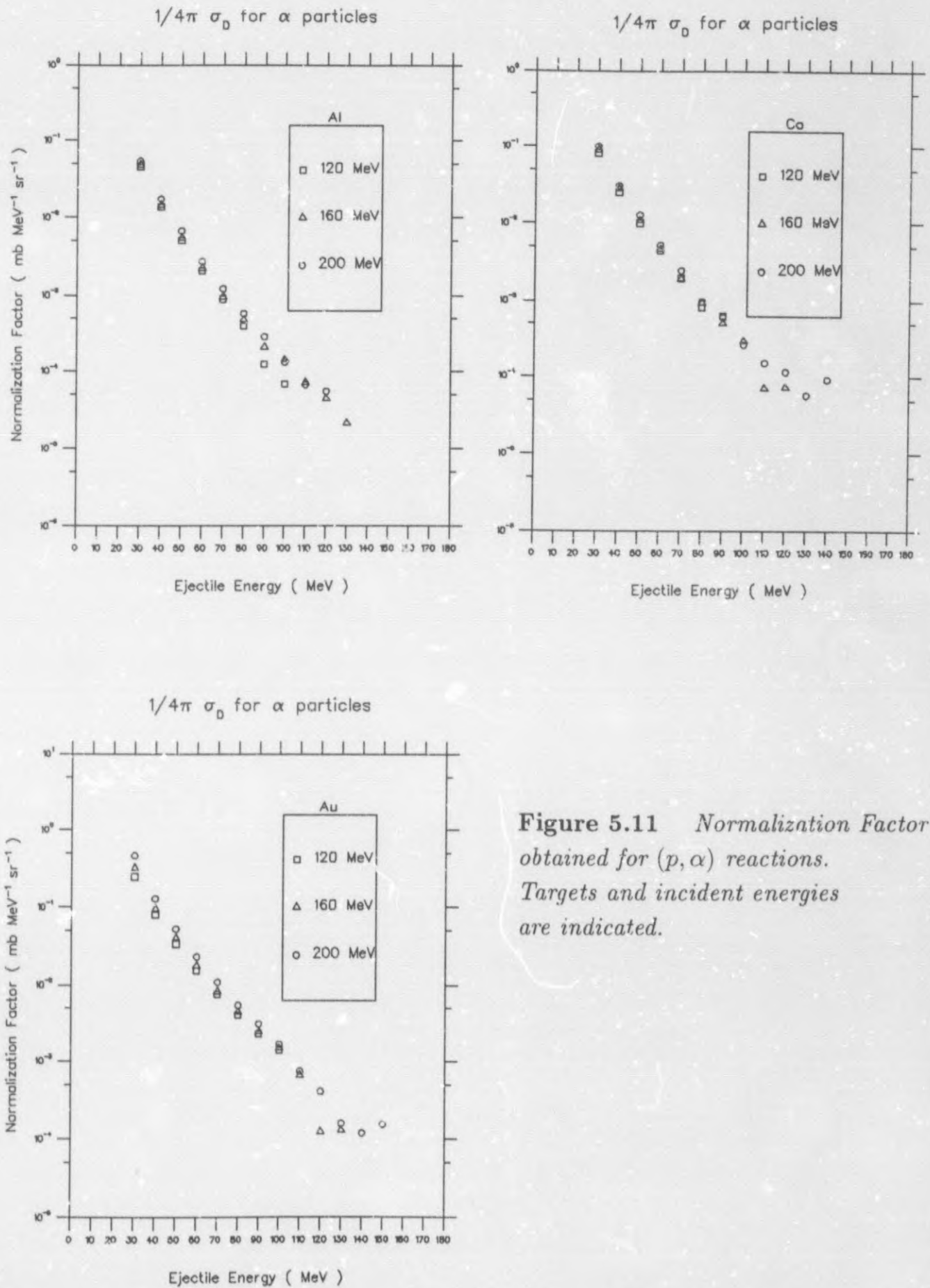


Figure 5.11 Normalization Factor obtained for (p, α) reactions. Targets and incident energies are indicated.

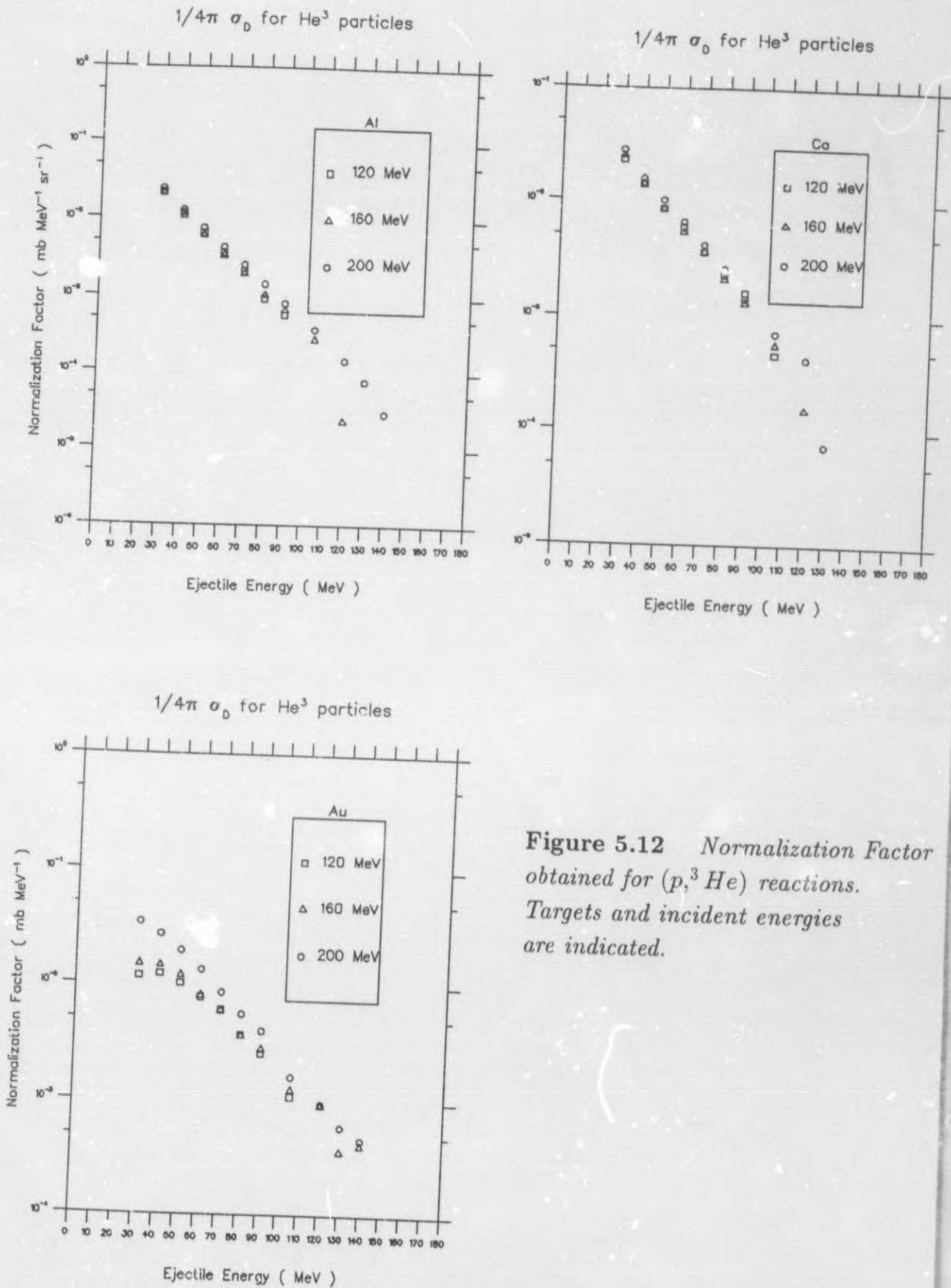


Figure 5.12 Normalization Factor obtained for $(p, ^3\text{He})$ reactions. Targets and incident energies are indicated.

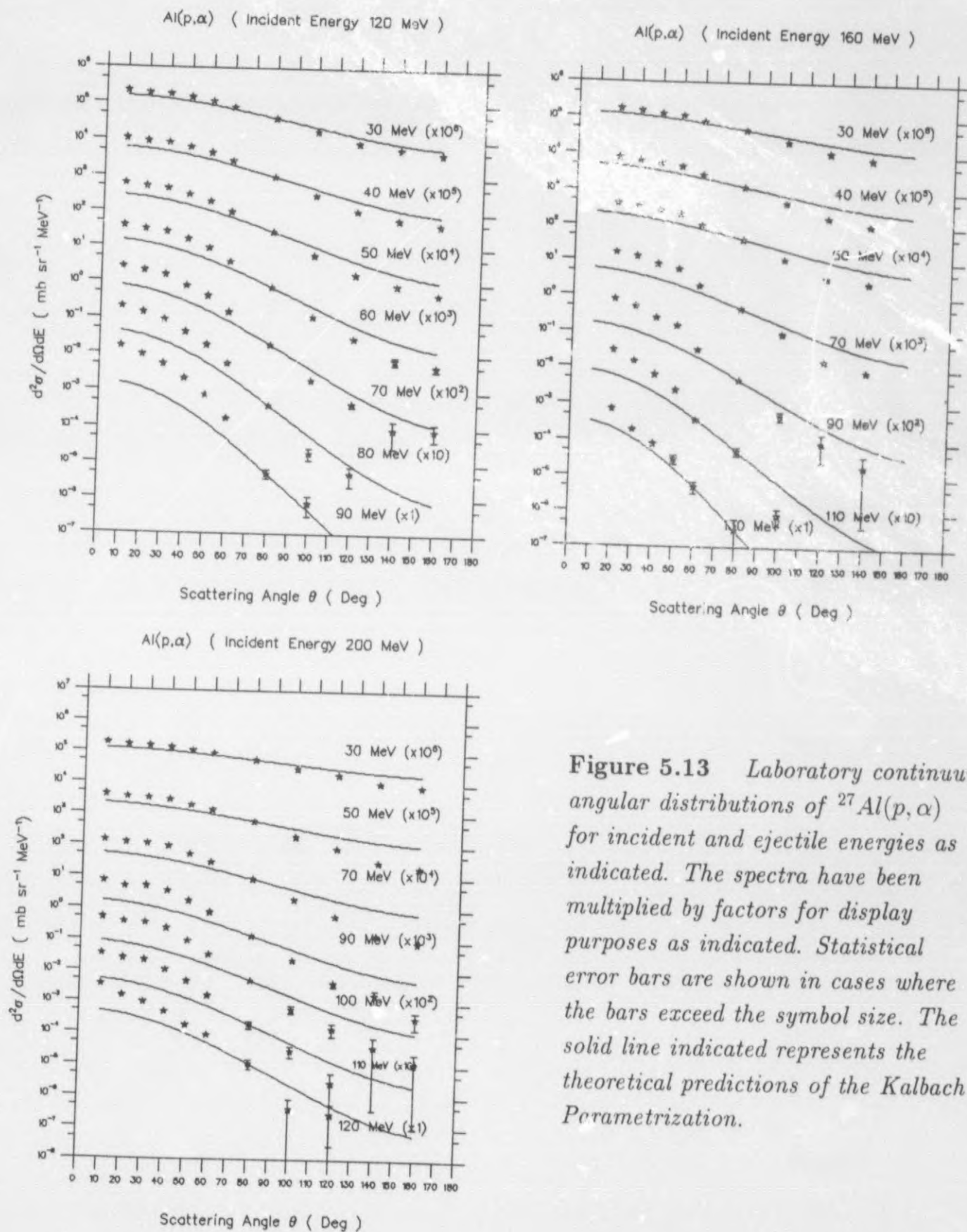


Figure 5.13 Laboratory continuum angular distributions of $^{27}Al(p,\alpha)$ for incident and ejectile energies as indicated. The spectra have been multiplied by factors for display purposes as indicated. Statistical error bars are shown in cases where the bars exceed the symbol size. The solid line indicated represents the theoretical predictions of the Kalbach Parametrization.

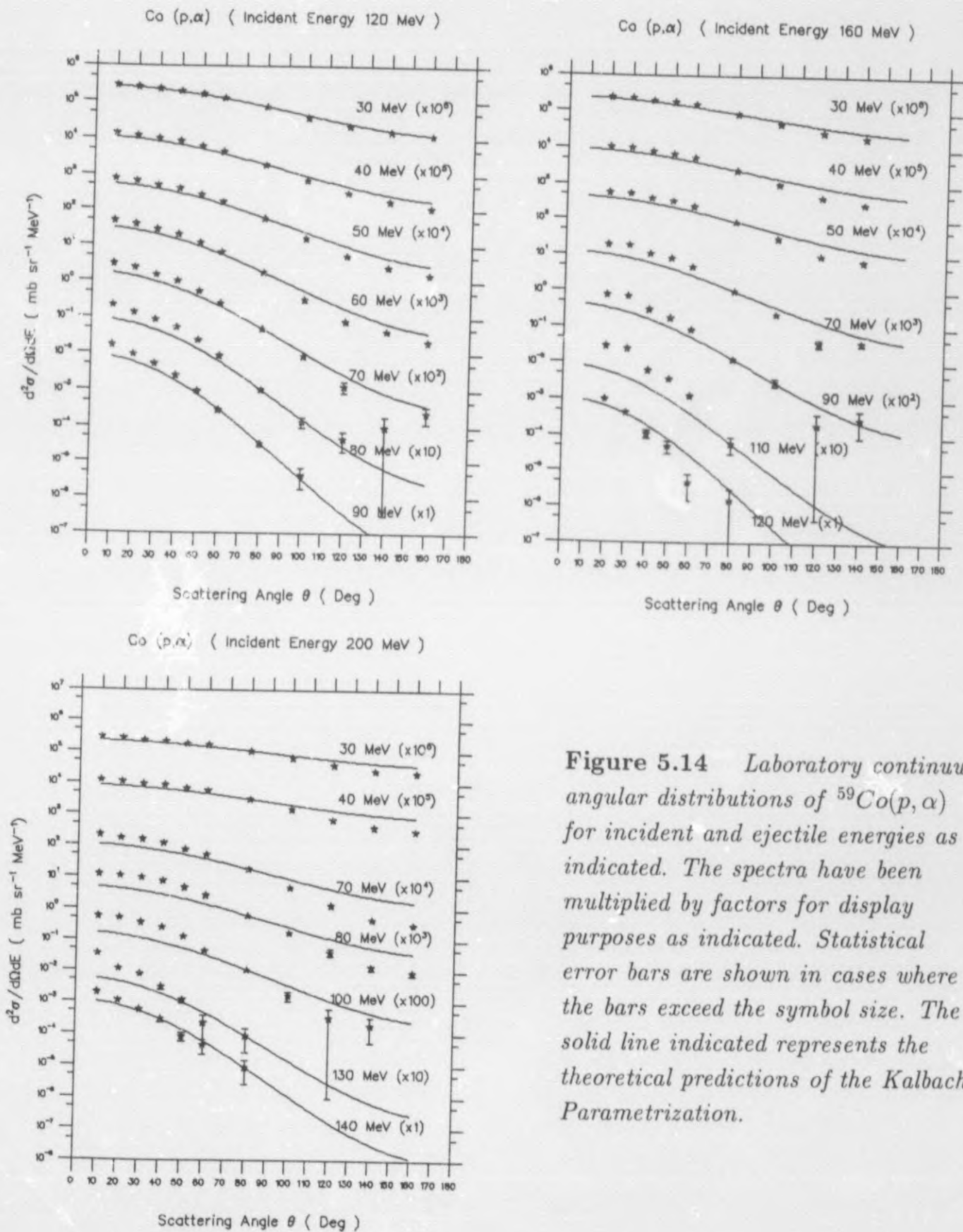


Figure 5.14 Laboratory continuum angular distributions of $^{59}\text{Co}(p, \alpha)$ for incident and ejectile energies as indicated. The spectra have been multiplied by factors for display purposes as indicated. Statistical error bars are shown in cases where the bars exceed the symbol size. The solid line indicated represents the theoretical predictions of the Kalbach Parametrization.

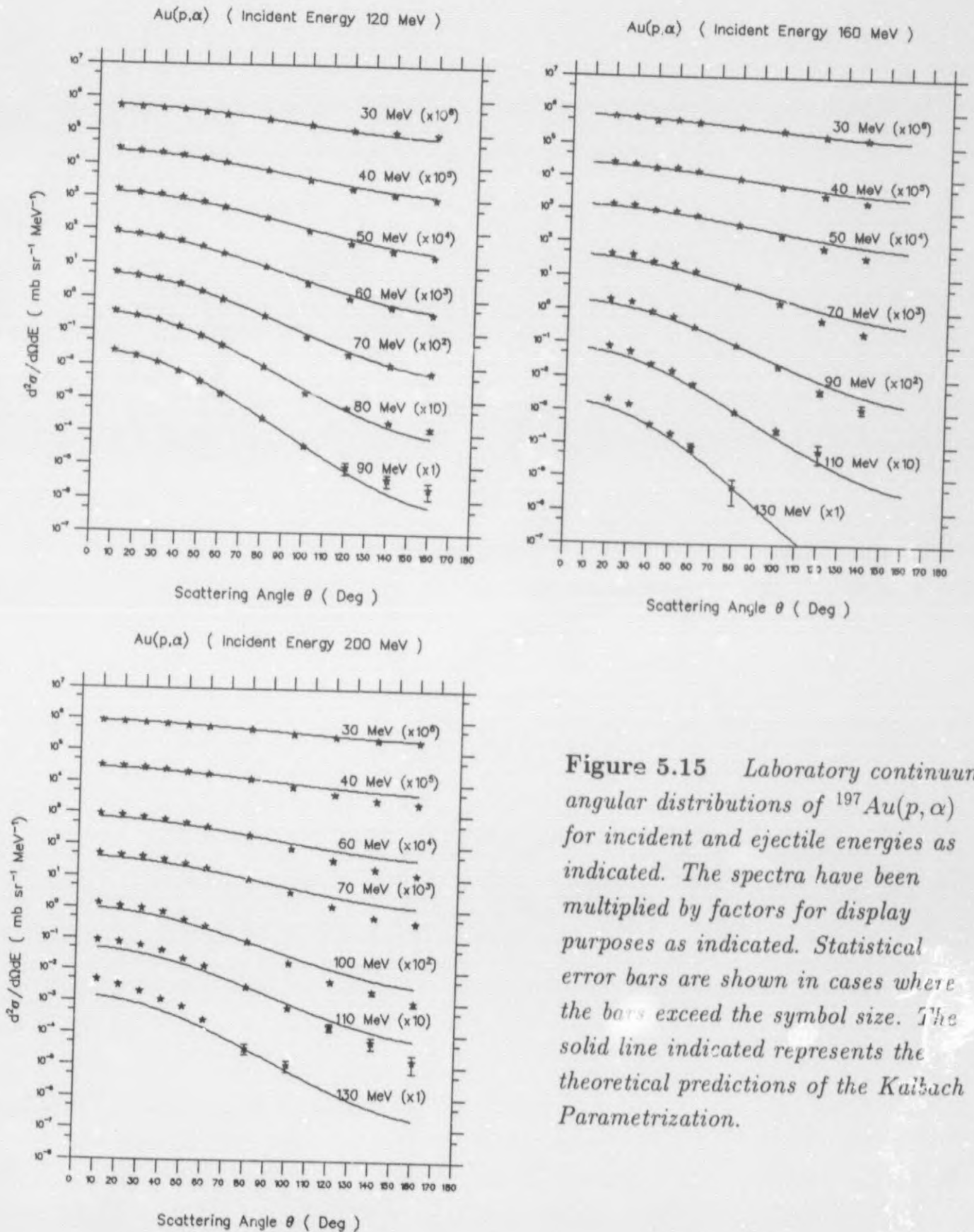


Figure 5.15 Laboratory continuum angular distributions of $^{197}\text{Au}(p,\alpha)$ for incident and ejectile energies as indicated. The spectra have been multiplied by factors for display purposes as indicated. Statistical error bars are shown in cases where the bars exceed the symbol size. The solid line indicated represents the theoretical predictions of the Kubiach Parametrization.

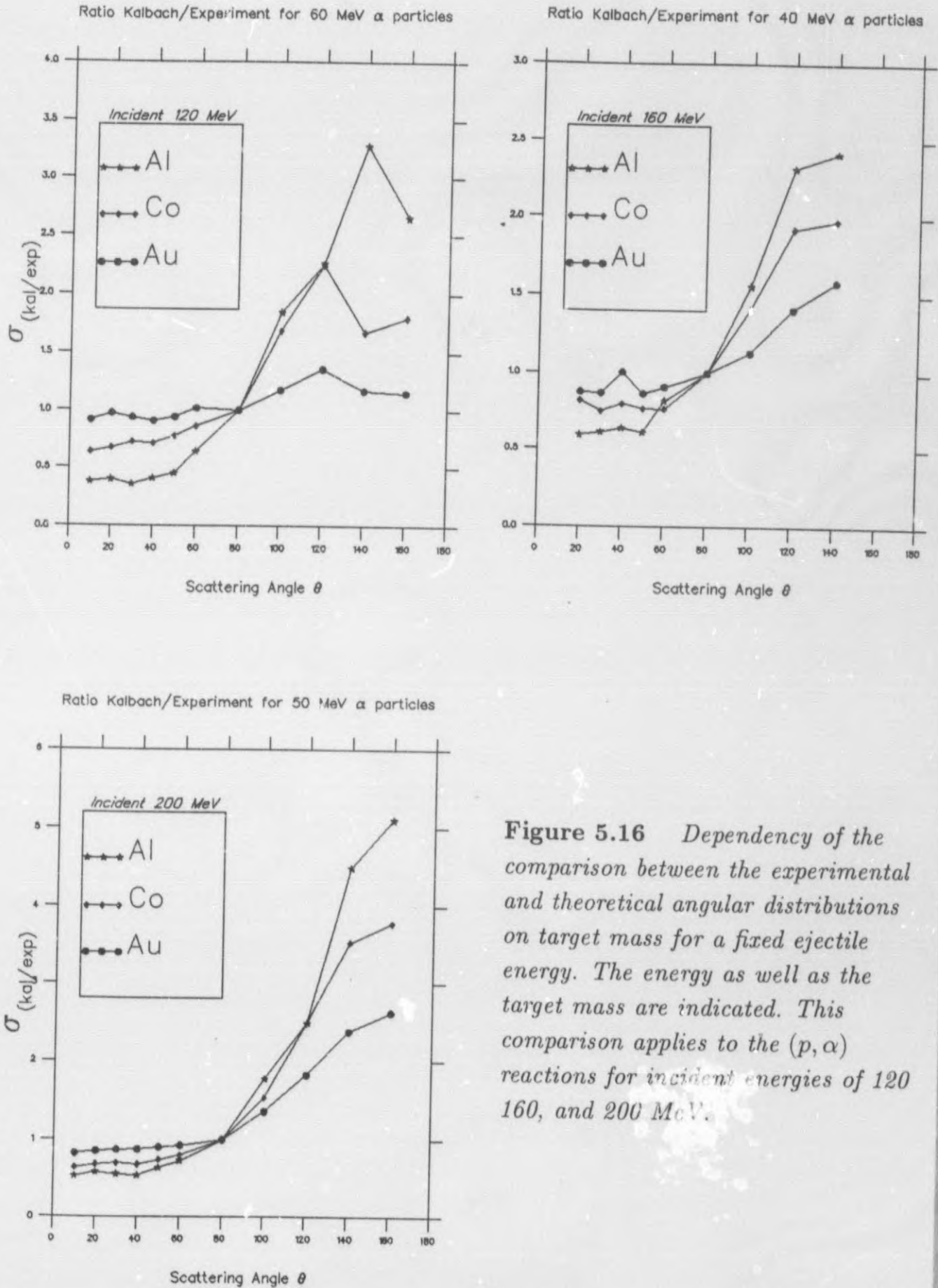


Figure 5.16 Dependency of the comparison between the experimental and theoretical angular distributions on target mass for a fixed ejectile energy. The energy as well as the target mass are indicated. This comparison applies to the (p, α) reactions for incident energies of 120, 160, and 200 MeV.

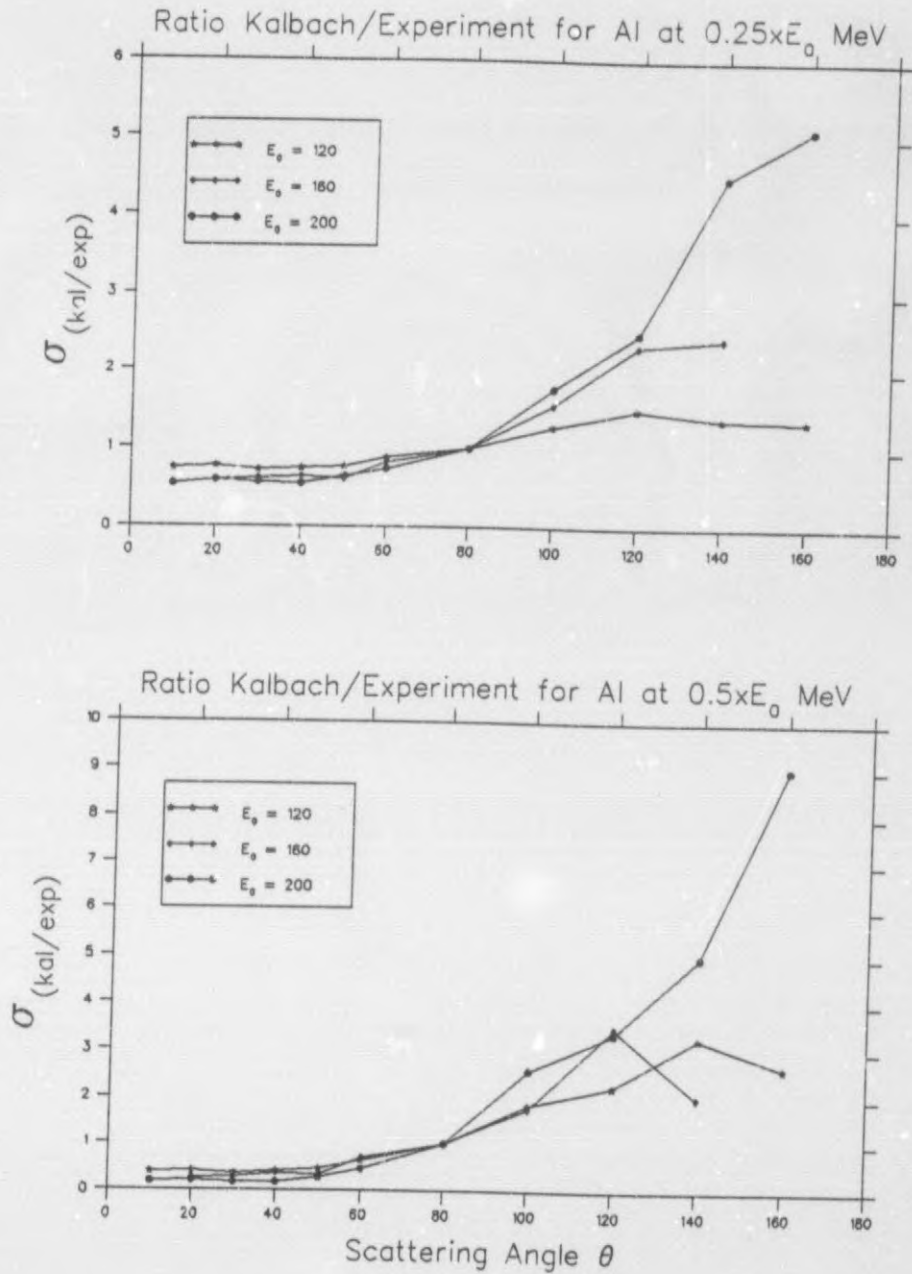


Figure 5.17 Dependency of comparison between the experimental and theoretical angular distributions on incident energy for fixed fractions of the incident energy. Target and fractions are indicated. Comparison applies to the (p, α) reactions.

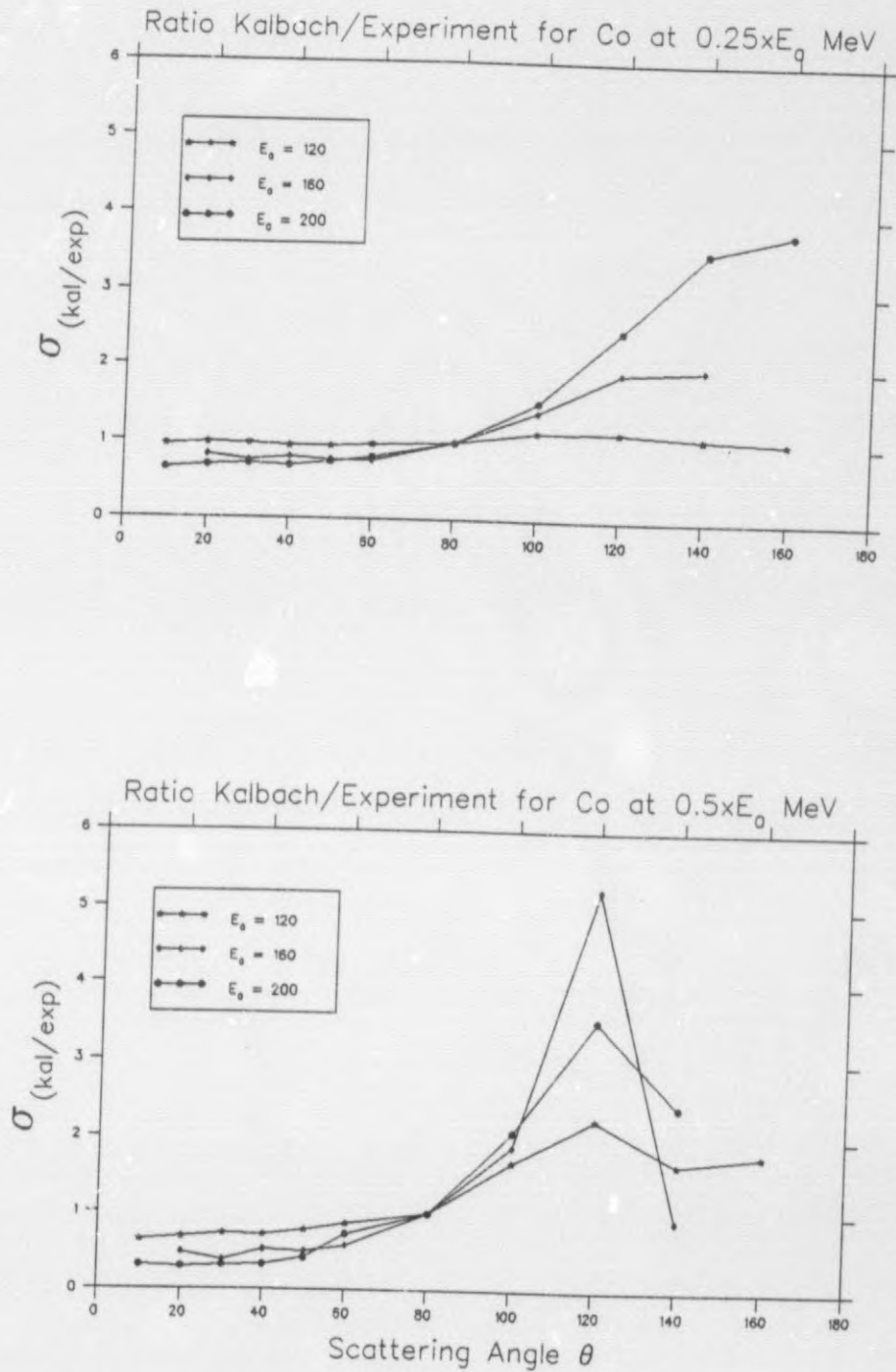
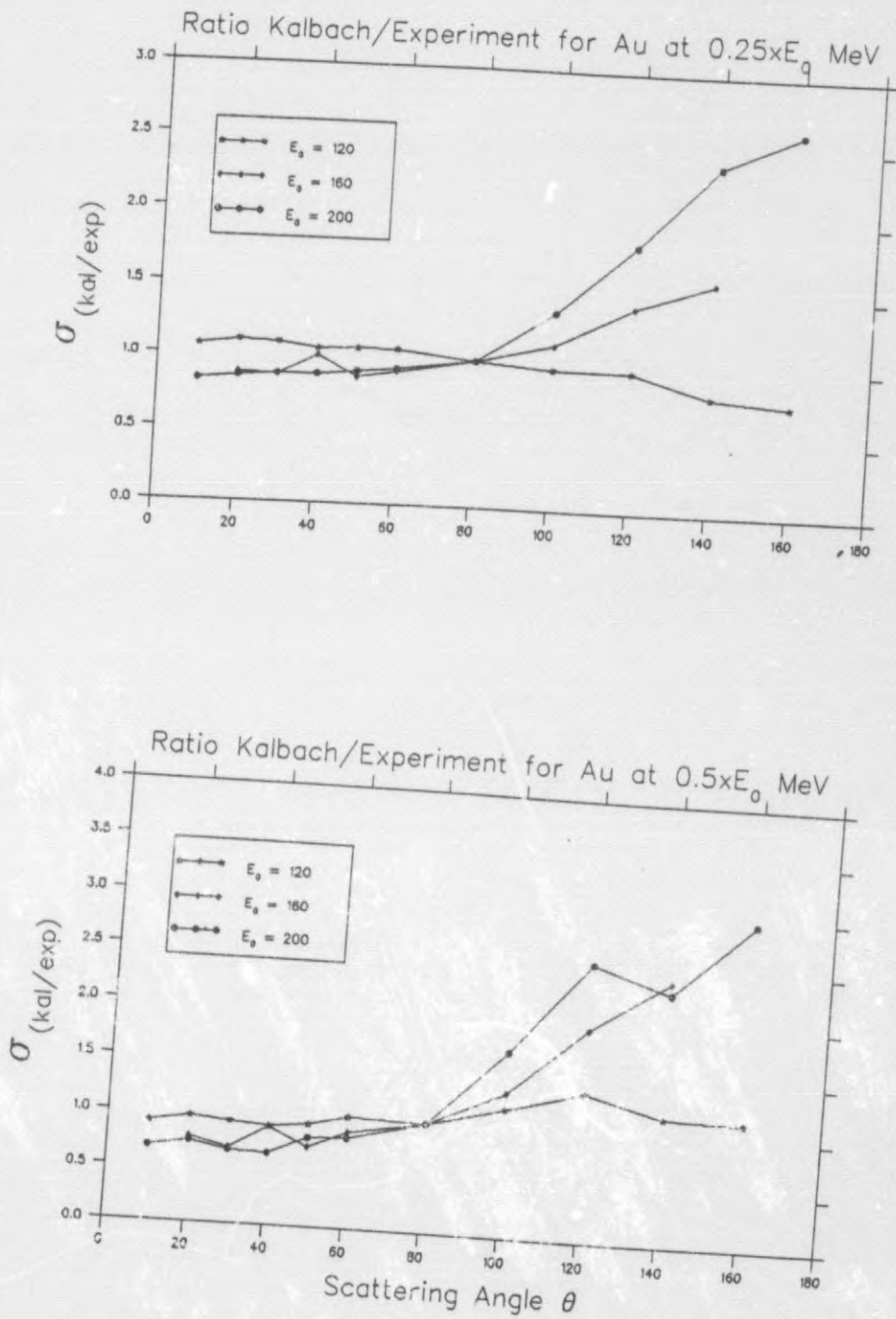


Figure 5.17 *Continues*

Figure 5.17 *Continues*

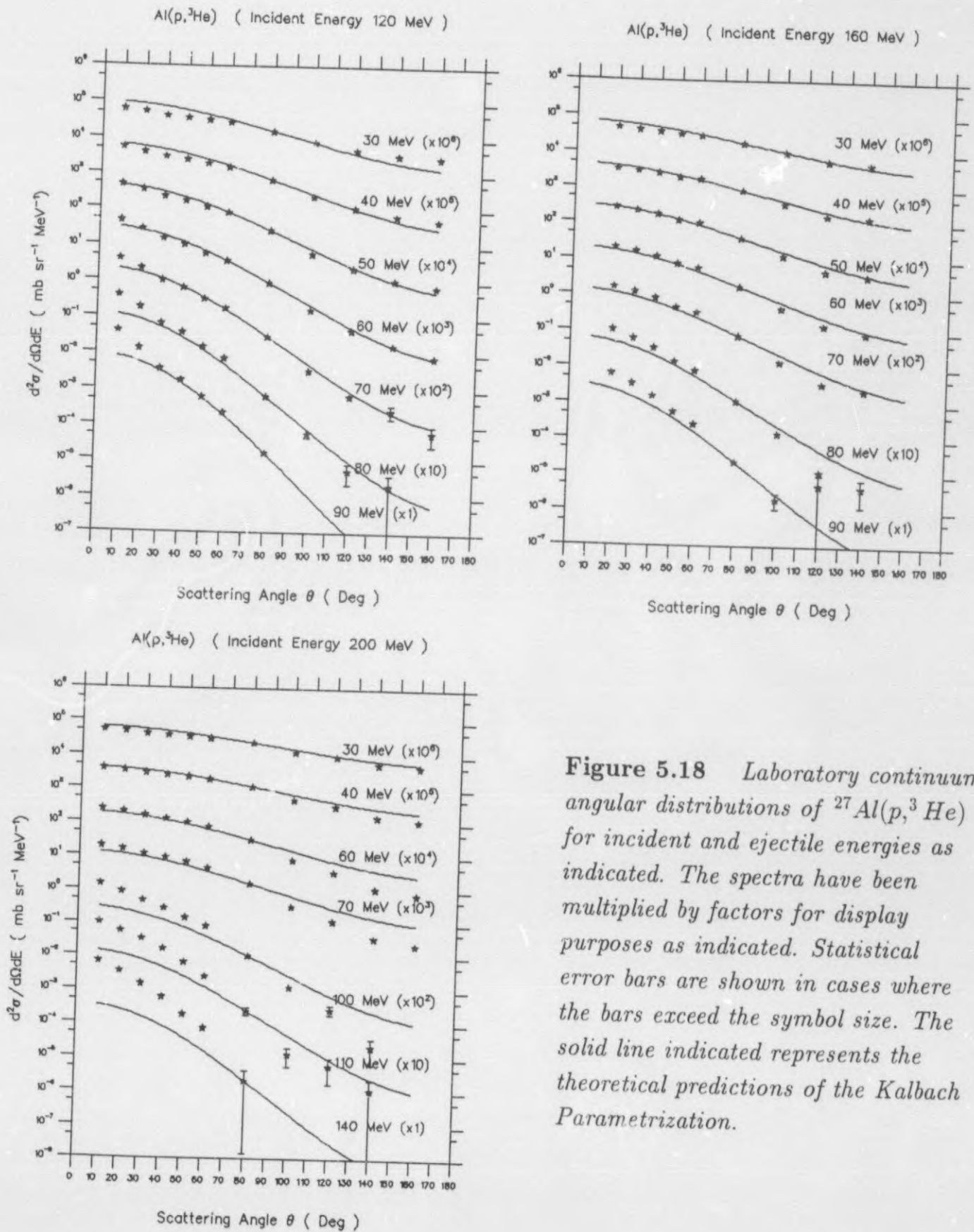


Figure 5.18 Laboratory continuum angular distributions of $^{27}\text{Al}(p,^3\text{He})$ for incident and ejectile energies as indicated. The spectra have been multiplied by factors for display purposes as indicated. Statistical error bars are shown in cases where the bars exceed the symbol size. The solid line indicated represents the theoretical predictions of the Kalbach Parametrization.

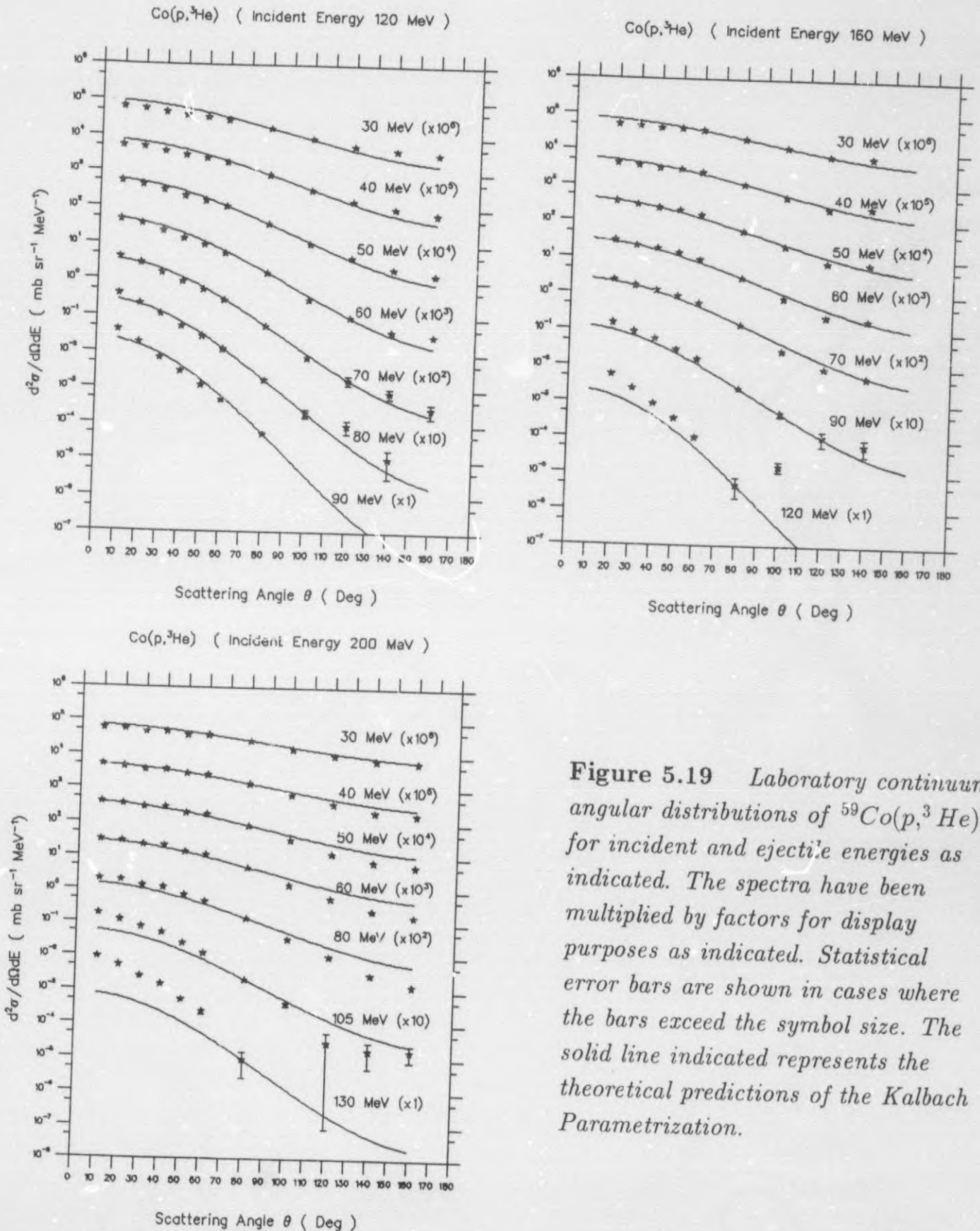


Figure 5.19 Laboratory continuum angular distributions of $^{59}\text{Co}(p,^3\text{He})$ for incident and ejectile energies as indicated. The spectra have been multiplied by factors for display purposes as indicated. Statistical error bars are shown in cases where the bars exceed the symbol size. The solid line indicated represents the theoretical predictions of the Kalbach Parametrization.

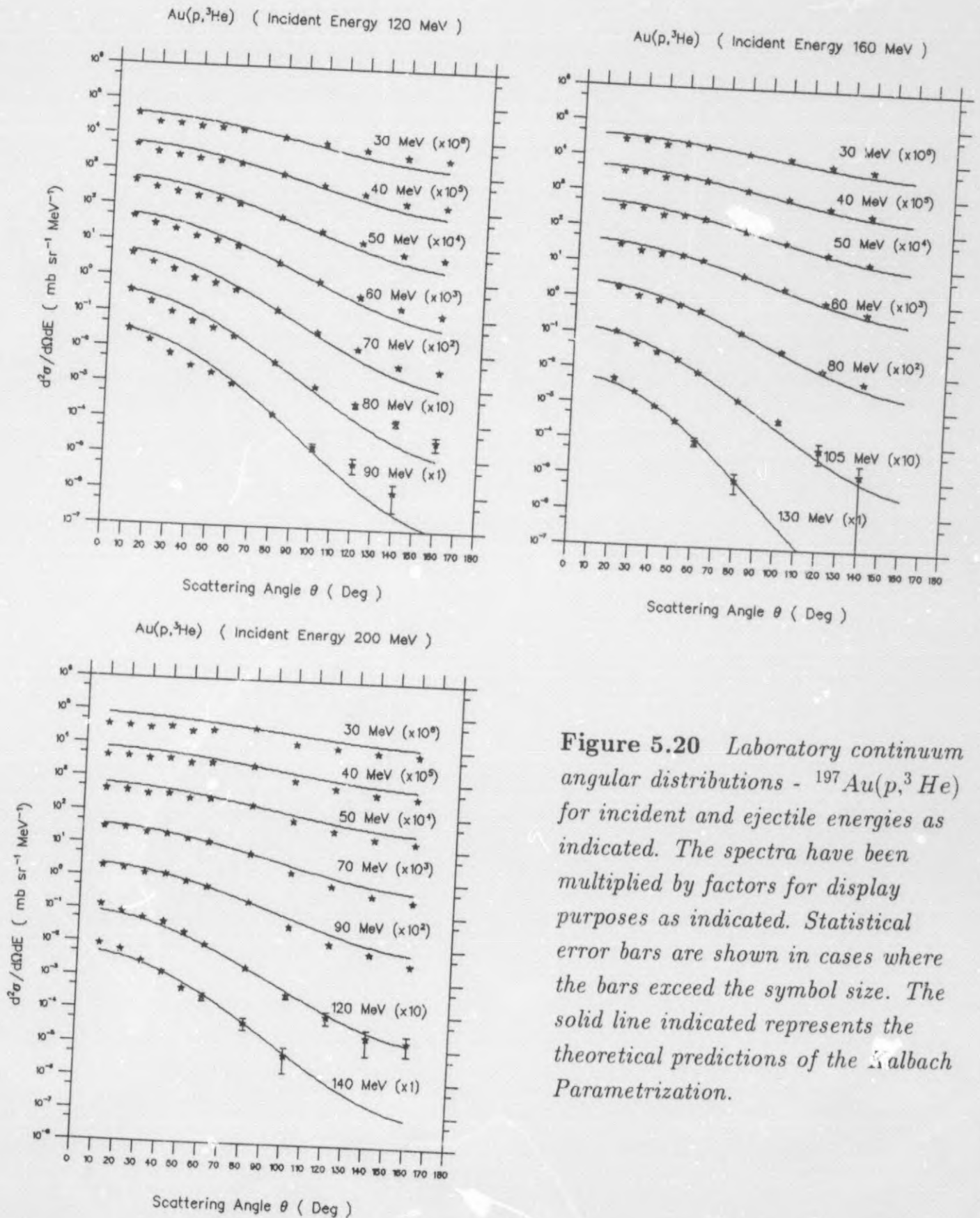


Figure 5.20 Laboratory continuum angular distributions - ${}^{197}Au(p, {}^3He)$ for incident and ejectile energies as indicated. The spectra have been multiplied by factors for display purposes as indicated. Statistical error bars are shown in cases where the bars exceed the symbol size. The solid line indicated represents the theoretical predictions of the Kalbach Parametrization.

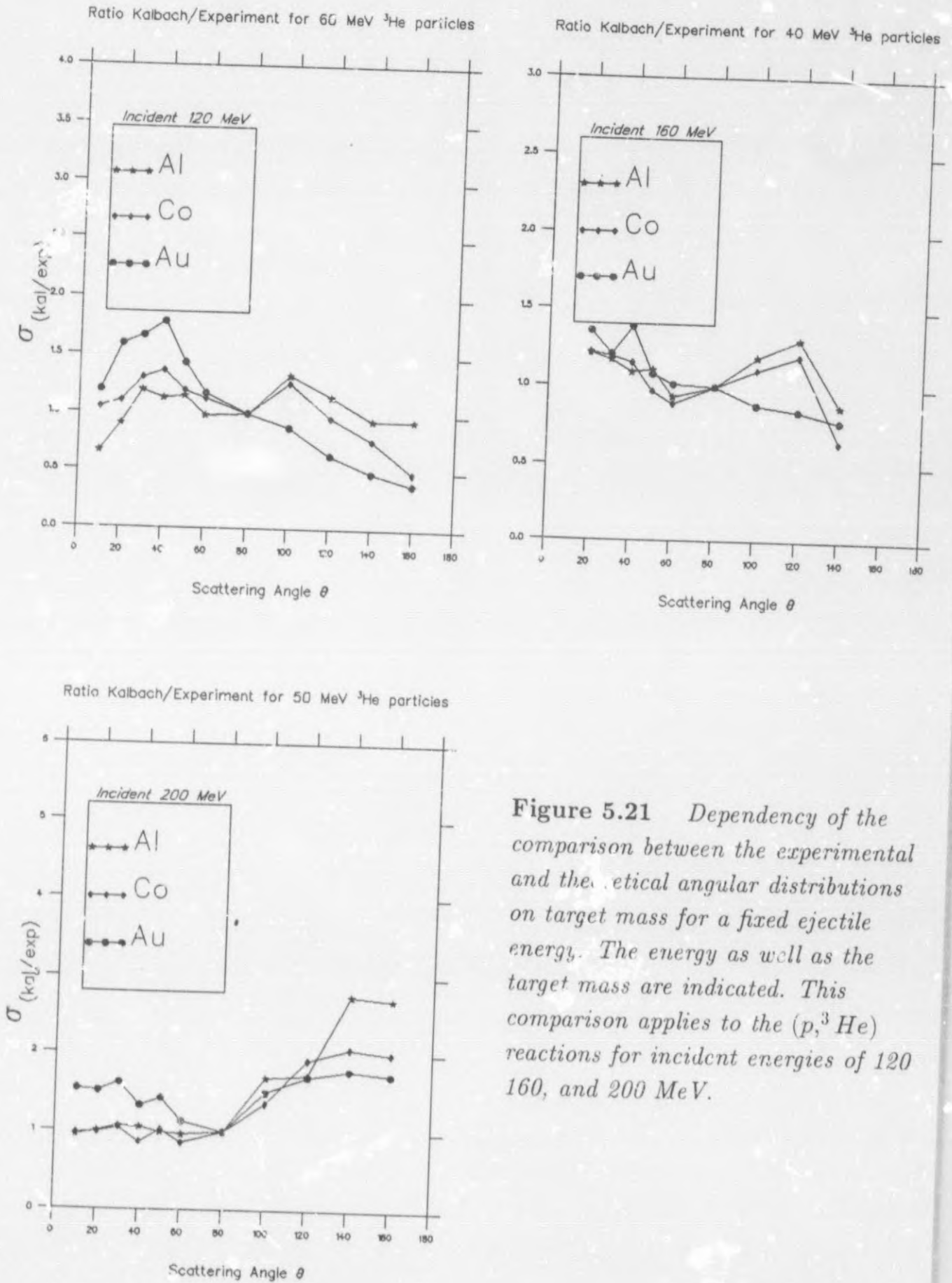


Figure 5.21 Dependency of the comparison between the experimental and the theoretical angular distributions on target mass for a fixed ejectile energy. The energy as well as the target mass are indicated. This comparison applies to the $(p, {}^3\text{He})$ reactions for incident energies of 120, 160, and 200 MeV.

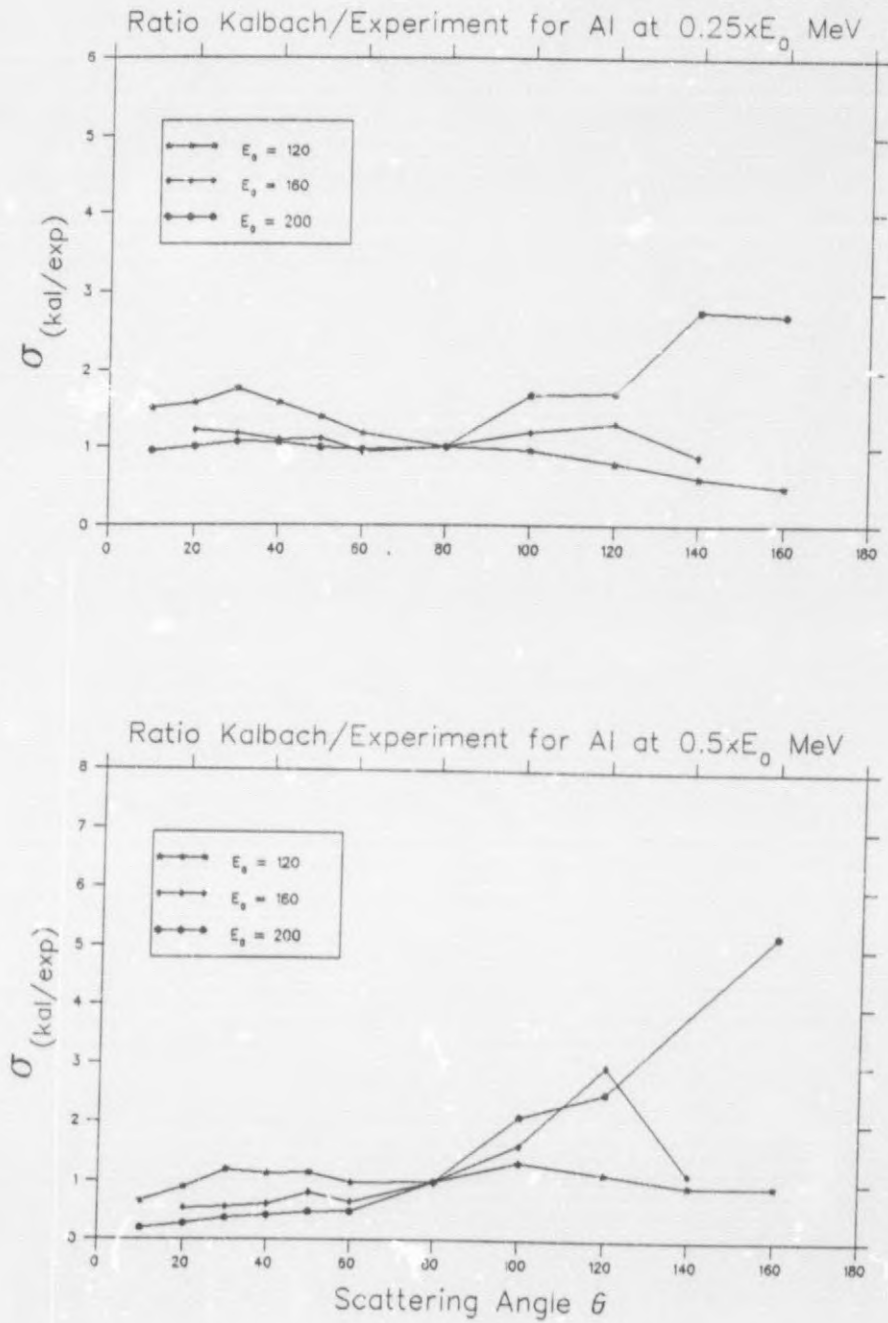


Figure 5.22 Dependency of comparison between the experimental and theoretical angular distributions on incident energy for fired fractions of the incident energy. Target and fractions are indicated. Comparison applies to the $(p, {}^3\text{He})$ reactions.

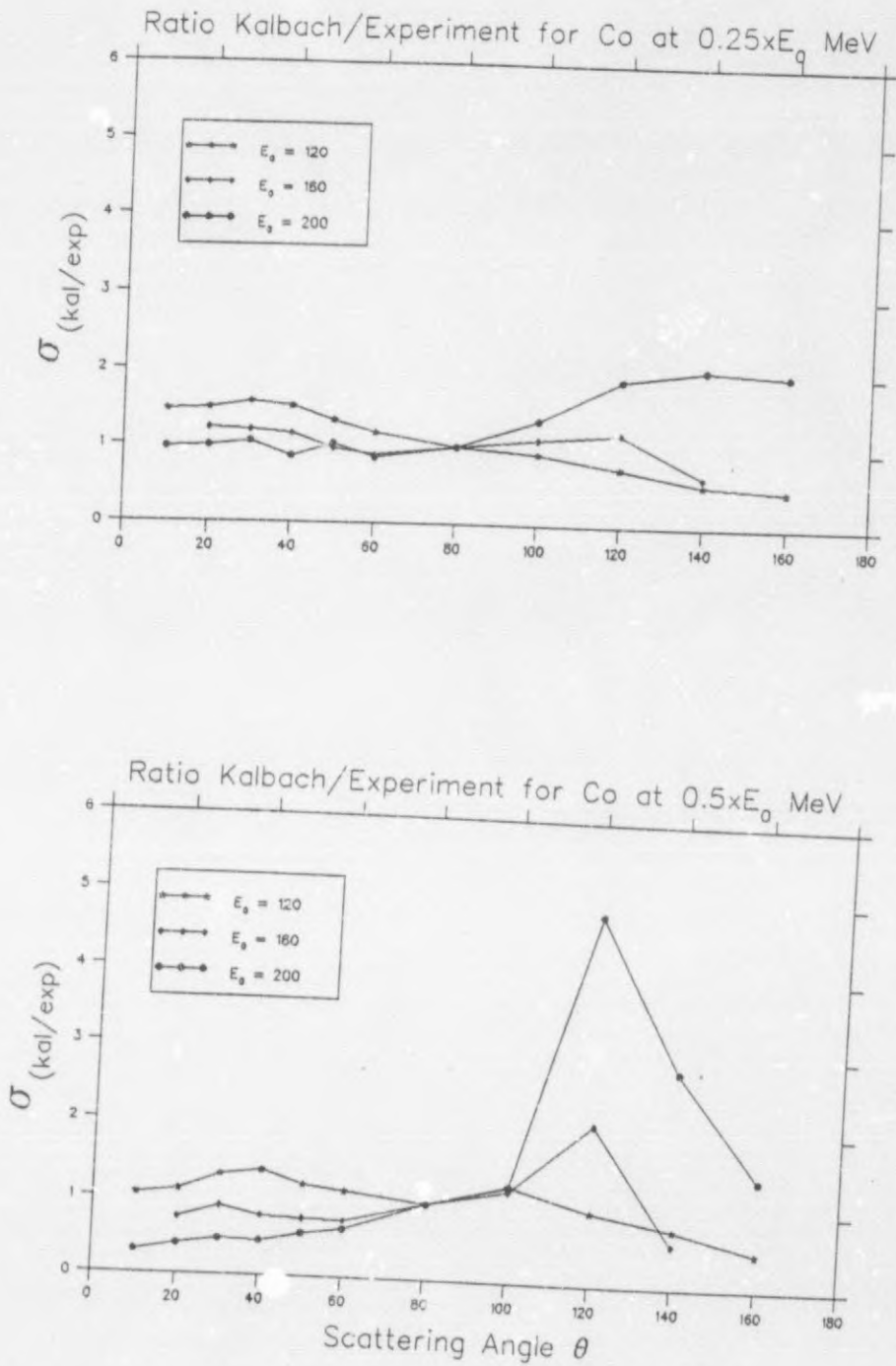


Figure 5.22 *Continues*

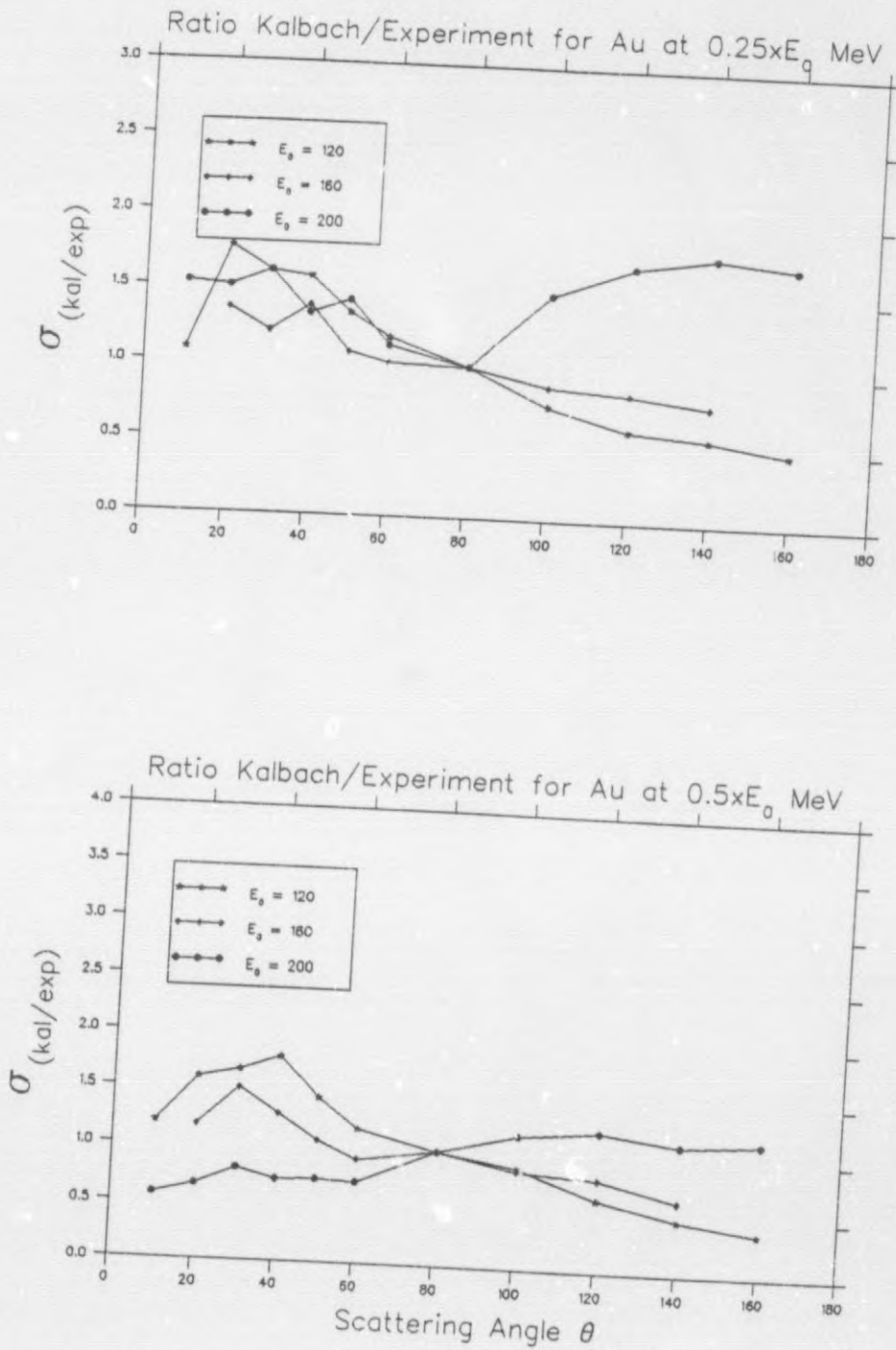


Figure 5.22 Continues

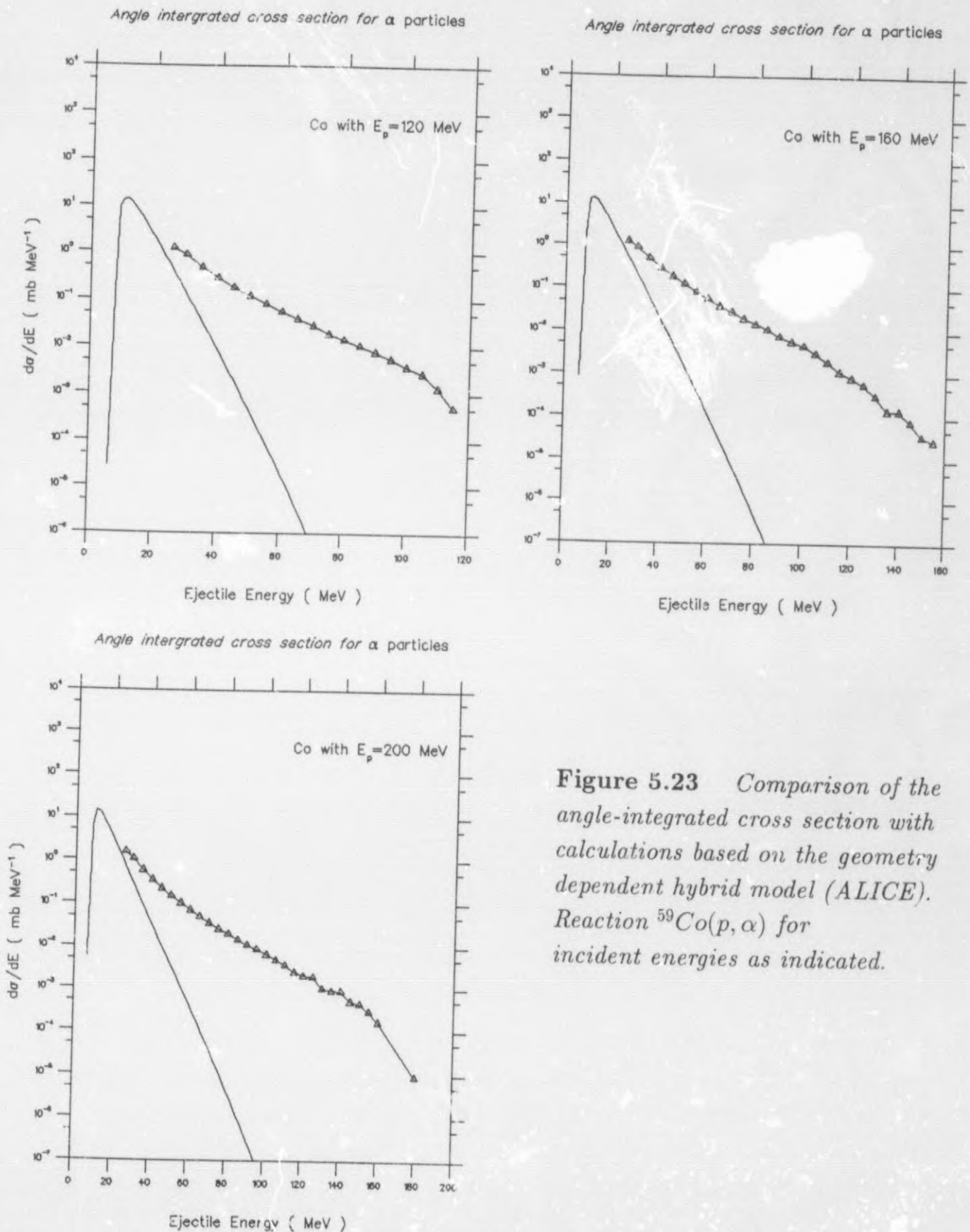


Figure 5.23 Comparison of the angle-integrated cross section with calculations based on the geometry dependent hybrid model (ALICE). Reaction $^{59}\text{Co}(p, \alpha)$ for incident energies as indicated.

CHAPTER SIX

SUMMARY AND CONCLUSIONS

SUMMARY AND CONCLUSIONS

In this work the systematic behaviour of the continuum of complex ejectiles was investigated as a function of incident proton energy and target mass. Data were acquired for the reactions $^{27}\text{Al}(p, X)$, $^{59}\text{Co}(p, X)$, and $^{197}\text{Au}(p, X)$, with $X=\alpha$ and ^3He , at incident proton energies of 120, 160, and 200 MeV.

The experimental angular distributions for the (p, α) and $(p, ^3\text{He})$ reactions were compared with the multistep direct (MSD) part of the phenomenological parametrization of Kalbach. In general good agreement was obtained for both reactions, which confirms the predicative power of the parametrization with regard to the angular distributions of the reactions. Nevertheless, systematic discrepancies depending on target mass and incident proton energy were observed. As the incident energy increased the agreement between the experimental angular distribution and the parametrization deteriorated. The trend was quite different from the discrepancy encountered for (p, p') by Cowley et al [11] which could be corrected with a slight modification of the parametrization. Furthermore it was found that the agreement between the experimental angular distributions and the parametrization improved as the target mass increased.

One of the reasons for trusting that a study of the phenomenology would be useful, was because Chadwick et al [26] were able to derive theoretically the expression contained in the parametrization of Kalbach. This derivation was based on the conservation of linear momentum and implies that the parametrization, although empirical, has a firm physical foundation.

Apart from a hybrid model calculation to estimate evaporation of α particles, no other semi-classical models were explored in this work. Semi-classical models which address pre-equilibrium emission of complex ejectiles are:

- The cluster model of Iwamoto et al [35] in which the exciton model takes explicit account of preformation probabilities for clusters [36, 37] and
- The pick-up model of Bisplinghoff [38] in which the pick-up mechanism [31, 39] is included into the exciton model without the consideration of preformation probabilities.

Because the former model relies on the introduction of an arbitrary preformation probability, and the latter model only became available after completion of this work, no calculations were performed with the models.

Quantum mechanical treatments are not currently available to model the likely mechanisms involved in (p, α) and $(p, ^3\text{He})$ reactions properly, therefore it was not possible to extract further information from the experimental data at this stage.

The systematics of the agreement, or lack thereof, between the experimental angular distributions and the parametrization of Kalbach could provide guidance to the future attempts to develop a proper quantum mechanical description of the reaction mechanism of complex-ejectile production induced by energetic protons.

REFERENCES

1. Note on the transmutation function for neutrons
J. Oppenheimer and M. Philips
Physical Review 48 (1935) 500
2. Nuclear Reactions and Nuclear Structure
P. Hodgson
Oxford University Press Oxford 1971
3. Neutron capture and nuclear constitution
N. Bohr
Nature 137 (1936) 344
4. N. Bohr and Kalckar
Danske Vidensk. Selsk. Mat. Fys. Meddr 14 10
5. Nuclear reactions at high energies
R. Serber
Physical Review 72 (1947) 1114
6. Energy dependence of average direct reaction cross sections and partial nuclear level densities
J. Griffin
Physics Letters 24B (1967) 5
7. Pre-equilibrium emission
E. Gadioli and E. Gadioli-Erba
Nuclear Instruments and Methods 146 (1977) 265
8. Pre-equilibrium nuclear reactions
E. Gadioli and P. Hodgson
Clarendon Press Oxford 1992
9. The statistical theory of multistep compound and direct reactions
H. Feshbach, A. Kerman and S. Koonin
Annals of Physics 125 (1980) 429
10. Pre-equilibrium Decay
M. Blann
Annual Review of Nuclear Science 25 (1975) 123
11. Continuum protons from the inclusive reaction $^{197}\text{Au}(p, p')$ at incident energies between 100 and 200 MeV
A. Cowley, S. Förtsch, J. Lawrie, D. Whittall, F. Smit and J. Pilcher
Zeitschrift für Physik A336 (1990) 189

12. Continuum protons from $^{58}\text{Ni}(p,p')$ at incident energies between 100 and 200 MeV
S. Förtsch, A. Cowley, J. Lawrie, D. Whittal, J. Pilcher and F. Smit
Physical Review C43 (1991) 691
13. Statistical multistep direct calculations for (p,p') continuum spectra up to 200 MeV
W. Richter, A. Cowley, R. Lindsay, J. Lawrie, S. Förtsch, J. Pilcher, R. Bonetti and P. Hodgson
Physical Review C46 (1992) 1030
14. Pre-equilibrium (p,p') measurements and calculations for ^{90}Zr and neighbouring nuclei for incident energies up to 200 MeV
W. Richter, A. Cowley, G. Hillhouse, J. Stander, J. Koen, S. Steyn, R. Lindsay, R. Julies, J. Lawrie, J. Pilcher and P. Hodgson
Physical Review C49 (1994) 1001
15. Commissioning of the NAC separated-sector cyclotron
A. Botha, H. Jungwirth, J. Kritzinger, D. Reitmann and S. Schneider
Proceedings of the Eleventh International Conference on Cyclotrons and their Applications (1986) 9
16. Radiation Detection and Measurement (2nd edition)
G. Knoll
John Wiley & Sons (1979) Singapore
17. Proton emission in pre-equilibrium reactions induced by incident protons of 100 to 200 MeV
S. Förtsch
Ph. D thesis University of Pretoria (unpublished)
18. The Feshbach-Kerman-Koonin multistep compound reaction theory
R. Bonetti, M. Chadwick, P. Hodgson, B. Carlson and M. Hussein
Physics Reports 202 (1991) 171
19. Multistep direct reaction analysis of continuum spectra in reactions induced by light ions
T. Tamura, T. Udagawa and H. Lenske
Physical Review C26 (1982) 379
20. Statistical theory of pre-compound reactions
H. Nishioka, H. Weidenmüller and S. Yashida
Annals of Physics 183 (1988) 166
21. Randomness in multistep direct reactions
A. Koning and J. Akkermans
Annals of Physics 208 (1991) 216

22. Hybrid model for pre-equilibrium decay in nuclear reactions
M. Blann
Physical Review Letters 27 (1971) 337
23. Importance of the nuclear density distribution on pre-equilibrium decay
M. Blann
Physical Review Letters 28 (1972) 757
24. Global test of modified pre-compound decay models
M. Blann and H. Vonach
Physical review C28 (1983) 1475
25. Systematics of continuum angular distributions: Extensions to higher energies
C. Kalbach
Physical Review C37 (1988) 2350
26. Physical basis for the Kalbach angular distribution systematics
M. Chadwick and P. Obližinský
Unpublished
27. Particle-hole state densities with linear momentum and angular distributions in pre-equilibrium reactions
M. Chadwick and P. Obližinský
Physical Review C46 (1992) 2028
28. Phenomenology of continuum angular distributions. Systematics and parametrization
C. Kalbach and F. Mann
Physical Review C23 (1981) 112
29. Possible energy parameters for continuum angular distributions
C. Kalbach
Physical Review C25 (1982) 3197
30. Charged-particle spectra: 90 MeV protons on ^{27}Al , ^{58}Ni , ^{90}Zr , and ^{209}Bi
J. Wu, C. Chang and H. Holmgren
Physical Review C19 (1979) 698
31. The pick-up mechanism in composite particle emission
Z. Jingshang, Y. Shiwei and W. Cuilan
Zeitschrift für Physik A344 (1993) 251
32. Study of the thermalization process in 72 MeV ($p, ^3\text{He}$) and (p, α) inclusive reactions
M. Kozłowski, H. Müller, R. Wagner and K. Czerski
Nuclear Physics A462 (1986) 554

33. Accretion model for the hot source formation in 72 MeV proton induced ^3He and α emission
M. Kozłowski, H. Müller and R. Wagner
Nuclear Physics A487 (1988) 133
34. M. Blann and J. Bisplinghoff
Lawrence Livermore National Laboratory Report No. UCID 19614 (1983)
Unpublished
35. Mechanism of cluster emission in nucleon-induced pre-equilibrium reactions
A. Iwamoto and K. Harada
Physical Review C26 (1982) 1821
36. Preformation probability of α clusters in rare earth nuclei measured by means of the (p, α) reaction
L. Milazzo-Colli, G. Bragg-Marcazzan, M. Milazzo and C. Signorini
Nuclear Physics A218 (1974) 274
37. Pre-equilibrium α emission induced by different incident channels: Evidence for α preformation in nuclei
A. Chevarier, N. Chevarier, A. Demeyer, G. Hollinger, P. Pertosa and Tran Minh Duc
Physical Review C11 (1975) 886
38. Pre-equilibrium α emission in the exciton model
J. Bisplinghoff
Physical Review C50 (1994) 1611
39. A method for calculating double differential cross sections of α particle emission
Jingshang Zhang
Nuclear Science and Engineering 116 (1994) 35